1-16-2020

Vibrational and Electronic Structure of Environmentally Persistent Free Radicals Formed on Metal Oxide Nanoclusters and Single-Crystal Surfaces

Nadra Ibrahim Sakr
Louisiana State University and Agricultural and Mechanical College

VIBRATIONAL AND ELECTRONIC STRUCTURE OF ENVIRONMENTALLY PERSISTENT FREE RADICALS FORMED ON METAL OXIDE NANOCLUSTERS AND SINGLE-CRYSTAL SURFACES

A Dissertation

Submitted to the Graduate Faculty of the
Louisiana State University and
Agricultural and Mechanical College
in partial fulfillment of the
requirements for the degree of
Doctor of Philosophy

in

The Department of Physics and Astronomy

by
Nadra Ibrahim Sakr
B.S., Ain Shams University, 2002
M.S., Ain Shams University, 2006
May 2020

To my beloved family

Acknowledgements

First and foremost, I would like to thank my advisor, Dr. Phillip Sprunger, for granting me the chance to join his research group and gain valuable experimental research skills and knowledge of an interesting research topic. His scientific acumen and depth of knowledge have always inspired me. I truly acknowledge his continuous support and patience throughout my journey to PhD.

I extend my deepest gratitude to Dr. Erwin Poliakoff and Dr. Richard Kurtz for their invaluable discussions and guidance. I also would like to thank Dr. Juana Moreno and Dr. Stephen Shipman for their advice and comments. I am deeply indebted to Dr. Matthew Patterson and Dr. Orhan Kizillikaya for their continuous support, inputs, and encouragement as well as their enthusiasm for the research which have helped me materialize this dissertation.

I would sincerely like to thank Dr. Slawo Lomnicki, Dr. Farhana Hassan, and Dr. Rafael Cuato for giving me access and assistance to the EPR facility. I also would like to thank Dr. Tammy Dugas in the Superfund Research Center for bringing all the PhD students to discuss multidisciplinary topics. This has definitely expanded my knowledge of the subject and broadened my scientific horizons. I would like to express my sincere gratitude and appreciation to Dr. Dana Browne for his support throughout my PhD. I am also thankful to my fellow graduate student Frank McKay for his great help in the lab which has eased my experimental frustrations.

Finally, my dearest gratitude to my great parents and my wonderful family, specially my husband and my kids Yaseen and Mariam who came at different stages of my journey to PhD. You have brought a lot of joy into my life that has comforted the stress of the world outside.

Table of Contents

Abstract

We have studied the morphology and electronic structure of transition metal oxides (TMOs) nanoparticles and single-crystal surfaces which are known to be active for the formation of environmentally persistent free radicals (EPFRs) from organic precursors. We have also investigated the effect of simulated solar irradiation on the formed EPFRs.

First, we examined the change in the vibrational and structural properties of TiO_2, ZnO, CuO, and Fe_2O_3 nanoparticles due to phenol adsorption at high temperature and thus EPFR formation on the surface of these TMOs. The paramagnetic signal observed by electron paramagnetic resonance (EPR) indicates the formation of phenoxyl-type radical. Vibrational spectroscopy has further confirmed the formation of EPFRs by the disappearance of –OH groups which indicates the chemisorption of the organic precursor on the metal oxide surface, as well as observing both ring torsion mode and C-H in-plane bend characteristic of phenol adsorption on the studied systems. In this study, we have also investigated the change of the oxidation of the metal cations upon phenol adsorption at elevated temperature. We have found that the direction of charge transfer (redox) during phenol chemisorption is strongly dependent on surface properties as well as surface defects of the metal oxide surface.

Second, we studied the adsorption behavior of phenol on the surface of α–Fe_2O_3 (0001) single-crystal surface at both high temperature and ambient to probe the changes in the electronic structure due to adsorption. At room temperature dosing, phenolic bands have been clearly observed in the UPS spectrum indicating the physisorption of phenol on the metal oxide surface. Upon dosing at high temperature, both techniques have shown clear features that strongly suggest a charge transfer from the organic precursor to the metal oxide. This evidence agrees well with the

EPFRs proposed formation mechanism, and can guide future experimental and computational studies.

The spin density of EPFRs formed by phenol adsorbed on TiO_2 nanoparticles at high temperature is found to increase upon exposure to simulated solar radiation as well as a mild shift in the g-value. Furthermore, solar irradiation induces the transformation of phenoxyl radical to a combination of catechol and some quinone product.

Chapter 1. Introduction

1.1. Environmentally Persistent Free Radicals (EPFRs)

EPFRs are long-lived surface bound radicals that are known to form on particulate matter (PM) [1]. EPFRs are formed by the adsorption of organic precursors on the surface of metal oxides which are bound to PM. EPFRs are found in contaminated superfund soils [2, 3], soot [4-7], clays [8], and cigarette smoke [9-11]. Figure (1.1) shows the basic formation mechanism of EPFRs. Organic precursors (such as chlorinated phenols or benzenes, hydroquinone, and catechol) initially physisorb to the surface of the transition metal oxide (TMO) via Van der Waals interaction between the metal OH and the organic Cl or OH, followed by elimination of water or HCl (depending on the type of the organic precursor). Thus, the organic precursor chemisorbs to the TMO surface. EPFRs are formed when a charge transfer occurs between the metal center and the organic precursor, resulting in a change of the oxidation state of the metal cations.

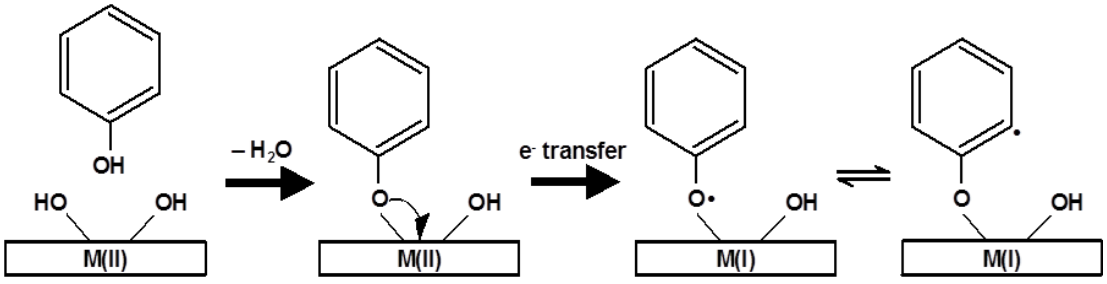

Figure 1.1. Schematic of EPFRs formation from phenol as an organic precursor on the surface of metal oxide [adapted from Patterson, 2017 [12]].

EPFRs are known to have half-lives longer than typical free radicals; they can last for hours, week, and even month. *Ab initio* calculations have shown that EPFRs gain their stability from resonance with phenyl ring [13], which enables them to resist decomposition and persist in ambient environment [14]. Dellinger et al. have shown that the lifetime of the formed EPFRs depends on both the type of TMO as well as the type of the aromatic adsorbate [15]. For example, figure (1.2)

displays the decay profile of EPFRs formed on the surface of ZnO/SiO_2 dosed with different organic precursors at 230 ºC. For the same TMO, adsorbates as phenol (PH), monochlorobenzene (MCBz), and 2-monochlorophenol (2-MCP) have two decay profile (short and long lifetimes),

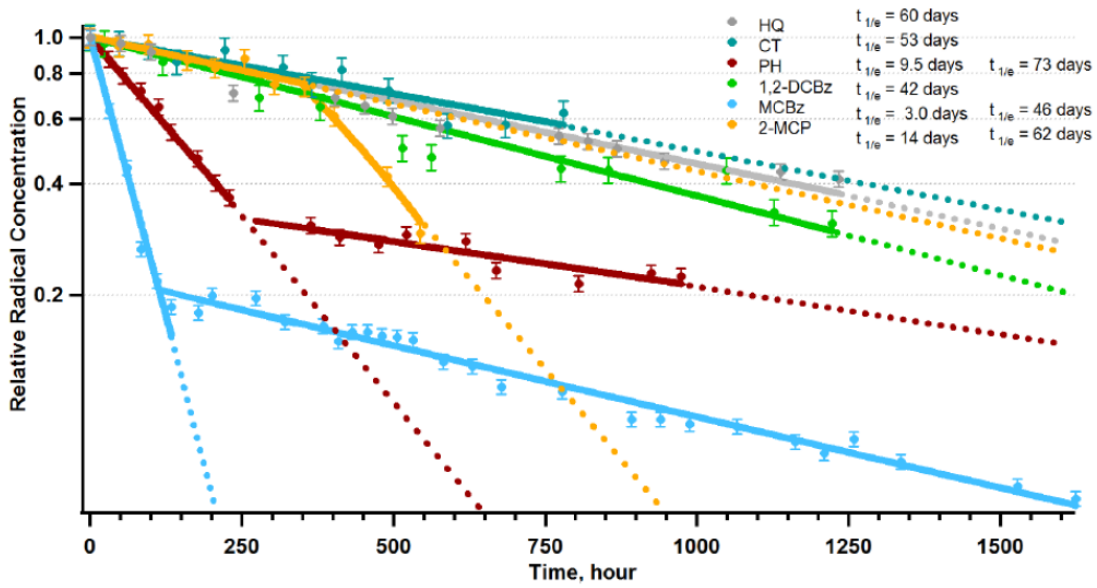

Figure 1.2. First order decay profile of EPFRs on ZnO/SiO_2. [reprinted with permission from reference[15], Copyright 2012 Royal Society of Chemistry].

while hydroquinone (HT), catechol (CT), and 1, 2-dichlorobenzene (1, 2-DCBz) have only long lifetimes [15]. Dellinger et al. have found that the long-lived species on the surface of ZnO/SiO_2 are semiquinone-type radical which result from the reaction of the phenoxyl species with the surface whereas the shorter-lived ones are phenoxyl (or chlorophenoxyl) radicals which result from the surface decomposition of dihyroxybenzenes [15]. Thus, EPFRs formed by phenol dosed ZnO/SiO_2 has longest-lifetime compared to EPFRs formed by 1, 2-DCBz dosed ZnO/SiO_2 as shown in figure (1.3). Also, the type of TMO plays a role in determining the 1/e lifetime of the EPFRs formed. Decay studies have been performed on the EPFRs formed by phenol dosed metal oxide powders. The 1/e lifetimes reported for the pure oxide powder of TiO_2 [16] are 4.2 days for short decay and 57.4 days for long decay. As for the ZnO, CuO, and Fe_2O_3, the decay studies were performed on

the 5 wt% metal oxide supported on SiO_2. The 1/e liftetimes of ZnO [15] are 10 days for short decay and 70 days for long decay, while for CuO [17] and Fe_2O_3 [18] , the 1/e lifetimes are 74 minutes and 3.8 days respectively.

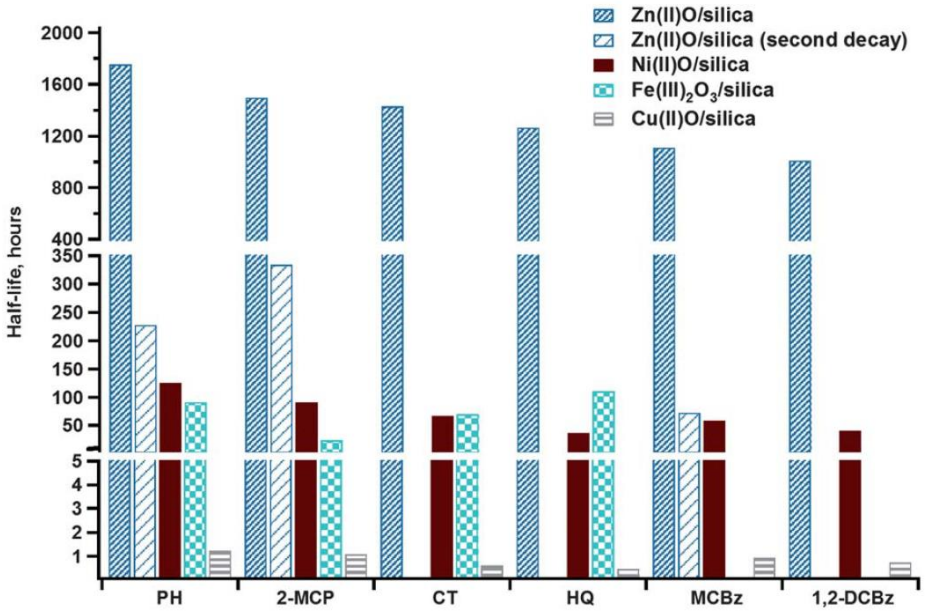

Figure 1.3. Comparison of half-lives of EPFRs for different organic precursors formed on various metal oxides [reprinted with permission from reference [15], Copyright 2012 Royal Society of Chemistry].

Dellinger's group have conducted several studies on TMOs supported on silica dosed by various organic precursors at a range of high temperatures, and they have found that EPFRs are thermally activated, and that the EPFRs formed rely on the structure of the organic precursor as well as the dosing temperature [17-19]. For instance, figure (1.4) shows electron paramagnetic spectroscopy (EPR) spectra of 5% CuO/SiO_2 and dosed with PH, 2-MCP, CT, HQ, MCBz, and 1, 2-DCBz. Two types of EPFRs have been observed, namely g2 and g3 which refer to the g-value of phenoxyl and semiquinone radicals, respectively. PH dosed CuO/SiO_2 has produced g2 radical at all temperatures with the highest radical yield observed at 230 ºC. Conversely, HQ has formed g3 radicals at all temperatures. For 2-MCP, g2 has formed at low temperatures whereas both g2

and g3 have been observed at high temperature. They have regarded this observation to the activation energy required for the elimination of OH and Cl during chemisorption, as OH requires less energy to overcome the activation barrier for its elimination compared to Cl. Therefore, at high temperature (~200 °C) both processes become feasible.

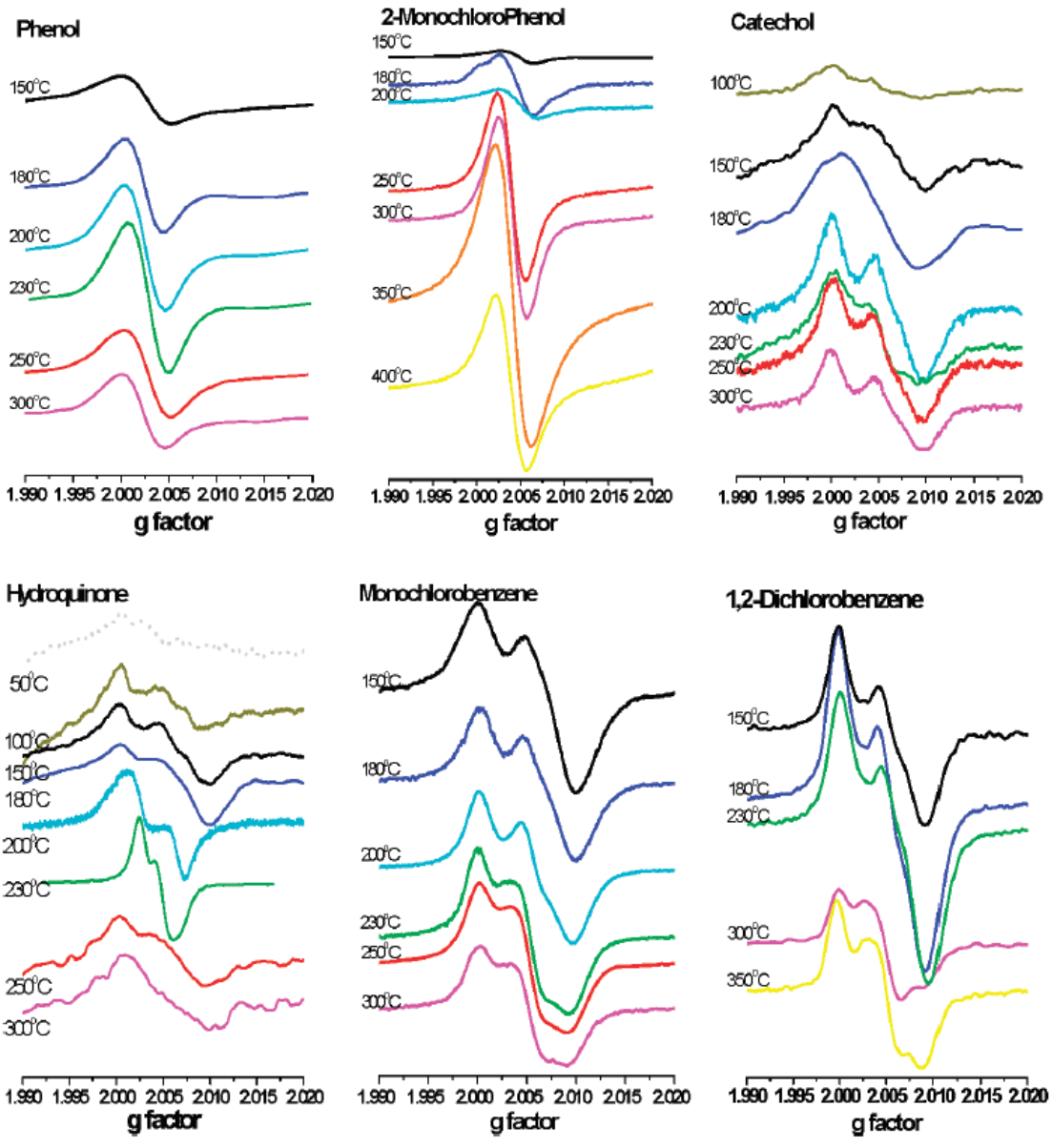

Figure 1.4. EPR spectra of 5% CuO/SiO_2 dosed with different radical precursors at different temperatures [reprinted with permission from reference [17], copyright 2008 American Chemical Society].

1.2. Sources of EPFRs

The formation of EPFRs depends on the presence and abundance of catalytically active TMO and organic compounds [13, 17]. Hydroxylated aromatic precursors such as PH, HQ, and CT are found in biomass [20-22], industrial processes [23], and are the most abundant organic components in cigarettes [24-26]. On the other hand, chlorinated aromatic precursors such as 1, 2-DCBz, MCB, and 2-MCP are found in municipal and hazardous wastes [20, 27]. Characterization of EPFRs generated by combustion systems and thermal processes has revealed that iron and copper are the most abundant catalytic transition metal along with other metals as nickel and zinc [28-31]. These transition metals are known to enhance the formation of polychlorinated dibenzodioxin and dibenzofurans (PCDD/Fs), in particular, iron and copper [32-37].

EPFRs form through a series of surface-mediated reactions [13, 17]. Their formation takes place in the cool zone of combustion processes which have been shown to be the main source of PM [38]. Sources of combustion systems range from engine exhaust, waste incinerators, biomass burning, and refineries [28, 38-45]. Figure (1.5) shows the zone diagram of combustion process. The combustion process is divided into five zones based on the temperature range of that particular zone. In zone 1, the fuel is vaporized and mixed, therefore this zone is called preflame zone. The fuel is then exposed to high temperature flame (1000-1800 ºC), and thus metals and chlorine vaporizes and organic material combusts into CO_2, H_2O and HCl in zone 2 (flame zone). Zone 3, noted as post-flame thermal zone, is characterized by lower temperatures (600-1200 C). In this zone, dissociated molecules proceed by gas phase reactions where they condense into nanoparticles, at the low limit of the zone's temperature, or recombine into molecular compounds. Finally, zones 4 & 5 (cool zone), is characterized by temperatures less than 600 ºC. Therefore, the

gases are cooled and surface-mediated reactions with TMOs take place producing EPFRs along with other harmful pollutants as dioxins [46] and furans [47].

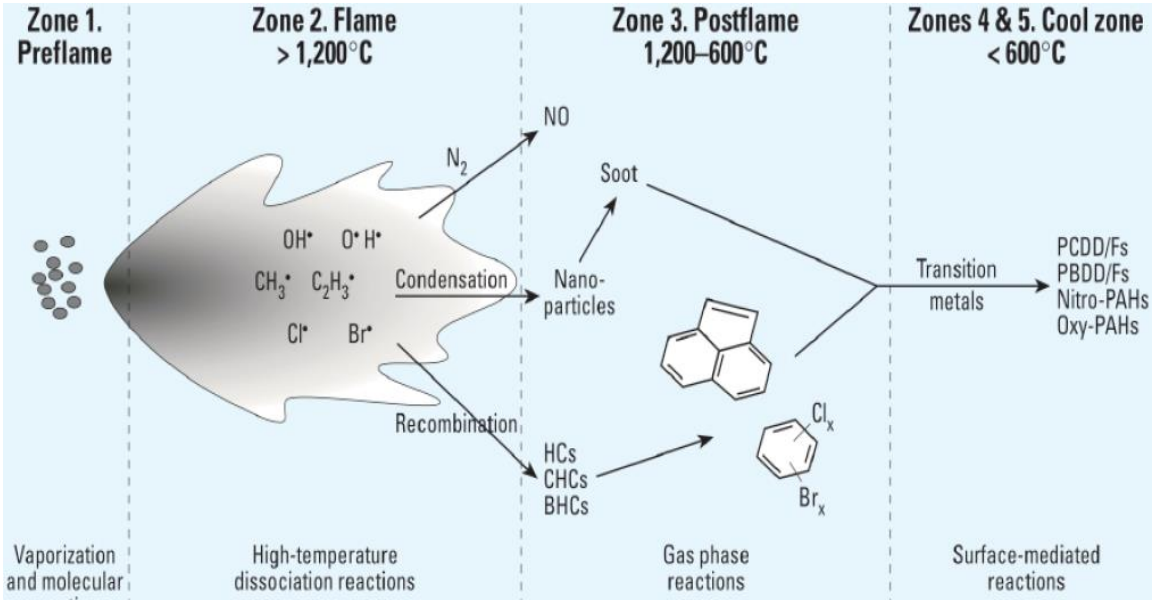

Figure 1.5. Zone theory of combustion systems [reprinted with permission from Environmental Health Perspectives from reference [48], copyright 2006].

1.3. Health Implications of EPFRs

Airborne and combustion-generated particles are found to contain a significant amount of EPFRs [13, 17, 49, 50]. Recent studies have found a correlation between PM, mortality, and morbidity [51-55]. It has also been found that EPFRs may play a significant role in the toxicity of PM [3, 56, 57]. PM is a complex mixture of liquid droplets and microscopic solid particles suspended in gas phase [58], and are classified based on their aerodynamic size to three modes: coarse (10 - 2.5 μm), accumulation (< 2.5 μm -100 nm), and nucleation mode (ultrafine particles) (<100 nm) [58]. PM poses adverse health effects, in particular, particles in nucleation mode because their higher surface area and number concentration make it feasible for toxic pollutants to condense on their surface [59]. On the other hand, upon inhalation of ultrafine particles, their size allows them to travel deep

into the respiratory tract where they can deposit in the lower respiratory system causing several cardiovascular and respiratory diseases [60, 61].

The damage induced by PM depends on the ability of the organic compounds adsorbed on its surface to redox cycling [62]. The toxicological effects of EPFR-containing PM arises from its ability to generate sustained reactive oxygen species (ROS) [63-66]. ROS produced from secondary reactions with EPFRs include hydrogen peroxide, superoxide anion, and hydroxyl radical which is the most biologically damaging of all [67-70]. ROS are necessary in the maintenance of cellular components, however, overproduction of ROS causes oxidative stress and cell damage [62]. Several studies reported that exposure to high concentration of EPFR-containing PM causes DNA damage [49], asthma [71], increased flu [72], decreased cardiac function [73, 74], and pulmonary toxicity [75].

ROS production can be catalyzed by the presence of metals in PM [64]. Iron (III) and copper (II) contribute by up to 2.35% and 0.05%, respectively, in combustion-generated PM [76]. PM samples have been collected from six cities across the united states and were analyzed. Studies conducted on these samples revealed that sufficient amount of radical species attributed to semiquinone are found in PM with particle size of 2.5 μm ($PM_{2.5}$) [13, 17, 50, 77-84]. It has been proposed that ROS are generated from EPFRs by semiquinone radical that initially reduces oxygen and producing superoxide anion [23, 81, 85-88]. Superoxide anion undergoes dismutation with biological reducing agents and hydrogen peroxide is produced [89]. The role of transition metals in ROS generation is to catalyze hydroxyl radical formation via Fenton reaction from the hydrogen peroxide produced. The resulted hydroxyl radical is reported to cause biological damage to DNA [23, 87, 89, 90].

1.4. Research Objectives

The objectives of this study are threefold. The first objective is to study the characteristics of the EPFR signature produced by phenol, as an organic precursor, to the surface of four different TMOs nanoparticles that are known to be active in catalyzing EPFRs formation. Second, is to examine the adsorption behavior of phenol on α-Fe_2O_3 (0001) single crystal using surface science techniques to gain deeper understanding of the atomistic and electronic structure of the EPFRs generated by phenol. Finally, the third objective is to expose the EPFRs, generated by dosing TiO_2 with phenol at high temperature, to simulated solar radiation and observe changes in EPFR signal.

The main goal of the first objective is to study the ability of different transition metal oxide to catalyze EPFR formation from phenol. We also need to find a pattern in the results obtained for each TMO that will help future researchers to easily identify EPFRs produced from phenol. We have chosen Cu(II)O and $Fe(III)_2O_3$ nanoparticles, since research has found that these two TMOs exist in combustion-generated PM with high concentration [76]. Also, Zn(II)O and $Ti(IV)O_2$ are included in this study due to their high activity in forming EPFRs [16].

This study has employed electron paramagnetic resonance (EPR) to study the concentration and type of the radical formed. The formation and decay of EPFRs are investigated by Fourier transform infrared spectroscopy (FTIR) which enables one to study the changes in the surface functional groups due to chemisorption of phenol as well as the decay of the EPFR formed. The changes in the vibrational structure due to phenol chemisorption were further investigated by inelastic neutron scattering (INS), which shows modes that are IR inactive. The proposed mechanism of EPFRs formation requires a charge transfer between the surface of the metal oxide and the organic precursor for the radical to be formed, as shown in figure (1.1). We have studied the change in the oxidation state of the metal centers in the four selected TMOs and we have found

a relation between surface property of the metal oxide prior to dosing and direction of the charge transfer. This study was performed by utilizing X-ray photoelectron spectroscopy (XPS).

In the second objective, we study the adsorption behavior of phenol on α-Fe_2O_3 (0001) single crystal at room temperature and at 250 ºC where EPFRs are known to form. Hematite, α-Fe_2O_3, is the most thermodynamically stable iron oxide phase at room temperature [91]. It crystallizes in the corundum structure and contains Fe^{3+} cations in octahedral sites [92]. We are interested in Hematite because the iron found in PM exist as Fe^{3+} rather than Fe^{2+} [93]. By comparing the two adsorption behaviors, one can determine the structural changes which are attributed to EPFR formation.

This study has been conducted in ultrahigh vacuum (UHV) systems with a base pressure of 10^{-10} Torr to ensure surface cleanliness and that only phenol molecules adsorb on the surface. Furthermore, the surface of the single crystal was checked, prior to dosing, by low energy electron diffraction (LEED). The objectives of this study have been accomplished by utilizing ultraviolet photoelectron spectroscopy (UPS) and XPS, which enable one to study the occupied electronic states in both valence band and in the core, respectively. The direction of charge transfer has also been verified and was found to be consistent with the proposed mechanism.

Finally, the third objective was realized by exposing phenol dosed anatase TiO_2 nanoparticles to simulated solar radiation for different durations. The change in spin density as a function of exposure time along with change in the g-value have been measured and compared with the non-irradiated sample. The change in surface functional groups as a function of exposure time has also been studied using FTIR.

Chapter 2. Experimental Methods and Techniques

2.1. Introduction

The investigation of EPFRs formation on single crystal surfaces demands preparing and characterizing the surface using ultra high vacuum (UHV) techniques to ensure that we are dealing with a clean and well-defined surface prior to dosing with ultra-pure gas. This chapter describes the general techniques used to prepare the single crystal, the method for probing surface morphology (LEED), and spectroscopic techniques utilized to investigate the electronic structure of the surface pre and post dosing (XPS and UPS). This chapter also describes the FTIR technique used to study the vibrational structure of the EPFRs formed on TMO nanoparticles as well as their detection (EPR). The main emphasis of this chapter is to present the physics behind these techniques and the information that can be obtained upon utilizing them.

2.2. Principles of Ultra High Vacuum

Surface science techniques demand UHV to be performed. The importance of UHV arises mainly from two requirements: first, the trajectories of ions and/or electrons involved in a surface science analysis have to remain uninterrupted by other particles in the surrounding environment. Second, the investigated surface has to remain clean of contaminants while the experiment is being conducted. Thus, long mean free path as well as long monolayer time are required to achieve surface science analysis, and are therefore, the terms required to understand the concept of vacuum [94].

Starting with mean free path which is defined as the average distance travelled by a gas molecule between two successive collisions. The kinetic theory of gases, which explains the macroscopic properties of gases, enables us to derive an expression for the mean free path. For gas molecules in a container will collide with the walls of the container, and will also collide elastically

with each other. The collision rate, z, which is defined as the average number of collisions per second between gas molecules, is given by

$$z = \frac{\langle c \rangle}{\lambda} \tag{2.1}$$

where ⟨c⟩ is the mean particle speed, and λ is the mean free path. The mean particle speed is given by

$$\langle c \rangle = \sqrt{\frac{8kT}{pm}} \tag{2.2}$$

where k is the Boltzmann constant, m is the mass of the gas molecule, p is the pressure of the gas, and T is the absolute temperature. The pressure of the gas is also related to the mean square speed, $\langle c^2 \rangle$ and the number density, n through the equation:

$$p = \frac{1}{3} nm\langle c^2 \rangle \tag{2.3}$$

for collision to take place between two gas molecules which are modeled as two spheres each of a radius r, the separation distance between their centers has to be less than 2r. The collision rate is thus given by

$$z = \sqrt{2} n\pi (2r)^2 \langle c \rangle \tag{2.4}$$

Equation (2.4) into equation (2.1) yields:

$$\lambda = \frac{1}{\sqrt{2} n\pi (2r)^2} \tag{2.5}$$

From equation (2.5) we see that the mean free path is inversely proportional to the number density of molecules and hence the pressure. That is, if the pressure increases, the collision rate also increases resulting in a shorter mean free path and vice versa. Therefore, for a pressure of 10^{-9} Torr (UHV) and at room temperature, the mean free path of gas molecules is ~ 50 km. Thus,

gas molecules in UHV pressures collide with the walls of the chamber than colliding with other gas molecules.

Pressure also affects the time constant to form a monolayer. Time constant, τ, is given by

$$\tau = \frac{n_\circ}{I} \tag{2.6}$$

where $n_\circ$ is the number of atoms in a monolayer, and I is the flux of molecules impinging on the surface from the surrounding environment, and is given by the expression

$$I = \frac{p}{\sqrt{2\pi mkT}} \tag{2.7}$$

Similarly, equation (2.7) shows that the increase in pressure decreases the time to form a monolayer. That is, at a pressure of 10^{-9} Torr, it takes one hour to form one monolayer of adsorbates (for sticking coefficient of 1) on the surface from the gas phase. The typical time required to form surface science experiment should be around one hour. The main purpose of a UHV system is to obtain ultra-low pressure, or in other words, ultra-low number density of molecules in UHV chamber to enable taking data by surface science techniques with the lowest possibility of the surface becoming contaminated by gas phase molecules. However, gas molecules are inevitable even in UHV pressures, but again, their mean free path is much greater than the dimensions of the chamber. That is, gas molecules will collide with the chamber walls many times before it collides with another gas molecule. For the same reason, gas molecules (primarily H_2O) adsorb to the walls of the vacuum chamber and it takes time for these molecules to desorb and to be pumped out of the vacuum system. The problem here is, if any part of the chamber is heated, the pressure will rise and the surface of the sample will be contaminated. To maintain UHV pressure, bake out is mandatory. In the bake out process, the UHV chamber is heated to 150-250 ºC with heating tapes wrapped around the chamber. To ensure that the entire system is properly heated, heating blankets are wrapped around the chamber with the heating tapes attached. Also,

viewports, exposed connectors, and feedthrough are all wrapped with aluminum foil to avoid damage during to bake-out. The system can be baked 24-48 hours including the cool down period. After bake-out, residual gas analyzer (RGA) can be utilized to determine the cleanliness of the vacuum system by comparing the mass spectra of a vacuum chamber before and after bake-out, as shown in figure (2.1).

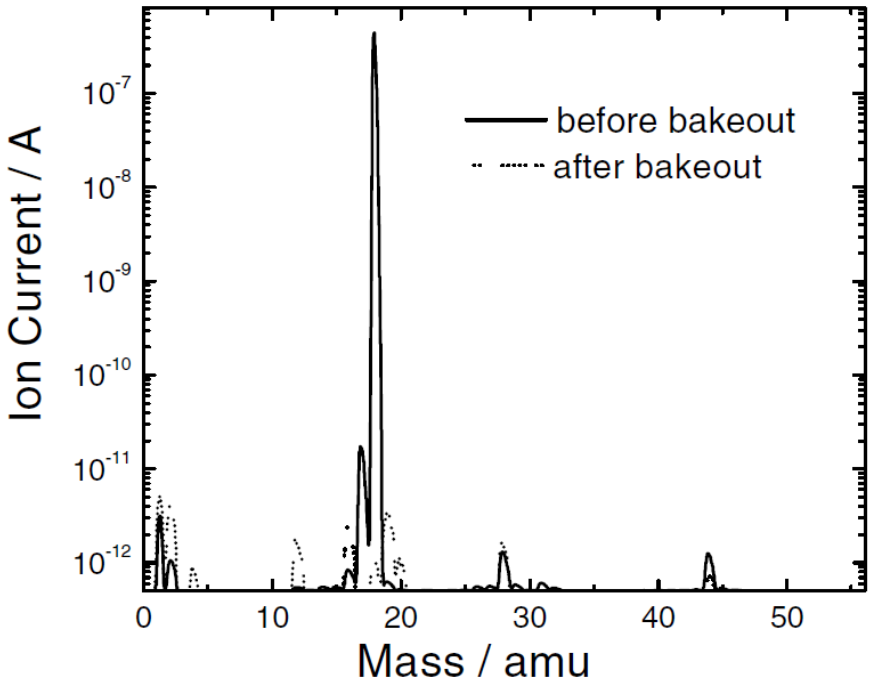

Figure 2.1. Mass spectrum of residual gas in a UHV chamber before and after bake-out [95].

To obtain and maintain the pressure of a UHV system, a system of vacuum pumps is utilized. The characteristics of a gas behavior changes with pressure [94]. Therefore, the vacuum pressure is divided into four regions based on the similar characteristics of the gas within that pressure region. The regions of the vacuum are [94]:

Rough vacuum	10^{3} -1	mbar
Medium vacuum	1-10^{-3}	mbar
High vacuum	10^{-3}-10^{-7}	mbar
Ultra-high vacuum	10^{-7}	mbar and below

It is the nature of the gas flow that makes the distinction between each vacuum region. In the rough vacuum region, viscous flow is the dominant behavior of the gas molecules, in which gas molecules collide with one another more frequently than with the walls of the conducting tube. On the other hand, in the high and ultra-high vacuum, the gas molecules move freely and no molecular interaction occurs, but gas molecules collide predominantly with the walls of the vessel. This type of flow is called molecular flow. The type of gas flow in the medium vacuum region represents a transition from viscous flow to molecular flow. This type of flow is called Knudsen flow.

Each type of the gas flow requires a pump that operates with a certain physical method. To bring a system from atmospheric pressure to 10^{-3} Torr (rough and medium vacuum), rotary pumps are employed. Rotary pumps are mechanical pumps that remove gas particles from the vacuum system to the atmosphere by compression in one or more stages [94]. These pumps can be oil lubricated or oil free, and they can also act as a backing pump. The most common type of these pumps are the vane rotary pump shown in figure (2.2).

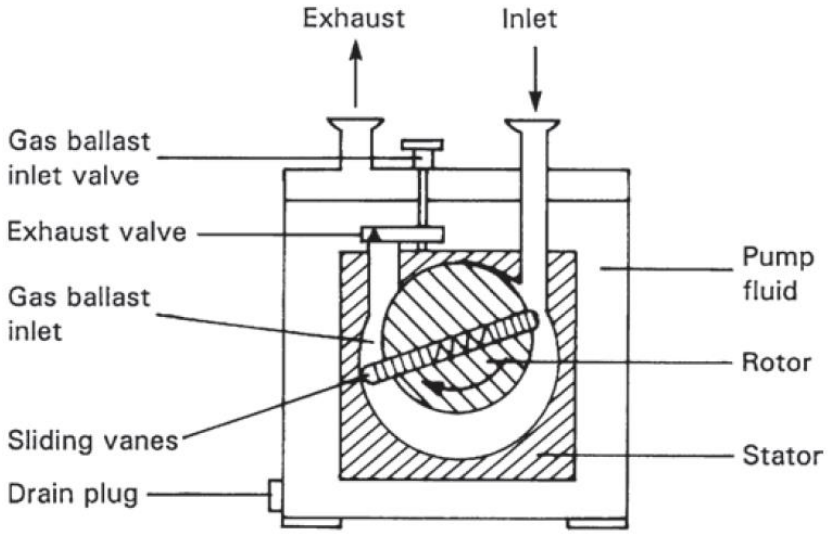

Figure 2.2. Cross section of a single-stage sliding vane rotary pump [94].

The pressure of the vacuum is further lowered to the high and ultra-high vacuum regions with another type of mechanical pumps called Turbomolecular pump. This pump is capable of pumping down the vacuum system to 10^{-9} Torr. Turbomolecular pumps remove gas particles by compression through high speed rotating blades which are angled downward. The blades will hit the gas molecules giving them an impulse to flow in the required direction [94]. The compressed gas is removed by a backing pump which is typically a rotary pump. Figure (2.3) shows cross-sectional picture of a Turbomolecular pump. Excess heat add up due to the friction resulting from the blades impacting the gas molecules at high speeds. Therefore, turbomolecular pumps need to be either air-cooled by a fan or water cooled.

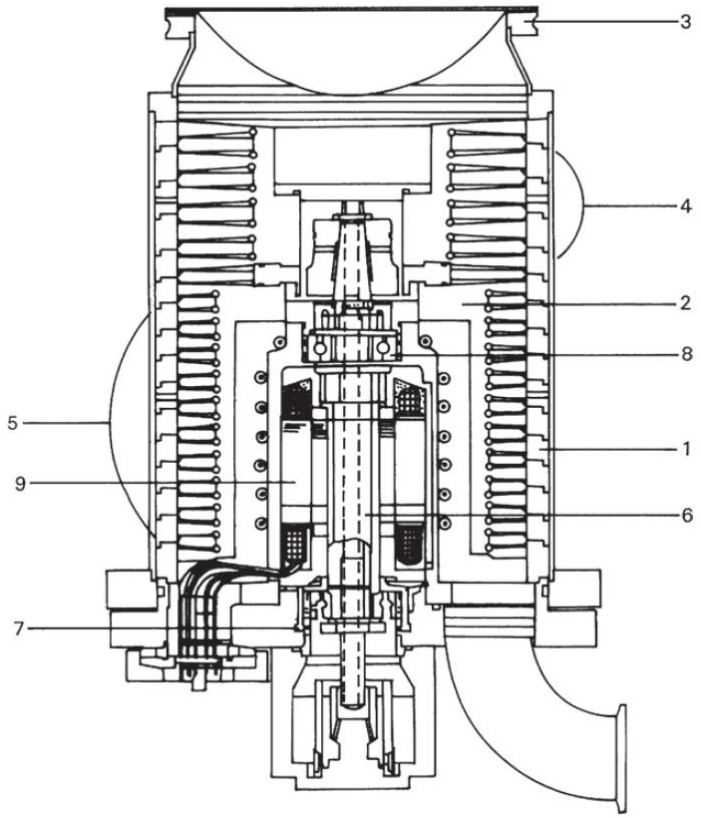

Figure 2.3. Cross-sectional picture of a Turbomolecular pump of a single-ended axial flow design: 1, stator blades; 2, rotor body; 3, intake flange; 4, blades of the suction stage; 5, blades of the compression stage; 6, drive shaft; 7 and 8, ball bearings; 9, high-frequency motor [94].

Finally, ion getter pumps are used to pump down vacuum systems to pressures below 10^{-7} Torr. Unlike rotary and turbomolecular pumps, these pumps are not mechanical pumps and they don't remove gases from vacuum system by compression. Ion getter pumps are a type of entrapment pumps where gas molecules are removed from vacuum system by adsorbing them to a solid wall. Figure (2.4) shows a diagram of a triode ion pump. The triode consists of a collector, an anode and a cathode made from titanium. The cathode is kept at a high negative electric potential (5-7 kV) causing electrons to be emitted from the cathode. The whole triode is maintained in a strong homogeneous magnetic field (0.1-0.2 T). Therefore, the magnetic force compels the emitted electrons to travel in an orbital path and ionize the gas molecules. The orbital path increases the probability of collisions with the gas molecules. The ionized molecules are then accelerated toward the cathode in an almost straight path relatively unaffected by the magnetic field due to their large mass. The ionized gas molecules impinge on the cathode and titanium is sputtered mostly in forward direction and deposits on the collector. Here titanium acts as a getter; its good mechanical properties and its high reactivity with residual gases allow it to absorb the residual gas molecules. Therefore, the gas molecules are not removed from the system to the atmosphere as in rotary and turbomolecular pumps, but they are trapped by titanium and become buried in the collector. The amount of titanium sputtered from the cathode and deposited on the collector is proportional to the number of the gas molecules which struck the cathode, and thus, to the pressure of the system.

The single-crystal used in this work was purchased from SurfaceNet GmbH (Germany). It is sold cut and polished along a certain atomic plane to their specification. The surface of the single-crystal has to be clean and prepared prior to performing any surface experiment. The cleaning procedure usually involves several cycles of ion sputtering and annealing.

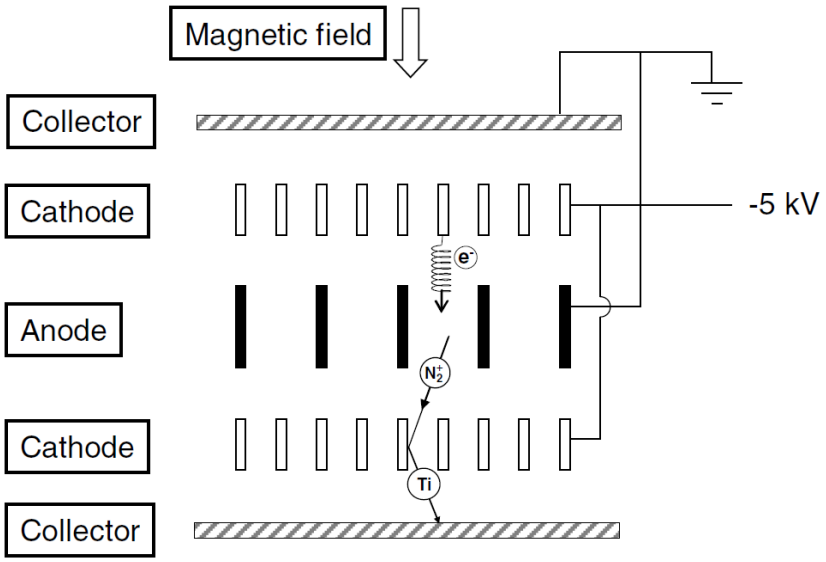

Figure 2.4. A diagram of a triode ion getter pump [95].

Sputtering involves ions of noble gas such as Ar^+ and Ne^+. The noble gas can be fed to the ion gun housing or to the entire chamber via a leak valve. Figure (2.5) shows an example of a sputter gun. The noble gas ions are generated by collisions with electrons which are emitted from the cathode and are accelerated toward the cage-anode. The purpose of the geometry of the cathode and the anode in figure (2.5) is to increase the collision probability. The positively charged gas ions are then accelerated to the required energy toward the cap and is focused onto the sample. Surface contaminants are removed when the gas ions strike the surface. This process can be achieved in three different mechanisms. The first mechanism is called direct knock-off process, as the name suggests, the contaminants are removed by the direct collision with the gas ion. The second is called the knock-off where the contaminant is removed by collision with the ion gas reflected off the surface. Finally, in the third process, gas ions strike the surface causing substrate atoms to be sputtered outward, the sputtered substrate particles transfer energy to the contaminants causing them to desorb from the sample's surface. The three processes take place at low ion energies, however, the first and second mechanisms decay with increasing ion energy while the

third becomes prevalent at about 1.5 keV [95]. Some contaminants, such as sulfur and carbon, are pushed deeper into the substrate matrix. Cleaning the surface thus requires several cycles of annealing and sputtering, since annealing the substrate bring these contaminants to the surface, hence sputtering becomes more effective. When the degree of surface cleanliness is obtained, high temperature annealing is recommended to restore the surface order. Annealing in UHV chambers is achieved by a tungsten filament attached behind the sample and can reach temperatures up to 1200 ºC.

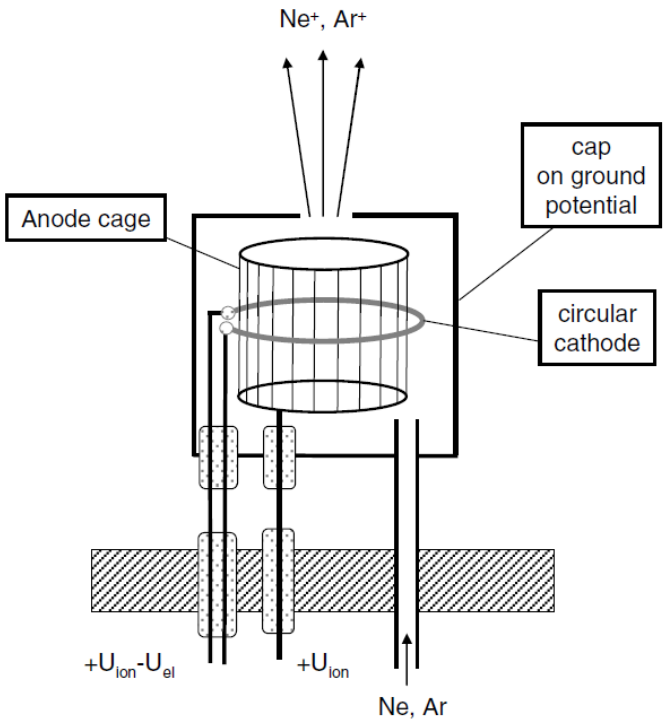

Figure 2.5. A diagram of a sputtering ion gun [95].

2.3. Electron Paramagnetic Resonance

EPR is a sensitive technique designed to study systems with unpaired electrons such as paramagnetic centers on several oxide surfaces. These paramagnetic centers may include surface defects, inorganic or organic radicals, metal cations or supported metal complexes and clusters [96]. The basic theory of EPR is based on electron Zeeman interaction. Electron acts as a bar magnet

due to its charge and angular momentum. The magnetic moment associated with the electron spin, μ_e, is given by

$$\mu_e = -g\mu_B S \tag{2.8}$$

where g is the g-factor of the unpaired electron, S is the spin angular momentum of the electron, and μ_B is the Bohr magneton and is given by

$$\mu_B = \frac{e\hbar}{2m_e} \tag{2.9}$$

where e is the electron charge, $\hbar$ is the rotational Planck's constant, and m_e is the electron mass. When an external magnetic field is applied to a system of unpaired electrons. The magnetic moment interacts with the applied magnetic field, and the energy of interaction is given by

$$E = -\mu . B_\circ \tag{2.10}$$

If the field is applied along the z-direction, the energy of interaction simplifies to

$$E = g\mu_B B_\circ M_s \tag{2.11}$$

where $M_s = \pm\frac{1}{2}$. So, in the absence of the magnetic field these two energy states are degenerate, however, when the magnetic field is applied the degeneracy is lifted and the spin states splits with an energy separation proportional to the magnitude of the magnetic field applied, as shown in figure (2.6). The energy separation is given by

$$\Delta E = h\nu = g\mu_B B_\circ \tag{2.12}$$

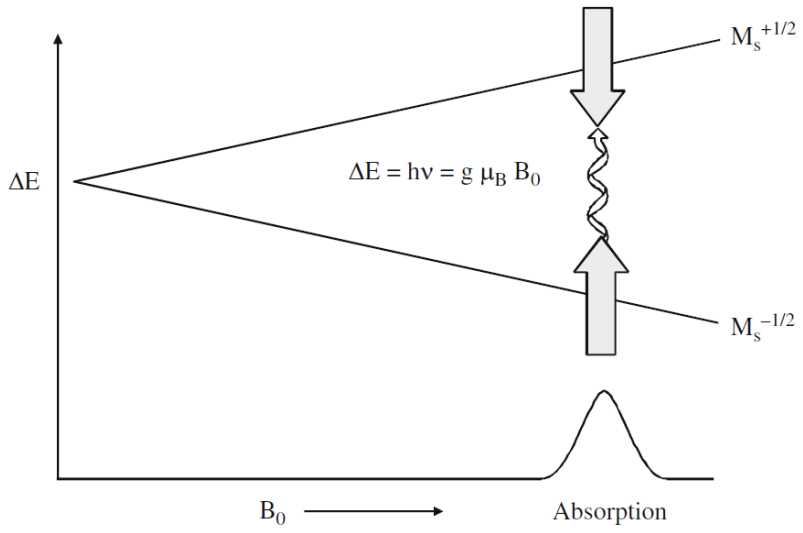

Figure 2.6. Diagram of the energy separation of the two spin states as a function of magnetic field [97].

The peak shown in figure (2.6) is due to electron absorbing electromagnetic radiation. EPR spectra are obtained by applying an electromagnetic radiation with a constant frequency while the magnetic field is scanned. Absorption of energy takes place when the magnetic field tunes the two spin states [97]. That is, when the separation of energy matches the energy of the applied radiation. For organic radicals, the magnetic field used is in the range of 3400 G which correspond to electromagnetic frequency of 9-10 GHz which falls in the microwave frequencies and is known as X-band frequency.

The EPR signal produced in X-band is very small due to very small net magnetization and the small magnetic field perturbing the spin magnetization [97]. Therefore, EPR spectroscopy uses phase sensitive detection to improve the sensitivity of the spectrometer. This technique presents the spectrum as a first derivative, as shown in figure (2.7). The peak of the absorbance spectrum corresponds to the first derivative spectrum crosses the zero point. Interestingly, this point is the g-factor. Rearranging equation (2.12) gives us the g-factor

$$g = \frac{h\nu}{\mu_B B_\circ} \tag{2.13}$$

The value of the g-factor gives information on the electronic structure of the radical, since unpaired electrons are influenced by the neighboring atoms and that consequently affects the value of the g-factor [97]. The g-factor for a free electron is 2.00232 while for organic radicals it is 2.0023 if it is carbon-centered radical, and 2.004 if the radical is oxygen-centered. For metal ions, the geometry of the complex affect the g-factor, the g-factor can range from 1.96-2.3 [97].

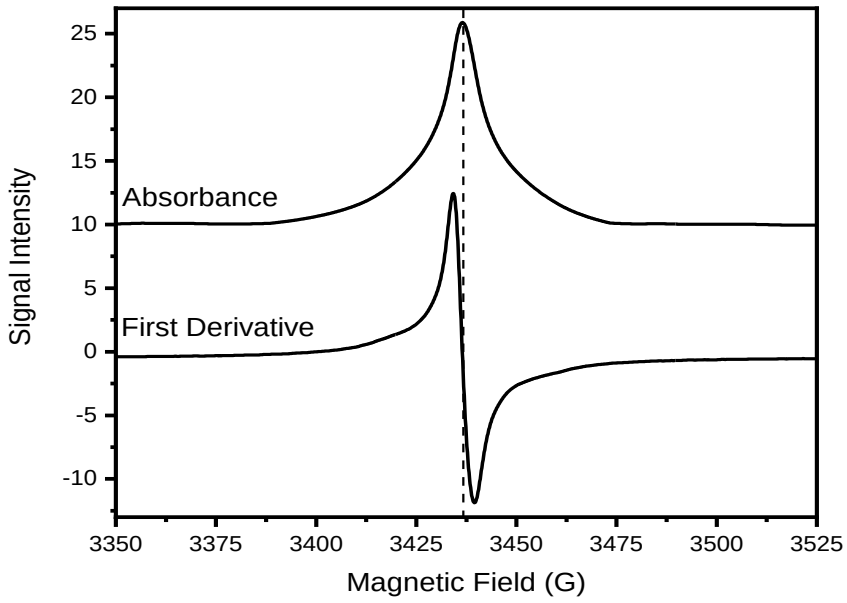

Figure 2.7. Absorbance spectrum and its first derivative EPR signal. The dashed line defines the g-factor of the observed signal.

Another useful information that can be obtained from EPR signal is the spin density. The calculation of spin density determines the number of spins in a certain volume per unit mass. This parameter is particularly important for the study of EPFRs because it enables one to obtain the decay profiles of each formed radical. For some EPFRs, decay profiles can show more than one decay rate, thus giving information about the number of radical formed. Using the decay rates, the 1/e lifetimes can be determined. Spin density can be calculated by double integrating the area under

the first derivative signal and compare it to a standard, the commonly used is 2,2-diphenyl-1-picrylhydrazyl (DPPH). The number of spins is then divided by the mass of the sample in grams to obtain spin density.

2.4. Surface Science Techniques

Surface science techniques enable us to study the electronic structure of EPFRs on a nanoscale. Some techniques can be performed on powder samples while others require single crystal. Chapter 4 in this dissertation discusses the changes in the electronic structure of a single crystal metal oxide used as a model system for powders and is known to be active in forming EPFRs. The main advantage of using single crystal is that the surface structure can be identified using a surface technique as LEED.

2.4.1 Low Energy Electron Diffraction (LEED)

LEED is a very sensitive surface science technique that is widely used to determine the cleanliness and order of the surface of single crystals prior to their use in an experiment. The sensitivity of this technique arises from the use of low energy electrons (~150 eV). Electrons with this energy possess a wavelength of ~ 1 Å which is smaller than the typical interatomic spacing, therefore they interact with the topmost surface atoms. Figure (2.8) show a schematic diagram of LEED set-up. An electron gun generates an electron beam with variable energy (typically from10-500 eV), the electron beam strikes the surface of the sample causing the electrons to backscatter from the surface of the sample onto a system on grids. The elastically scattered electrons are accelerated toward a fluorescent screen and producing a LEED pattern. Grids G2 and G3 are held at an adjustable negative potential to reduce the bright and diffused background caused by the inelastically scattered electrons. The pattern of LEED spots can be used to obtain information about surface symmetry or surface reconstruction [98].

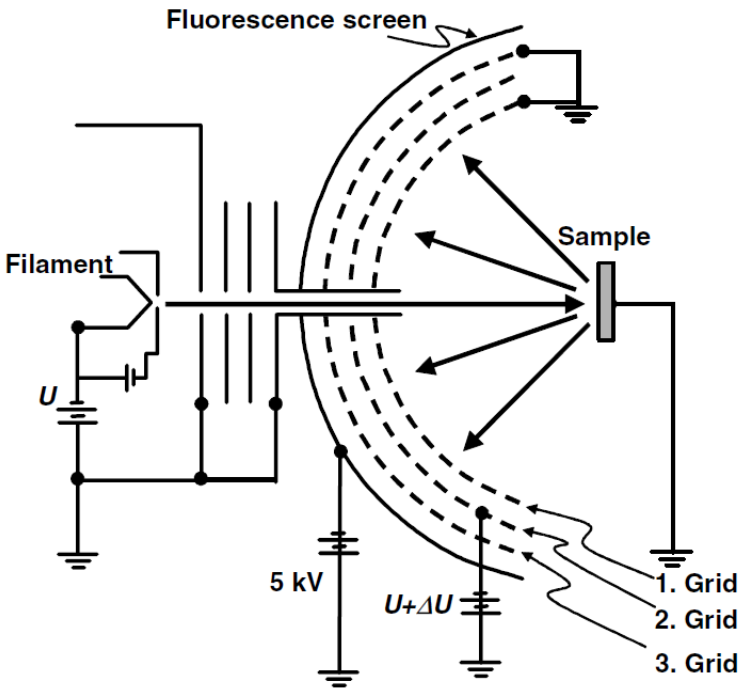

Figure 2.8. Schematic diagram of LEED set-up [95].

The LEED pattern observed on the fluorescent screen is a representation of the surface reciprocal lattice. The atomic spacing between the periodic features at the surface can be calculated using Bragg's law:

$$n\lambda = d\ sin\theta \tag{2.14}$$

where n is the order of diffraction, λ is the wavelength of the electron beam, d is the spacing between atomic planes, and θ is the angle of diffraction between the incident wave vector and the backscattered beam. The wavelength of the electron beam is related to the electron beam energy through de Broglie's equation which is given by

$$\lambda = \frac{h}{\sqrt{2mE}} \tag{2.15}$$

where h is Planck's constant, m is the electron's mass, and E is the electron beam energy. Thus, increasing the energy of the electron beam increases the number of the spots observed on the screen.

The intensity of LEED spots can aid in determining the order of the surface, that is, if the surface is well-ordered the spots will appear sharp and intense with low intensity background. On the other hand, the existence of surface defects or imperfections results in low intensity spots with increase in background intensity [99]. Figure (2.9) shows a comparison between two different terminations of the same single-crystal. The subsurface cation vacancy (SCV) reconstruction have all LEED spots with similar intensity while spots at (3/2, 1/2) for Fe-dimer surface are much weaker [92]. More information can be obtained by probing the intensity distribution across the width of a spot [99]. This investigation of spot intensity is called LEED Spot Profile and is used to mainly probe surface imperfections [99]. Unfortunately, spot profiles do not reveal the atomic arrangement within a surface unit mesh. Therefore, the atomic positions are determined using I-V curves which analyze spot intensity as a function of electron beam energy [99]. This process involves performing a calculation consistent with the symmetry of the LEED pattern, the calculated I-V curves are then compared with the experimental results. Based on this comparison, the proposed atomic arrangement model can be adjusted and new calculations are performed until satisfactory agreement is obtained [99]. This process is beyond the scope of this work.

2.4.2 Photoemission Spectroscopy

Photoemission spectroscopy is a very powerful tool to probe the electron density of both bulk and surface states depending on the kinetic energy of the emitted photoelectron. It provides information about the chemistry, organization, morphology, and electronic structure of the surface [100]. The basic principle of photoemission relies on photoelectric effect which was discovered by

Hertz and Hallwachs in 1880s. In 1905, Einstein utilized Planck's quantization of energy and explained their observations. In photoelectric effect, electrons in a solid with a binding energy E_B

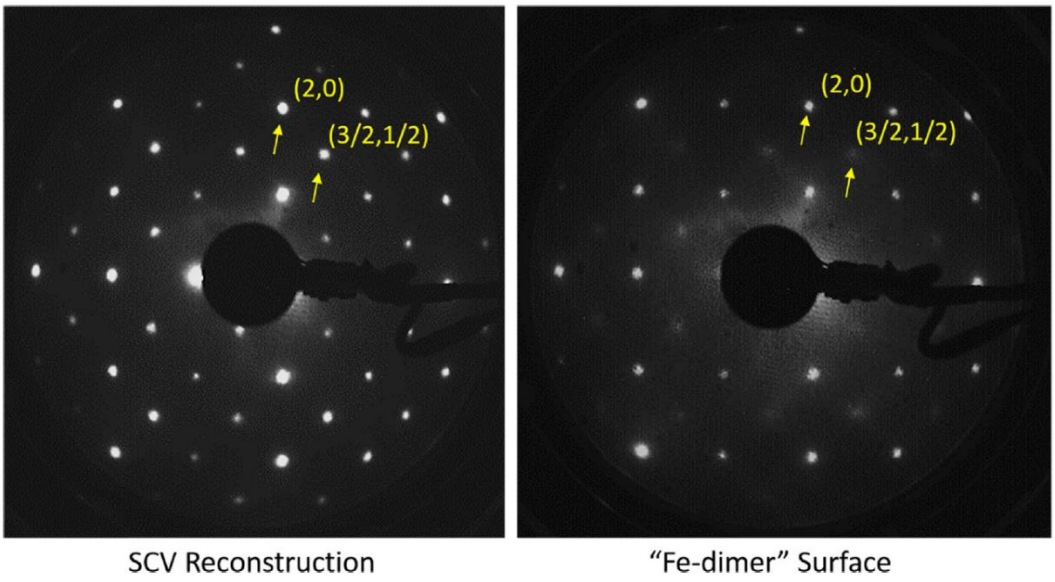

Figure 2.9. LEED patterns acquired at an electron energy of 90 eV of subsurface cation vacancy (SCV) reconstructed surface (left) and Fe-dimer surface (right) [92].

absorb photons with energy $h\nu$ and become photoexcited. Photoelectrons can escape the surface of the solid, if the photon energy overcome the work function ϕ of the solid. The photoelectron leaves the surface with a kinetic energy E_{kin} which is given by

$$E_{kin} = h\nu - E_B - \phi_s \tag{2.16}$$

The emitted photoelectron carries information about the chemical composition and concentration of the atomic species on the surface by identifying the binding energy and height of the observed photoelectron peaks. The distinction between Ultraviolet Photoemission Spectroscopy (UPS) and X-ray Photoemission spectroscopy (XPS) depends on the energy of the incident photons (light source). In XPS, the photon energy ranges between 200-1500 eV, whereas for UPS photon energy is 10s of eV. However, UPS is more sensitive in probing valence structure

than XPS because the cross-section of photoelectron emission from shallow valence band levels is very low at typical XPS photon energies [99]. Therefore, XPS is more suitable in probing core levels.

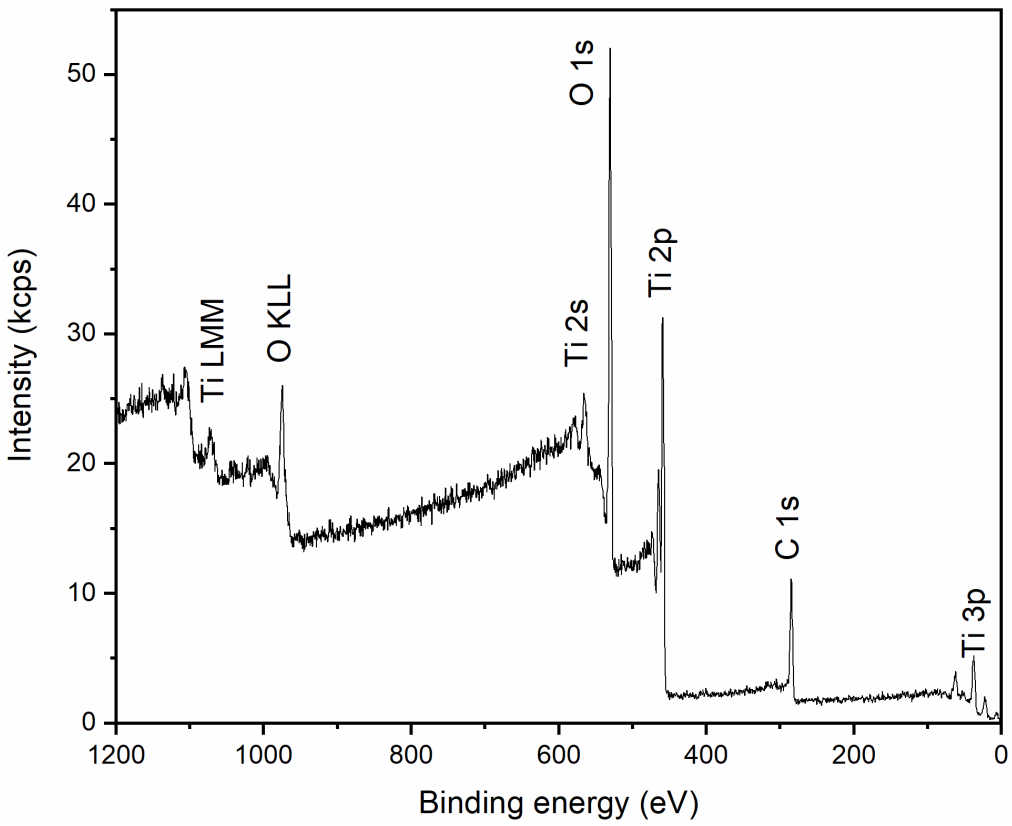

Figure 2.10. XPS survey spectrum of TiO_2.

2.4.2.1. X-ray Photoemission Spectroscopy (XPS)

In this technique, photons from X-ray source impinge on the surface of the sample to be examined resulting in the emission of photoelectrons after direct transfer of the photons' energy to core-level electrons. Photoelectrons, that manage to escape from the sample surface, are then separated with respect to their energy and are counted. The kinetic energy of the emitted photoelectron is related to the binding energy of the electron through equation (2.16), and an energy spectrum is acquired as the one in figure (2.10).

Measurement of the binding energy, E_B, of the photoelectron is very critical since it provides information on the electronic structure of the surface. Binding energy of the electron in an atom, and hence the ejected photoelectron, is affected by any change in the nuclear charge resulting from any alteration of the electron distribution on the atom. Formation of covalent or ionic bonds between atoms changes the electron distribution and consequently the binding energy of the ejected photoelectron change accordingly. Thus, XPS is very sensitive to chemical shifts.

To ensure accurate measurement of E_B, XPS instrument has to be properly calibrated. This purpose is achieved by grounding both the spectrometer and the conducting sample. By this means, the Fermi levels (E_F) of both the conducting sample and the spectrometer align. Figure (2.11) shows schematic representation of the energy scales in photoemission experiment. Here ϕ, the work function, is defined as the minimum energy required for an electron to be ejected from the solid to vacuum. Equation (2.16) requires measuring the work function of the sample to obtain E_B. To ease the operation, the dependence on samples' work function, ϕ_s, needs to be replaced by XPS instrument's work function, ϕ_A, and this is achieved by constructing XPS instrument with a work function values less than that of any sample previously exposed to air [101]. Now the kinetic energy of the emitted photoelectron becomes

$$E_{kin} = h\nu - E_B - \phi_s - (\phi_A - \phi_s) \tag{2.17}$$

$$\therefore\ E_{kin} = h\upsilon - E_B - \phi_A \tag{2.18}$$

XPS instruments are calibrated by obtaining high resolution scans of Cu $2p_{3/2}$, Ag $3d_{5/2}$, or Au $4f_{7/2}$ after the elemental sample is clean from surface oxides and adventitious carbon [101]. For insulators, the XPS spectrum will shift toward higher binding energy and this is because the Fermi levels of both the sample and the instrument does not align. Therefore, binding energy scale can

be calibrated by sitting C 1s peak arising from adventitious carbon which may present in UHV system. The common used value for adventitious C 1s is 284.7 ± 0.1 eV [101].

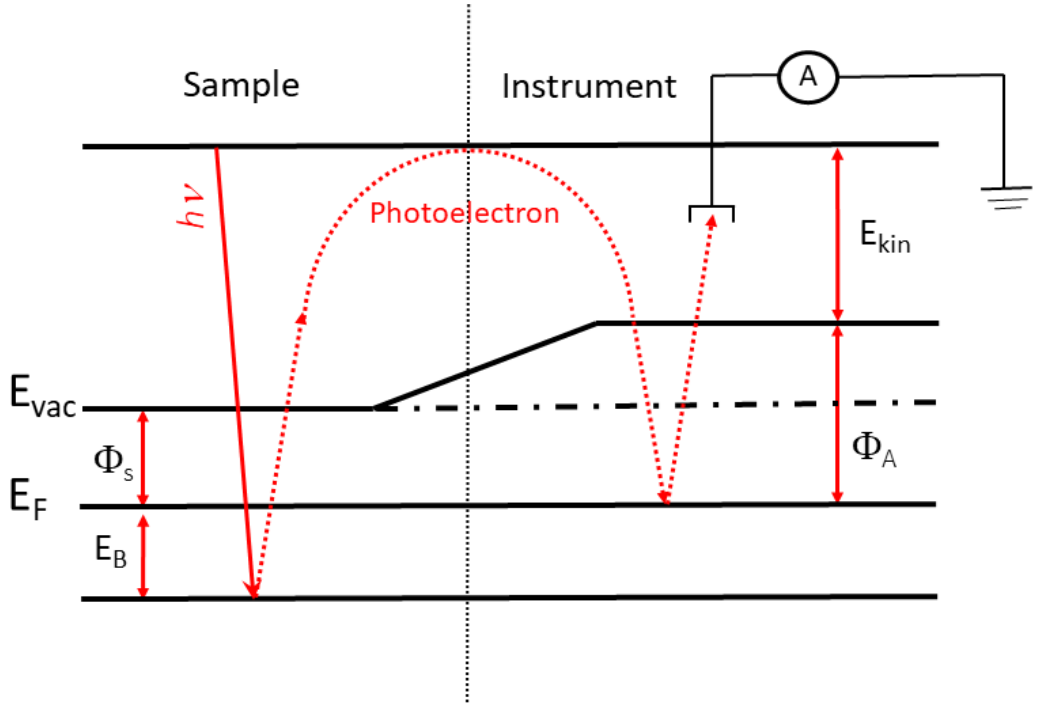

Figure 2.11. Schematic showing the relation between conducting sample and XPS instrument parameters in a photoemission experiment.

Binding energy is the energy required to remove an electron from its orbital. The closer the electron to the nucleus, the higher the binding energy becomes. Binding energy is affected by the change of the electron distribution due to the formation of chemical bonds between the atoms. This type of change in the binding energy is called chemical shift and is observed, for instance, in the case of varying the oxidation state of an element. As the oxidation state increases, more oxygen are bonded to the element, thus drawing more electrons to it due to its high electronegativity. This results in the element atom becoming more positively charged, and hence its binding energy increases [100]. However, this may not hold true for some of the oxides due to the dominance of the final state effects over the initial state effects.

The binding energy measured by XPS is not the same as the binding energy of the photoelectron in its orbital level in the atom. The reason for this is that other electrons in the ionized atom do not remain frozen during the photoemission process. After core hole creation, electrons tend to rearrange themselves to shield or minimize the energy of the ionized atom [100]. This energy is called relaxation energy. Thus, if we call the ground state of the atom prior to photoemission by initial state, and the state of the atom after photoemission by final state, then the binding energy observed by XPS is the difference between the final state energy and the initial state energy. Figure (2.12) show an illustration of all the initial and final effects that contribute to the change in the observed binding energy.

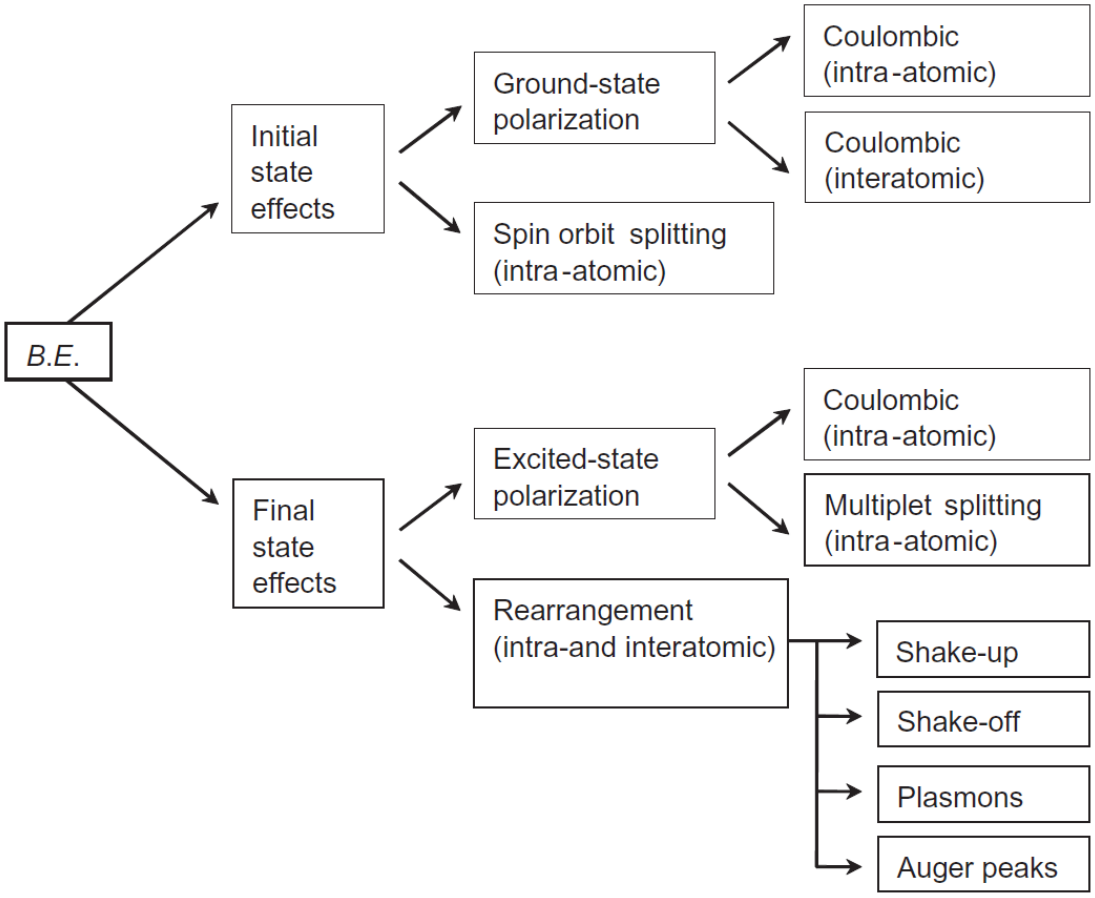

Figure 2.12. Illustration of the initial and final state effects that can be experienced by photoelectron [102].

Initial state effects arise from the electronic structure of the atom where the photoelectron is ejected. These effects are induced mainly by the charge density experienced by photoelectron. Changes that take place in the oxidation state of the ionized atom (prior to photoemission), bonding with neighboring atoms, as well as electronegativity of neighboring atoms all alter the charge density surrounding the emitted photoelectron [102].

Spin-orbit splitting is considered an initial state effect since it is an atomic property. This effect arises from the coupling of the magnetic field set up by an electron spinning around its own axis with that of an electron spinning around its nucleus (for $l > 0$) [102]. Because electron spin has two values ($\pm\frac{1}{2}$), two photoelectron peaks are observed for the same orbital angular momentum, l, and are described by their total angular momentum, J. The level with higher J has lower binding energy and the number of electrons in each level scales as $2J + 1$. Table 2.1 presents the intensity ratios of spin orbit split doublets.

Table 2.1. Parameters of spin-orbit coupling.

Orbital	Orbital angular momentum (l)	Total momentum $J = l \pm s$	Intensity ratio $(2J + 1)$
s	0	$\frac{1}{2}$	–
p	1	$\frac{1}{2}, \frac{3}{2}$	1:2
d	2	$\frac{3}{2}, \frac{5}{2}$	2:3
f	3	$\frac{5}{2}, \frac{7}{2}$	3:4

Final state effects arise due to the formation of a core hole in the ionized atom after the ejection of the photoelectron. The core hole itself can induce electrostatic and magnetic effects, which in turn affect the measured binding energy of the photoelectron. These effects are called multiplet or exchange splitting and it results from the interaction of the unpaired electron introduced by the formation of the core hole and any localized unpaired valence electron. Similar to spin-orbit splitting, the magnetic fields arising from the spin of these two electrons couple resulting in the splitting of the energy of the relevant orbitals which in turn splits the photoelectron peak in the XPS spectrum. It should be noted that multiplet splitting affect unpaired electrons in all orbitals including S orbitals. Also, the multiplet splitting energy separation increases with the decrease of the binding energy of the interacting core electron [102]. One should also note that for photoelectron peaks experiencing spin orbit splitting, only the main peak (higher J value) suffer multiplet splitting [102].

The rearrangement process that takes place due to the core hole formation also induces final state effects. Rearrangement originates from the transfer of energy associated with the decay of core hole. Rearrangement process that occur within the timescale of photoelectron emission produce observable spectral features such as photoelectron peak asymmetry, satellite peaks, plasmon loss peaks, and Auger electron peaks [102].

Auger electron emission along with fluorescence are the main processes by which core hole decays. Figure (2.13) show a schematic diagram of both processes. Auger electron emission is a three-electron process, therefore, it is observed for all elements except for H and He. The first electron is the ejected photoelectron, the core hole produced is then filled with the second electron which is an electron from a higher energy state (L_1 in figure 2.13). In fluorescence, the energy difference resulted from filling the core hole is emitted as photons whereas in Auger, these photons

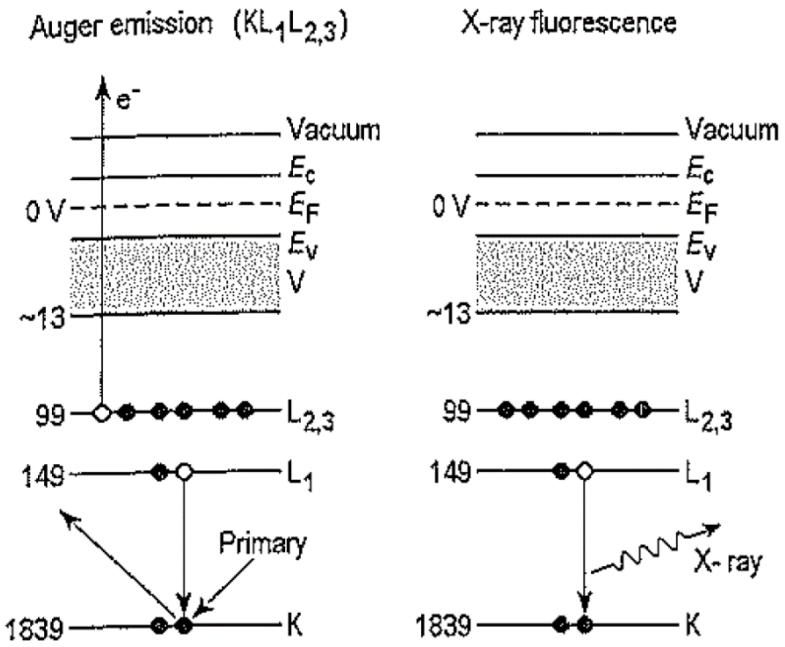

Figure 2.13. Schematic representation of the two process by which core hole is dissipated [99].

are absorbed by the third electron which is finally emitted and observed in the XPS spectrum. Both processes are comparable in the typical XPS photon energies, however, for photon energies less than 500 eV, fluorescence becomes negligible [99]. Auger electron emission adheres to the following selection rules:

$$\Delta l = \pm 1, \Delta m_l = 0, \pm 1$$

However, forbidden transitions may be observed in XPS spectrum with weak intensities compared to other Auger transitions [102]. The kinetic energy of the emitted Auger electron (for $KL_1L_{2,3}$ transition) is given by

$$E_{KL_1L_{2,3}} = E_K - E_{L_1} - E_{L_{2,3}} - \phi_A \qquad (2.19)$$

where ϕ_A is the work function of the XPS instrument if the sample is in good electrical contact. Also, $E_K - E_{L_1}$ represent the photon energy absorbed by the third electron. It should be noted that Auger transition spectra are normally plotted on a kinetic energy scale because the binding energy scale of the XPS depends on the energy of the incident X-rays, whereas the kinetic energy of the

Auger transitions depends solely on the kinetic energy of the difference between the two levels accessed and the instrument work function as seen in equation (2.19). Therefore, changing the photon source will change the binding energy at which the Auger transition is observed [102].

Although Auger electron emission is a final state effect, it is used to provide information on the samples' speciation. Figure (2.14) shows Cu $L_3M_{45}M_{45}$ Auger transition of Cu. As can be seen from the figure that different oxidation states of Cu display different peak structures as well as different peak positions. Therefore, some Auger transitions are used to differentiate between the different oxidation states of different oxides.

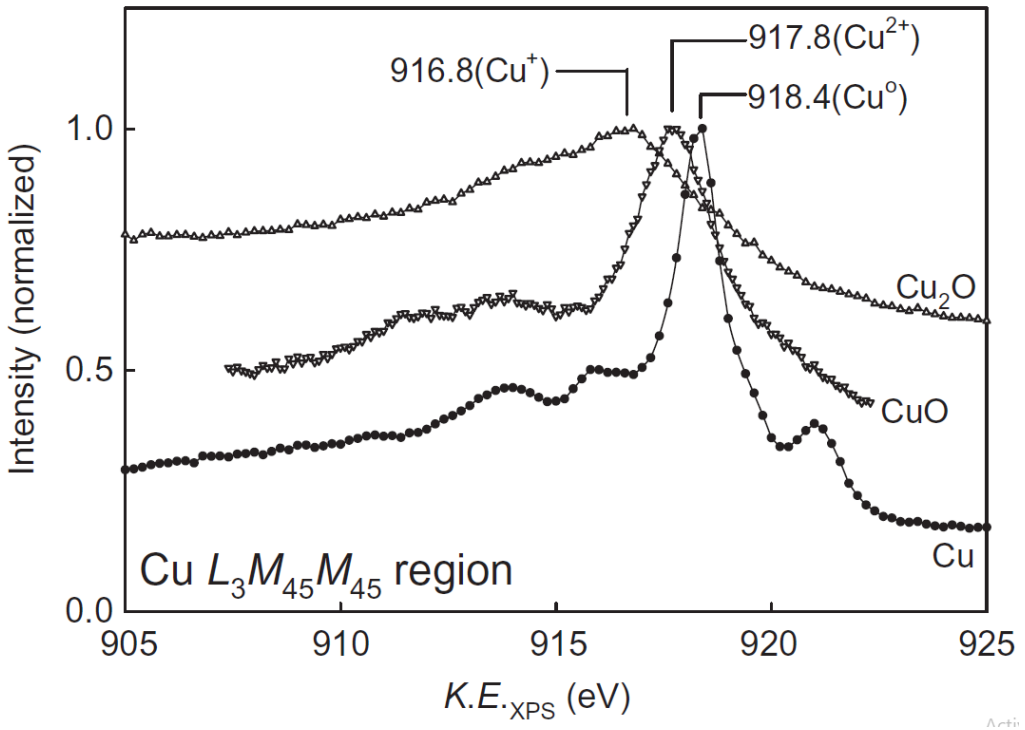

Figure 2.14. Cu $L_3M_{45}M_{45}$ Auger transition induced by X-ray photoemission [102].

Another core hole induced rearrangement is the shake-up satellite. In this type of rearrangement, the departing photoelectron excites a valence electron into unoccupied orbitals resulting in a decrease in the kinetic energy of the photoelectron. This process affects the spectral

features by introducing either an asymmetry of the main photoelectron peak and/or observance of new features called satellites [102]. Similar to Auger transitions, shake-up satellites are used to provide information about the sample's speciation. Figure (2.15) shows the Cu 2p core spectra of different copper oxides. As can be seen from the figure, shake-up satellites help distinguish between Cu ^{0}, Cu $^{1+}$, and Cu $^{2+}$. Also, the binding energy of Cu $2p_{3/2}$ of CuO is observed at a higher binding energy compared to Cu and Cu_2O due to the strong shake-up satellite.

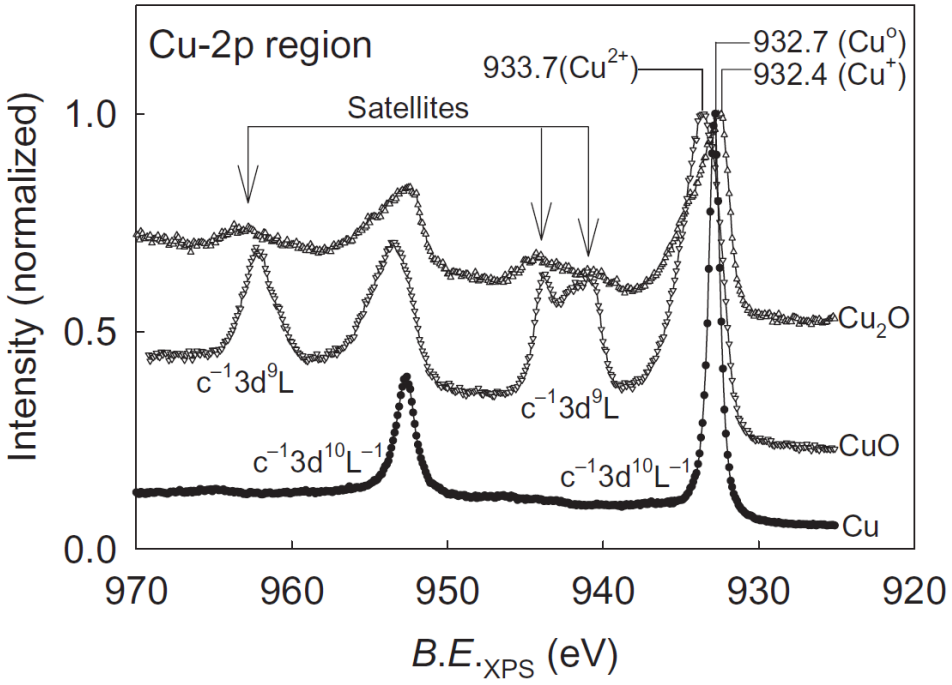

Figure 2.15. X-ray photoelectron spectra of Cu 2p region of metal Cu and its oxides [102].

The other type of satellites observed in XPS is shake-off satellites. In this process, the ejected photoelectron excites a valence electron to unbound continuum states located above the vacuum level [102]. The main difference between shake-off and shake-up satellites is that electrons leave the sample in shake-off process while they are merely excited to a higher energy level. Shake-off satellites are observed in XPS spectrum as a broadening of the photoelectron peak or

contribute to the inelastic background at a higher binding energy with respect to main core level peak [102].

The last final state effect discussed in this dissertation is the Plasmon excitations. Plasmons are collective oscillations of the free electron gas in the conduction band. Therefore, the ejected photoelectron excites Plasmon formation in samples that either contain a high density of free electrons in the conduction band like metals, or in insulators if the photoelectron excites valence electrons to the conduction band, as the case of TiO_2 as shown in figure (2.16) [102]. These excitations take place because of the change in the chare density either due to the fast passage of the ejected photoelectron or due to formation of the core hole [102]. Plasmon excitations are observed in the XPS spectrum as loss features at higher binding energy with respect to the main photoelectron peak.

Core level photoelectron peak, which does not experience rearrangement effects, is expected to be symmetric in shape with a peak width (FWHM) which is defined by [102]

$$FWHM = \frac{h}{\Gamma} \tag{2.20}$$

where h is the Planck's constant in electron-volt-second, Γ is the core-hole life time. Thus, in this case, the lifetime of the core hole is determined by the speed at which Auger processes take place [102]. On the other hand, the intensity of photoelectrons relies on different factors such as the photoelectron cross section, instrument geometry, and the inelastic mean free path (IMFP) [102].

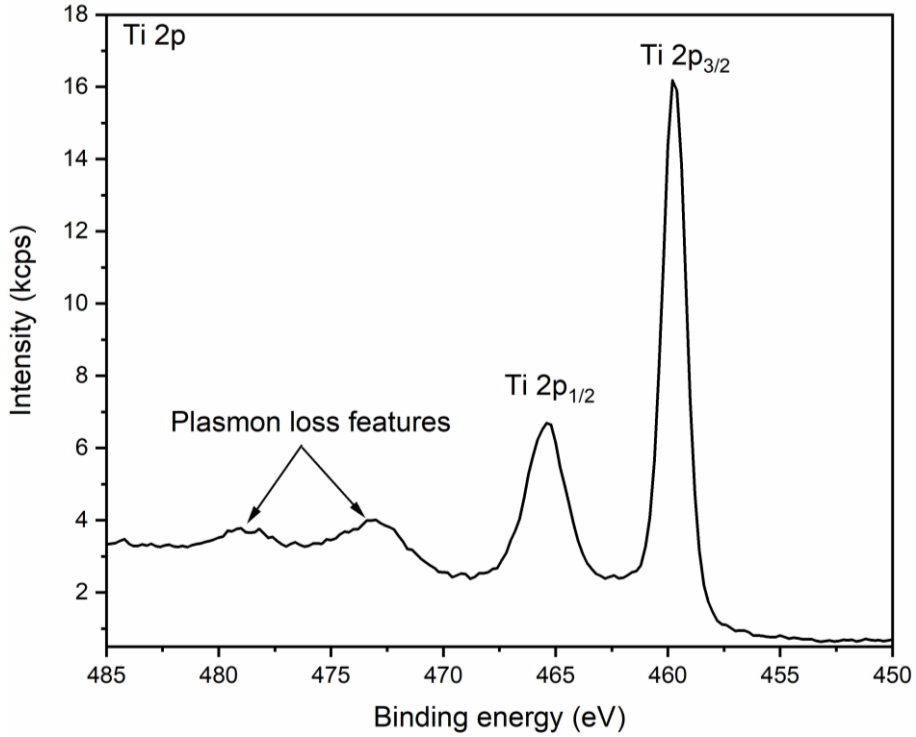

Figure 2.16. X-ray photoemission spectrum of Ti 2p core level of TiO_2.

The photoelectron path length is defined by the elastic and the inelastic scattering events encountered by the photoelectron. The inelastic mean free path is defined as the mean distance traveled by an electron with a kinetic energy (K.E.) in a solid before it loses its energy to its surrounding. The mean free path of the ejected photoelectron depends on its kinetic energy, therefore, if the ejected photoelectron loses energy more than the specified energy resolution of the instrument, the signal becomes part of the background. IMFP accounts for inelastic scattering, however, it should be noted that elastic scattering, although it does not cause loss of energy, it increases the depth from which electrons are ejected. Figure (2.17) shows the relation between IMFP of electrons in solid as a function kinetic energy approximated by TPP-2M relation. From this relation we see that the path length of electrons in solid increases with kinetic energies above 100 eV.

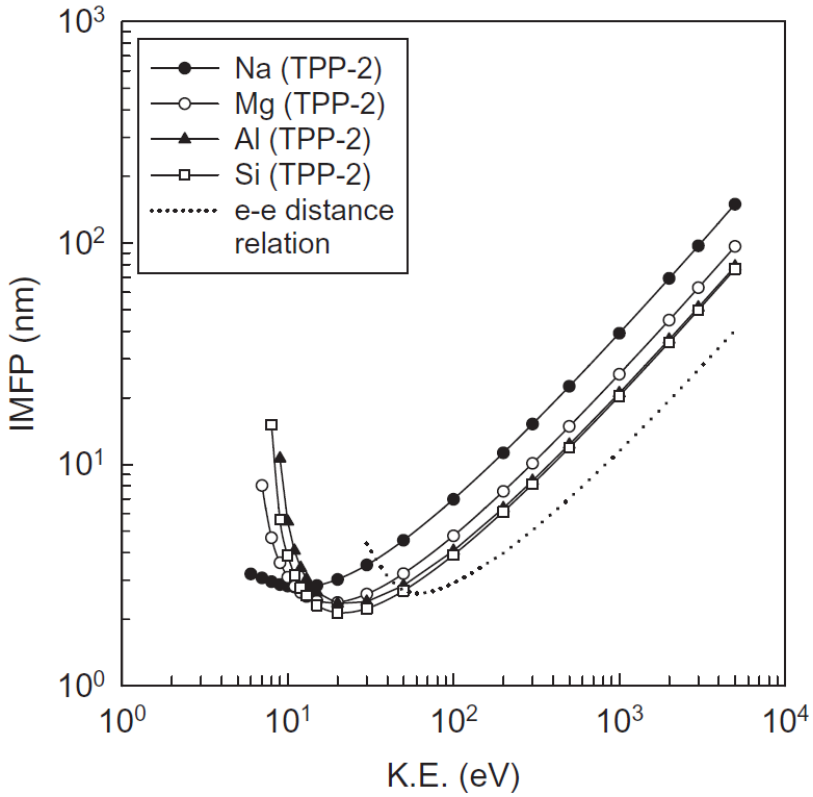

Figure 2.17. Inelastic mean free path of electrons in solid as a function of kinetic energy approximated by TTP-2M [101].

The core level XPS spectra obtained for chapter 3 in this dissertation were performed using an Omicron XM1200 monochromatic X-ray source in combination with Omicron EA 128 hemispherical analyzer while XPS spectra obtained for chapter 4 is performed using Omicron XM1000 monochromatic X-ray source (depicted in figure 2.18) in combination with a SPECS PHOIBOS 150 hemispherical analyzer. The X-ray source contains two thoria-coated tungsten filaments which emit electrons when heated. The electrons are then accelerated toward an aluminum anode with 15 keV generating characteristic X-rays upon electrons' bombardment with the anode. The generated X-rays impinge on a quartz crystal that diffracts the X-rays and allow only X-rays of characteristic Al Kα_1 energy (1486.6 eV) to be focused on the sample. The radius of curvature of the Rowland circle in XM1000 is 500 mm, and the spot size focused on the sample is $1.5 \times 2.5\ mm$ and $2.5 \times 4.5\ mm$ for the short and long filaments, respectively. The ultimate

combined system resolution of the XM1000 source and SPECS PHOIBOS 150 analyzer is ~0.6 eV for a core level XPS peak (Ag $3d_{5/2}$), or ~0.3 eV measured from a metallic sample Fermi edge at low temperature.

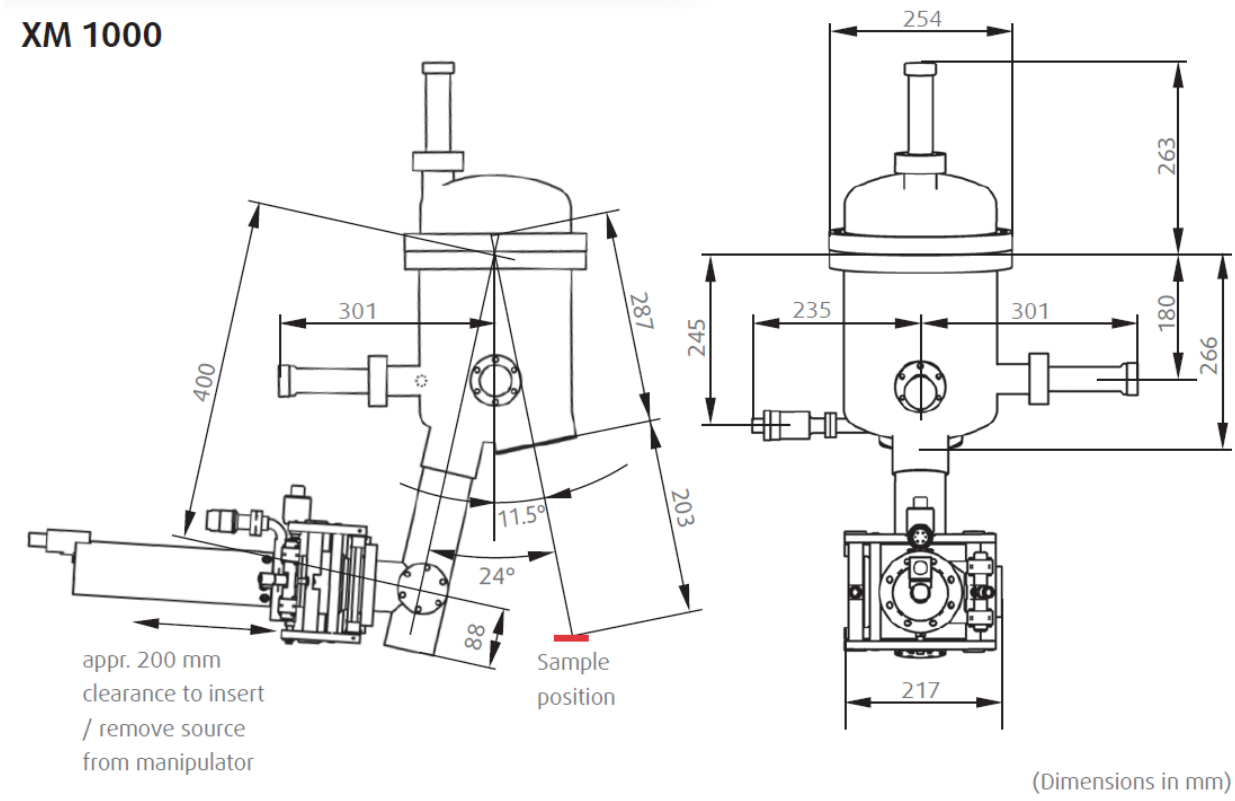

Figure 2.18. Schematic of Omicron XM 1000 X-ray source [103]

2.4.2.2. Ultraviolet Photoemission Spectroscopy (UPS)

UPS has the same basic principles discussed in XPS. It utilizes photons in the ultraviolet spectral range (10 – 50 eV), therefore it is used to study the electronic structure of valance bands in solids as well as adsorbed molecules on the surface. Also, UPS has access to core levels up to the photon energy used. It can also measure the work function of a given material. UPS is more surface sensitive than XPS because the ejected photoelectrons have lower kinetic energy compared to that ejected by X-ray photons resulting in a shorter IMFP and thus stronger signal sensitivity. The ultraviolet radiation source used in typical UPS experiments are either gas charge lamps or

synchrotrons. In laboratory, He discharge lamp is utilized with two intense lines at 584 Å corresponding to He I (21.22 eV) and 304 Å corresponding to He II (40.8 eV). The choice between the two lines is controlled by the gas pressure and discharge current [99]. The narrow linewidth of both UV sources makes the spectral resolution obtained by UPS significantly higher than that of XPS. Hence, the valence levels observed overlapped in XPS will be more resolved in UPS. Valence band photoemission data in this work are obtained by SPECS microwave UV light source (utilizes He II line ~40.8 eV) in combination with a SPECS PHOIBOS 150 hemispherical analyzer.

2.5. Fourier Transform Infrared Spectroscopy

Infrared spectroscopy measures the characteristic vibrational bands of chemical species by absorption of light in infrared range. This technique is very sensitive to molecular composition and can provide information on the type of chemical species present on the surface as well as the interactions between neighboring molecular components. The IR absorption process is achieved if the radiation frequency matches the natural frequency of a particular normal mode of vibration and the vibrational excitation causes a change in the dipole moment of the molecule. Therefore, the selection rule for IR spectroscopy requires a change in the dipole moment during the vibration to be IR active [104].

Vibrational excitation leads to stretching and bending vibrational modes. Stretching modes involve changes in bond length between atoms in the molecule while bending modes involve changes in the bond angles between the atoms. However, stretching modes can be symmetric or asymmetric. For CO_2, the net change of dipole moment in the symmetric stretching mode is zero whereas it is nonzero for the asymmetric stretch modes. Figure (2.19) shows vibrational modes of carbon dioxide. Therefore, symmetric stretching mode is IR inactive while the asymmetric stretch modes is IR active.

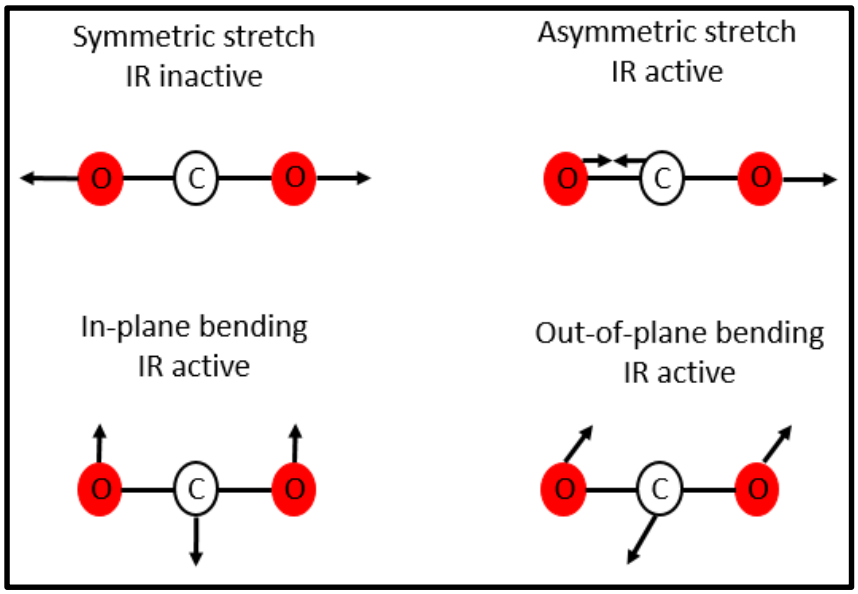

Figure 2.19. Stretching and bending modes of CO_2 molecule.

Fourier Transform Infrared spectroscopy (FTIR) utilizes an interferometer and a computer. Most of the commercially available FTIR spectrometers use Michelson interferometer. Figure (2.20) depicts a schematic diagram of Michelson interferometer. The principle of operation can be described by first considering the source which emits infrared light of all wavelengths. A collimating mirror collimates the infrared light to the beam splitter which equally divides the amplitude of the beam with 50 % is transmitted to the moving mirror and the other 50 % is reflected to the fixed mirror. The light reflected from both mirrors recombines at the beam splitter and experiences interference, then it passes through the detector. The constructively interfered light causes the detector response to reach a maximum. This is achieved when the path difference between the two interfering beams is an integral number of the wavelength. The path difference is controlled by the motion of the mirror. The interferogram is a record the detected signal intensity plotted against the optical path difference of the two interfering beams. It should be noted that

sampling takes place before the detector and its optics. Fourier transform is performed on the interferogram to obtain the spectrum. The spectrum S as a function of frequency ν is given by

$$S(\nu) = \int_{-\infty}^{+\infty} I(x)\, e^{+i2\pi\nu x}\, dx = F^{-1}[I(x)] \tag{2.21}$$

where x is the path difference

$$I(x) = \int_{-\infty}^{+\infty} S(\nu) e^{-i2\pi\nu x}\, d\nu = F[S(\nu)] \tag{2.22}$$

Equation (2.21) is called the inverse Fourier transform and equation (2.22) is called the Fourier transform. The inverse Fourier transform integral converts the interferogram $I(x)$, which is a function of path difference to $S(\nu)$ spectrum, which is a function of frequency, ν.

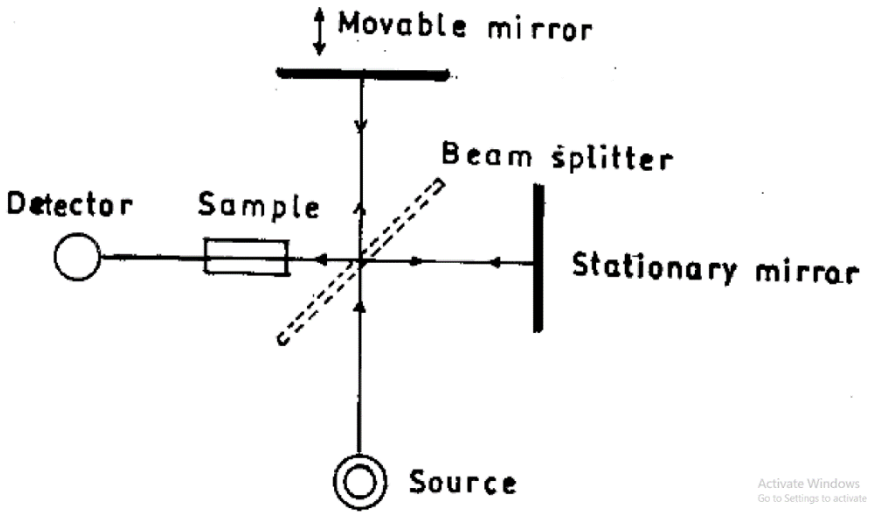

Figure 2.20. Schematic diagram of Michelson interferometer [105].

IR spectroscopy has different sampling modes. The work in this dissertation used attenuated total reflectance (ATR) mode. In this mode the sample is placed in a very close contact with a prism that has a refractive index higher than that of the sample. The IR radiation passes through the prism and become totally reflected if the angle of incidence is greater than the critical

angle. Moreover, the magnitude of the angle of incidence controls the number of internal reflections within the ATR prism, see figure (2.21). At each point of reflection in prism, an evanescent wave is created and extends into the sample. The interaction between the sample and the electric field of the evanescent wave attenuates the intensity of the reflected IR beam due to the absorption of the electric field. Thus, the evanescent wave decays exponentially into the sample with distance from the surface, z, of the prism according to

$$E = E_{\circ} e^{-z/d_p} \tag{2.23}$$

Where E and $E_{\circ}$ are the electric field after and before the exponential decay, respectively. d_p is the penetration depth of the evanescent wave and is determined by

$$d_p = \frac{\lambda}{2\pi n_1 \sqrt{[sin^2\theta - (\frac{n_2}{n_1})]^2}} \tag{2.24}$$

where λ is the wavelength of the IR radiation, θ is the angle of incidence, n_2 and n_1 are the refractive indices of the sample and the prism, respectively. The penetration depth is on the order of microns and that makes ATR ideal for studying surfaces and thin films.

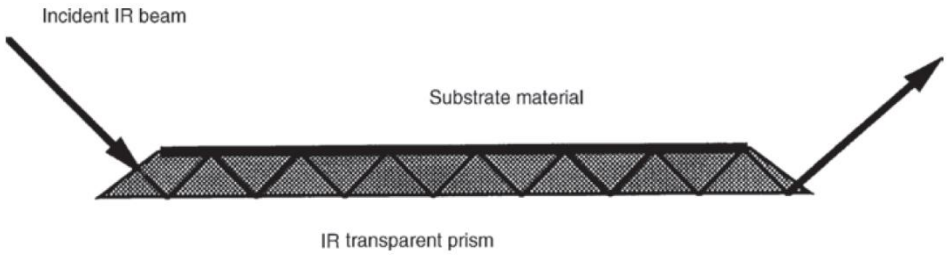

Figure 2.21. Schematic illustrating ATR mode of IR sampling [106].

2.6. Solar Simulator

Solar simulator is used to replicate the irradiance and spectrum of the sun. Due to the atmosphere, light from the sun can be divided into direct radiation which comes directly from the sun and scattered radiation in which light from the sun experiences absorption and scattering with air molecules and dust particles in the atmosphere. The main purpose of the solar simulator is to mimic the natural solar spectral distribution of the sunlight for different latitudes. In order to produce artificial sunlight, one needs to consider air mass (AM). Air masses are the gases and particles which persist in the atmosphere and attenuate the solar intensity as the sunlight propagates through the atmosphere. AM is defined as the path length of the direct sun beam through the atmosphere [107]. It can be expressed as the reciprocal of the cosine of the zenith angle. Figure (2.22) depicts the relation between AM and the zenith angle.

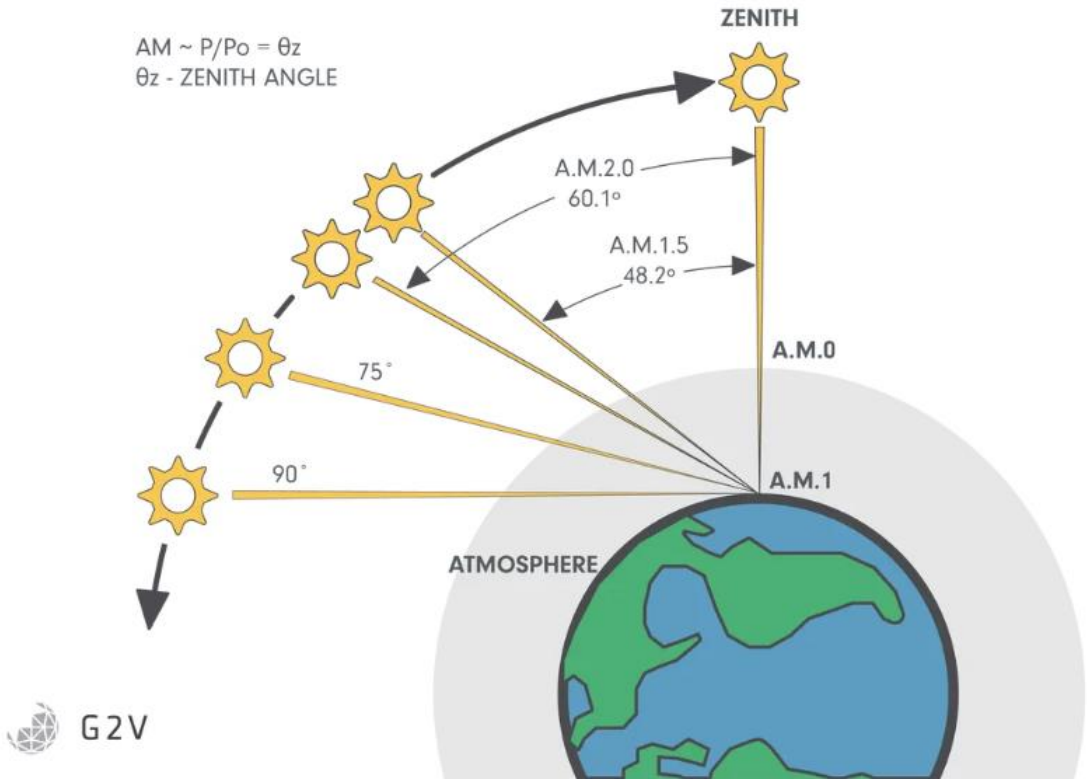

Figure 2.22. Air masses at different zenith angles [107].

Sunlight that travel through space, and does not encounter earth's atmosphere, experiences no change in solar spectrum. The air mass that expresses this type of sunlight which did not interact with earth's atmosphere is called AM0. Furthermore, direct radiation of the sun which travels vertically through the atmosphere is known as AM1 and is useful to estimate the performance of solar cells in equatorial and tropical regions [107]. Moreover, AM1.5 is the most commonly used to identify the performance of the solar cells in the mid-latitudes [107]. It represents a zenith angle of 48.2°. The wide spread of AM1.5 stems from the fact that most world population presents along the mid-latitudes. The American Society for Testing and Materials (ASTM) developed two standard terrestrial solar spectral irradiance distributions [108]. The first one is a standard total spectral irradiance (global) in which the air mass is 1.5 and the spectrum includes the blue sky and the surrounding ground [109]. The second is a standard direct normal spectral irradiance (direct), it is similar to the global spectral irradiance, the difference her is that the sunlight comes from a normal angle on the system and it cannot use the radiation from the blue sky [109]. Figure (2.23) shows a comparison between the different air masses.

Artificial sunlight can be produced by solar simulators. Solar simulators utilize a light source, power supply, optics, and filters. To match the intensity and spectral composition of the sunlight, solar simulators operate by either filtering a broad spectrum of light generated by a light source such as Xenon lamp, or by using narrow-band light sources and combine their outputs to generate the required spectra [107]. The solar irradiated EPFRs in this dissertation utilized Wavelabs Sinus 70 LED based solar simulator with spectral coverage from 365-1100 nm and AM1.5G spectral irradiance.

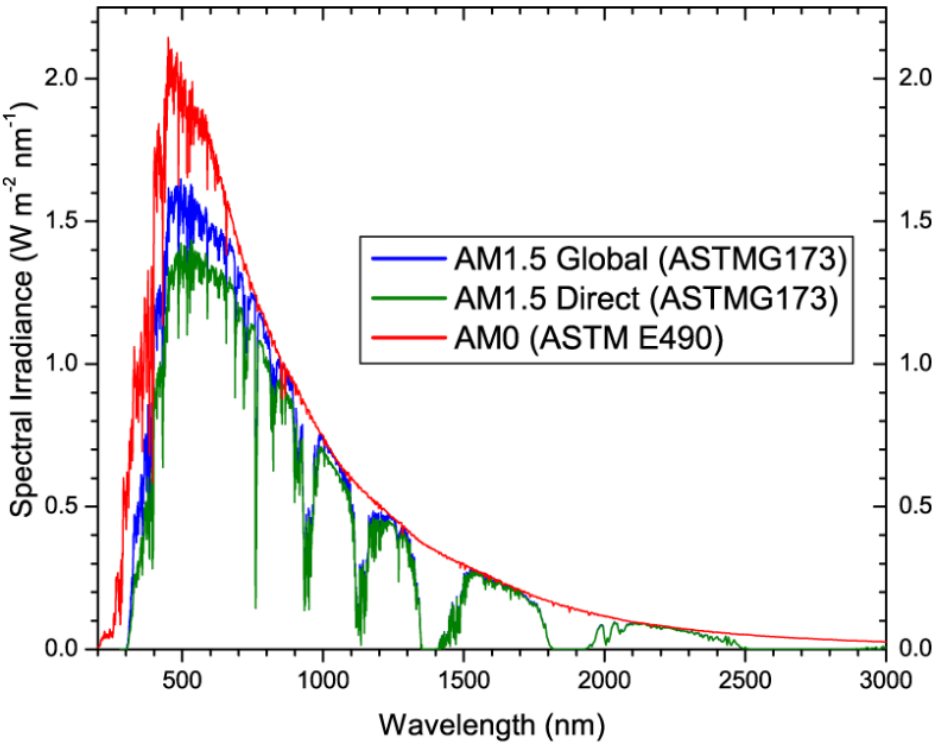

Figure 2.23. Comparison of the spectral irradiance of AM0 and AM1.5 [110] .

Chapter 3. Environmentally Persistent Free Radicals Formation by Phenol Adsorbed on Transition Metal Nanoclusters Systems

3.1. Introduction

The health impacts of airborne particulate matter (PM) are significant [14]. PM is generated by many sources such as refineries, automobile combustion engines, and waste incinerators [39]. The toxicity of PM is not only determined by the size, shape, and composition of PM, but also by the organic molecules associated with PM [14]. Studies have shown that environmentally persistent free radicals (EPFR)-containing PM, primarily those that contain small amounts of transition metal oxides (TMOs), can cause lung and heart damage, since EPFRs can produce reactive oxygen species (ROS) which in turn can cause oxidative stress and cell death in both animal and human [1, 75, 111-113].

EPFRs are free radicals that are known to have much longer lifetimes than typical radicals, with half-lives of hours to days under ambient conditions [14, 39]. EPFRs are formed by the adsorption of organic precursors such as phenol, 2-monochlorophenol (2-MCP), catechol, 1,2-dichlorobenzene and other substituted benzenes on the surface of TMOs at elevated temperatures (275-775 K) [16]. *Ab initio* calculations have shown that EPFRs gain their stability from the synergy of the metals and aromatic compounds [17], which enables the formed radicals to persist in ambient environment [14, 58]. The proposed mechanism of their formation involves initial physisorption followed by chemisorption to the metal ion in which water or HCl is eliminated [16, 114, 115].

As indicated, the chemisorption is generally accompanied by a single or partial electron charge transferred from the organic molecule to the metal cations, and consequently, the metal oxide surface is reduced concurrent with the chemisorbed formation of the organic free radical[17]. In short, EPFRs are a composite organic/metal oxide system.

The signature of EPFRs formation from several organic precursors has been identified by electron paramagnetic resonance (EPR) spectroscopy on different transition metal oxide systems such as CuO/SiO_2 [17], Fe_2O_3/SiO_2 [18], TiO_2 [16], NiO/SiO_2 [19], ZnO/SiO_2 [15], and ZnO [12] nanoparticles (NPs). It has been reported that some metal oxides form F-centers as well as either phenoxyl-type or semiquinone type radicals depending on the type of the organic precursor used for dosing [17, 18]. EPR also showed that EPFRs are thermally activated, that is, the spin density of the organic radical formed was found to increase above a certain temperature for each of the studied systems [17-19].

Other studies have shown that the formation and yield of EPFRs is dictated by the size of supported TMO nanoparticles (NP) [116]. Kiruri et al. have found that the catalytic ability of CuO to generate EPFRs increases with decreasing nanocluster size [117]. Thus, it is expected that NP-sized TMO produces a higher yield of EPFRs, since it offers a larger surface area and hence more active sites for the chemisorption of the organic precursors [118]. It is also reported that NP-sized TMO enhances electron transfer from the organic precursor [116]. However, the increased reactivity of NP-sized TMO due to the improved catalytic ability may consume EPFRs and lead to their decomposition [119]. Accordingly, it is interesting to study the influence and origin of NP-sized pure TMO on the yield of EPFRs.

The change in the oxidation state of TMOs that are known to be active for EPFRs formation was previously studied by various surface techniques. Cu K-edge XANES spectroscopy of Cu (II)O/SiO_2 dosed at high temperature by several organic precursors is found to reduce to a mixture

of Cu (II), Cu (I), and small amounts of Cu (0) [115]. Our group has also employed ultraviolet photoelectron spectroscopy (UPS) on a well-defined single-crystal metal oxide surfaces as TiO_2 (110) [120] and two crystallographic faces of ZnO [121]. A downward band bending, in which bands are shifted toward higher binding energy, has been observed for high temperature adsorption of phenol on TiO_2 (110) suggesting electron donation from the adsorbing molecule and thus the reduction of the metal cation [120]. However, an upward band bending, in which bands are shifted toward E_F, has been observed for both crystallographic faces of ZnO dosed with the same organic precursor at the same temperature indicating electron transfer from the metal oxide surface to the organic, which is in contradiction to what has been proposed in the formation mechanism of EPFRs [121].

Although the stability and persistence of EPFRs in the environment are remarkable, they do decay over longer timescales. Decay studies have been previously performed on the EPFRs formed by phenol dosed metal oxide nano-powders. The 1/e lifetimes, determined by EPR measurements, reported for pure TiO_2 [16] powder are a "short" decay of 4.2 days and a "long" decay of 57.4 days. As for the ZnO, CuO, and Fe_2O_3, the decay studies were performed on 5 wt% metal oxide NPs supported on SiO_2. ZnO also shows two decay modes with 1/e liftetimes of [15] are 10 days and 70 days, while for CuO [17] and Fe_2O_3 [18], only one decay is found for each with 1/e lifetimes of 74 minutes and 3.8 days respectively. Dellinger et al. have shown that the lifetime of the formed EPFRs does not only depend on the type of TMO, but also on the type of the aromatic adsorbate [15]. They have also shown that the lifetime of the EPFRs formed on 5% ZnO/SiO_2 by the adsorption of several organic precursors are the longest-lived species observed [15].

In this study, the formation of EPFRs by high temperature adsorption of phenol on several transition metal oxide NPs, namely ZnO, CuO, Fe_2O_3, and TiO_2 is probed by several experimental

probes. The purpose is to elucidate characteristic vibrational and electronic fingerprints of the EPFRs formed by phenol adsorption on TMOs. EPFR detection and characterization require a combination of techniques; we performed electron paramagnetic resonance (EPR), Fourier transform infrared spectroscopy (FTIR), inelastic neutron scattering (INS), and X-ray photoelectron spectroscopy (XPS) of phenol adsorbed at 250°C on four different metal oxide NPs. The goal is to obtain a comprehensive database, including EPR, vibrational spectroscopy (INS and FTIR), and electronic spectroscopy (XPS) that enables one to identify the propensity of EPFRs formation on differing TMOs and the resulting property differences from each other and from other organic contaminants, as well as degradation pathways.

3.2. Experimental Methods

All metal oxide powders (anatase TiO_2, 18 nm, CAS 13463-67-7, 289 m^2/g, 99.5% purity; α-Fe_2O_3, 30 nm, CAS 1309-37-1,20-60 m^2/g, 99.5% purity; CuO, 25-55 nm, CAS 1317-38-0, 13.98 m^2/g, 99.95% purity; ZnO, 18 nm, CAS 1314-13-2, 40-70 m^2/g, 99.95% purity) were purchased from US Research Nanomaterials and used as-received. Phenol (CAS 108-95-2, ACS reagent grade, ≥ 99.0% pure) was purchased from Sigma-Aldrich and used without further purification.

Samples were prepared using the same dosing manifold described in previous work [12, 16], including a similar system assembled on-site at the Spallation Neutron Source [12]. “Blank” (un-dosed) TMO samples for all measurements were prepared in vacuum (~50 μTorr) by heating the samples to 250°C for 1 hour then cooling to RT. In this work, all dosed samples were prepared by loading a small quantity (200-600 mg) of TMO powder into a sample tube along with a small quantity (100-200 mg) of solid phenol. For INS measurements, at least 0.01 mol phenol (approximately 940 mg) was loaded into the tube along with several grams of powder; this ensured

that enough mass was present to give a strong signal from the relatively weak neutron scattering process. Samples were reacted by attaching the filled tube to the dosing system, pumping out to the turbomolecular pump base pressure (< 2 mPa), then closing the evacuated tube and heating it to 250°C for 1 hour. After exposure, the sample tube was again opened to the turbomolecular pump and pumped out at the dosing temperature for 1 hour, then pumped continuously while cooling to RT before removal from the dosing system for measurement. In this way, un-reacted phenol was removed from the tube before measurement so that no excess solid phenol was present in the measured samples, as evident by the lack of phenolic –OH mode in FTIR/INS spectra (see section 3.3).

Electron paramagnetic resonance (EPR) measurements were performed using Bruker EMXnano spectrometer with X-band, microwave power 100 mW, and microwave frequency of 9 GHz. The spectra were obtained at room temperature and the typical operating parameters were: microwave power of 0.3 mW, modulation amplitude 1 G, and time constant 40.96 ms.

Samples were analyzed under ambient conditions at RT using EPR spectroscopy and FTIR spectroscopy, and under high vacuum at 5K using INS at the VISION beamline [122] at the Spallation Neutron Source at Oak Ridge National Laboratory using the same methods as in our prior work [12]. All INS spectra were acquired with the samples continuously held under high vacuum, while FTIR spectra were acquired under ambient conditions no more than 10 minutes after opening the sample tubes to the atmosphere. To eliminate the possibility of EPFR photodegradation, samples that were used for the studies taking place after 18 days in ambient conditions were stored in a dark cabinet in a climate-controlled lab in containers allowed to exchange air with the room. In order to probe the EPFR decay, the aged samples were then analyzed using the same procedures as fresh ones.

XPS measurements were performed on metal oxide NP powders pressed to 1 cm diameter pellets. The core-level structure measurements were performed using monochromatic Al $K\alpha_I$ radiation ($h\nu$ = 1486.6 eV) from an Omicron XM1200 source. High resolution spectra were recorded using Omicron EA 128 hemispherical analyzer using 50 eV pass energy. An Omicron charge neutralizer system, CN 10, was only used for TiO_2 and ZnO samples. All samples, dosed and undosed, are charge-corrected to their respective O 1s binding energy values reported in Biesinger et al. [123, 124]. None of the pellets were cleaned by sputtering prior to XPS analysis, as this can reduce the surface of the metal oxide samples [123].

3.3. Results and Discussion

3.3.1 EPR studies of phenol adsorption on metal oxide NPs

EPR analysis of the dosed metal oxides reveals a narrow EPR signal superimposed on the broad metal ion signal. This narrow EPR signal is typical of organic radicals characteristic of EPFRs which are formed due to the electron transfer from the organic molecule to the surface of the metal oxide as proposed by the formation mechanism of EPFRs [15, 17-19]. It is noted that the undosed TMO powder shows no signal attributed to any organic radical species but only a broad paramagnetic signal of the metal ion. Therefore, the observation of this EPR signal is a clear indication of the EPFR formation due to dosing and subsequent chemisorption [16-19]. The type of EPFR formed strongly depends on the type of the adsorbate and the nature of the surface of the metal oxide [17]. Figure (3.1) depicts the first derivative EPR spectra for the different metal oxide NPs. The g-factor of the paramagnetic signal obtained for the different metal oxide ranges from 2.0032-2.0045 (cf. Table 3.1), which is a fingerprint of the formation of phenoxyl-type radical that is known to form upon phenol dosing. As seen from both table (3.1) and figure (3.1), TiO_2 has the narrowest paramagnetic signal (least peak width, $\Delta H_{p-p)}$ while Fe_2O_3 has the broadest paramagnetic

signal. Signal broadness can be attributed to the superposition of more than one type of paramagnetic species [16]. According to DFT calculations, the unpaired electron in the phenoxyl radical can be both oxygen-centered and carbon-centered [13]. Comparing the g-factors of the paramagnetic signal obtained for the different metal oxide NPs, one can see that the phenoxyl radical formed on the surface of ZnO is more oxygen-centered, while that formed on the surface of TiO_2, CuO, and Fe_2O_3 may be a combination of both oxygen- and carbon-centered phenoxyl radical.

Table 3.1 EPR spectral characteristics of the organic radical signal observed upon phenol dosing at 250 °C.

Metal oxide	g-factor	$\Delta H_{p\text{-}p}$ (G)	Spins/g
TiO_2	2.00345	5.0	2.05×10^{18}
CuO	2.00356	7.2	6.23×10^{16}
ZnO	2.00447	6.1	3.44×10^{16}
Fe_2O_3	2.00315	12.7	3.14×10^{15}

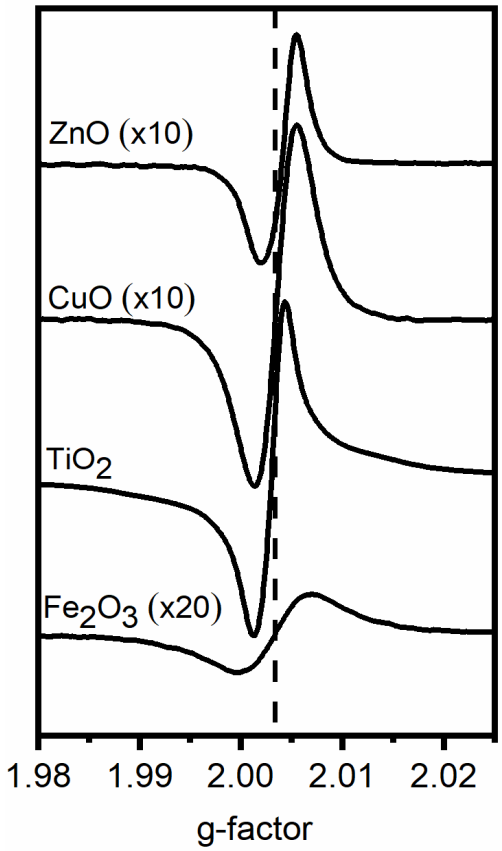

Figure 3.1. EPR spectra of metal oxide nanoparticles dosed for two hours with phenol at 250°C. Samples were allowed to react with phenol for 1 hr isolated from vacuum and an additional 1 hr in vacuum to ensure the removal of excess phenol in the dosed samples (see more details in Section 3.2).

The relation between EPFR concentration and the type of metal oxide has been previously studied [118, 125-127]. It has been found that the oxidation potential of the metal cation influences its catalytic ability toward forming EPFRs. Jia et al.[125] reported that Fe(III) has higher oxidation potential compared to Cu(II), Zn (II), Co (II), and Ni (II) in generating EPFRs from polycyclic aromatic hydrocarbon adsorbed on TMOs modified montmorillonite clay. Although high oxidation potential is expected to result in a larger concentration of EPFRs, the high catalytic activity of Fe (III) is found to decompose the formed EPFRs, which explains the low EPFR yield observed on Fe_2O_3 NPs [125]. On the other hand, the high radical yield observed in TiO_2 can be attributed to the presence of a large amount of superoxide species, which are reported to be

associated with metal oxide NPs [128, 129]. This can also explain the discoloration of TiO_2 nanopowder upon mixing with phenol at room temperature. Thus, the high EPFR yield on TiO_2 is a combined effect of the large surface area of the NPs and the superoxide species present which abstract hydrogen from the organic molecule and thus enable chemisorption of EPFRs on metal oxides surface [13, 118, 130].

3.3.2 Vibrational studies of phenol adsorption

The data presented in this section have been performed in collaboration with Dr. Matthew Patterson in the LSU Department of Chemistry. Figure (3.2) compares FTIR spectra for the different oxide powders dosed with phenol at 250°C, in the region between 1000-1800 cm^{-1}, as well as a reference spectrum of solid phenol. In order to remove the background features from the pure oxides, the FTIR spectra of the dosed powders are generated by subtracting the FTIR spectrum of the dosed powder with that of the undosed powders. In each case, the undosed powder was heated to the same temperature under vacuum and for the same amount of time, and the FTIR was obtained under the same conditions of the dosed oxide powders. By comparing the difference spectra of the different metal oxides to the phenol reference spectrum, one can see three main fingerprint features that accompany phenol chemisorption on the surface: the peak at 1593 cm^{-1} from solid phenol, which is attributed to pure C-C stretches in the ring, is observed in all dosed oxide powder spectra with a minor position shift and a drastic change in width, particularly, in CuO. The second feature is the collapse of the two peaks at 1470 and 1497 cm^{-1} to a single peak at around 1493 cm^{-1} for TiO_2, while the same feature results in a single peak at around 1489 cm^{-1} and a prominent shoulder at around 1446 cm^{-1} in ZnO, CuO, and Fe_2O_3. The two peaks at 1470 and 1497 cm^{-1} are attributed to a combination of $\nu(CC)+\nu(CO)$ and $\delta(CH)+\nu(CC)$ respectively in solid phenol. Finally, the third main feature is the broad band peaked at 1224 cm^{-1} in solid phenol

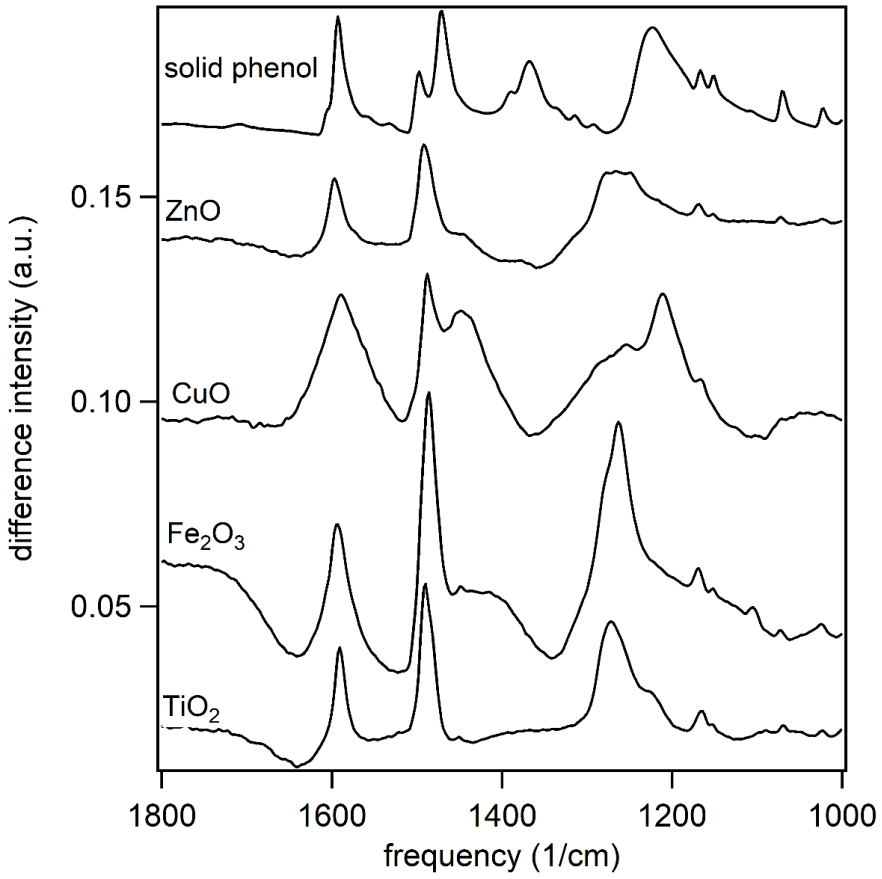

Figure 3.2. ATR-FTIR spectra of oxide powders dosed with phenol at 250°C. A spectrum of solid phenol is included for reference (topmost trace). Blank spectra (un-dosed powders heated to 250°C under vacuum for the same amount of time) have been subtracted from each dosed spectrum to remove background features from the pure oxides.

which is a manifold of δ(OH) and ν(CO) modes. This feature is observed in the spectra of all the dosed oxides in several positions that range between ~1275-1210 cm^{-1}, and in different widths as well, with Fe_2O_3 being the sharpest. These three features indicate the chemisorption of phenol on the surface of the different oxide powders, and hence the formation of phenol or phenoxyl-like surface species. Also, the absence of the broad manifold of hydrogen-bonded OH bending modes ~1380 cm^{-1}, observed in solid phenol, is indicative of a dissociated adsorption mechanism to the surface of the different oxide powders resulting in a chemisorbed phenoxyl-type surface species.

The major significant difference between the different FTIR spectra of the phenol dosed oxide powders lies in the intensity ratio of the two main C-C peaks (with Fe_2O_3 having the largest intensity ratio) as well as the intensity ratio of C-C to C-O.

The decay of the EPFRs formed on the surface of the different oxide powders has also been investigated using FTIR. Figure (3.3) depicts the FTIR spectra for the different oxide powders dosed with phenol at 250°C and stored for 18 days under ambient conditions. In general, the features characteristic of phenoxyl-like surface species are still present after 18 days in atmosphere at 300 K and ambient humidity. As seen from overlapping the FTIR spectrum obtained after 18 days on the top of the freshly dosed spectrum, the decay spectrum of TiO_2 shows a shift in the highest energy C-C peak at 1590 cm^{-1} toward higher frequency, as well as a shoulder at 1502 cm^{-1} that appears in the C-C stretch peak at 1490 cm^{-1} accompanied by a shift of the main peak from 1490 to 1485 cm^{-1}. Also, a small O-H in-plane peak at ~ 1380 cm^{-1} is also observed in the TiO_2 decay spectrum, along with a shift of the C-O region toward lower frequency associated with a redistribution of intensity. For Fe_2O_3, no position shifts or new peaks have been observed in the decay spectrum; however, there is an overall decrease in the intensity of the peaks observed as well as a broadening in the C-C peak at 1590 cm^{-1}. Similarly, an overall drop in the intensity of the peaks observed for the decay spectrum of CuO associated with some redistribution of the intensity between 1460-1360 cm^{-1}. Finally, the ZnO decay spectrum shows a large increase in the O-H in-plane bend peaked at 1355 cm^{-1} followed by slight changes in the C-O stretch region. Also, there is a decrease in the intensity ratio between the peak at 1492 cm^{-1} and the shoulder at ~1445 cm^{-1}.

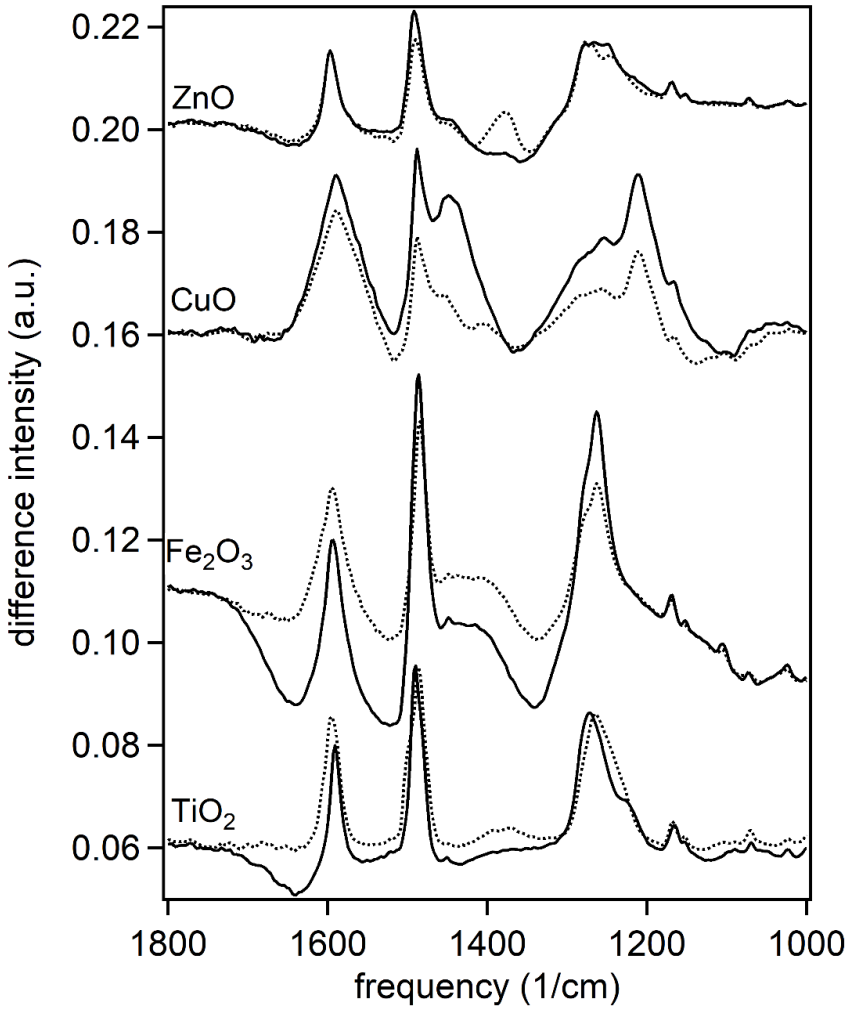

Figure 3.3. ATR-FTIR spectra of oxide powders dosed with phenol at 250°C (solid lines) compared with the same samples after storage under ambient conditions for 18 days (dotted lines). Blank spectra (un-dosed powders heated to 250°C under vacuum for the same amount of time) have been subtracted from each dosed spectrum to remove background features from the pure oxides.

Comparing the FTIR of the dosed metal oxides taken 18 days after dosing with the previously established phenoxyl-EPFR lifetimes, we can see that the appearance of the -OH in-plane bend at 1355 cm^{-1} and 1380 cm^{-1} observed in the FTIR decay spectra of ZnO and TiO_2, respectively. Furthermore, broadening in the C-C peak in Fe_2O_3 and decreased intensity of all peaks in both Fe_2O_3 and CuO are also observed. These features can be attributed to the decay of the phenoxyl radical into semiquinone products [16, 39]. This result is expected because the 18 days

time period between dosing and measurement is longer than the reported lifetime of the EPFRs formed on 5% Fe_2O_3/SiO_2, Fe(III)-exchanged clays, and 5% CuO/SiO_2, and thus some degree of degradation is expected. In ambient environment, molecular oxygen in the atmosphere, as well as adsorbed water, catalyze the photodegradation of EPFRs to molecular species [131, 132]. However, EPFRs can persist indefinitely in vacuum [17-19].

INS can more effectively probe lower energy excitations and access modes that are less IR active. Figure (3.4a) shows the out-of-plane bending motion of the phenyl ring at ~410 cm^{-1} for solid phenol as well as for oxide powders dosed at 250°C. The observation of this mode in the dosed oxide powders is a fingerprint of the chemisorption of phenol and the formation of phenoxyl-type adsorbed species on TMO powders. The peak widths are reminiscent of the ring stretching modes in IR, in that all oxide powders except CuO are close to each other and to the reference spectrum; however, the peak widths in CuO are considerably broader. Figure (3.4b) depicts the C-H in-plane bend at ~1160 cm^{-1}, which is the most intense C-H mode measured by INS. The C-H stretch peak positions for the different oxide powders are again comparable to those seen for the reference spectrum suggesting an intact phenyl ring [133].

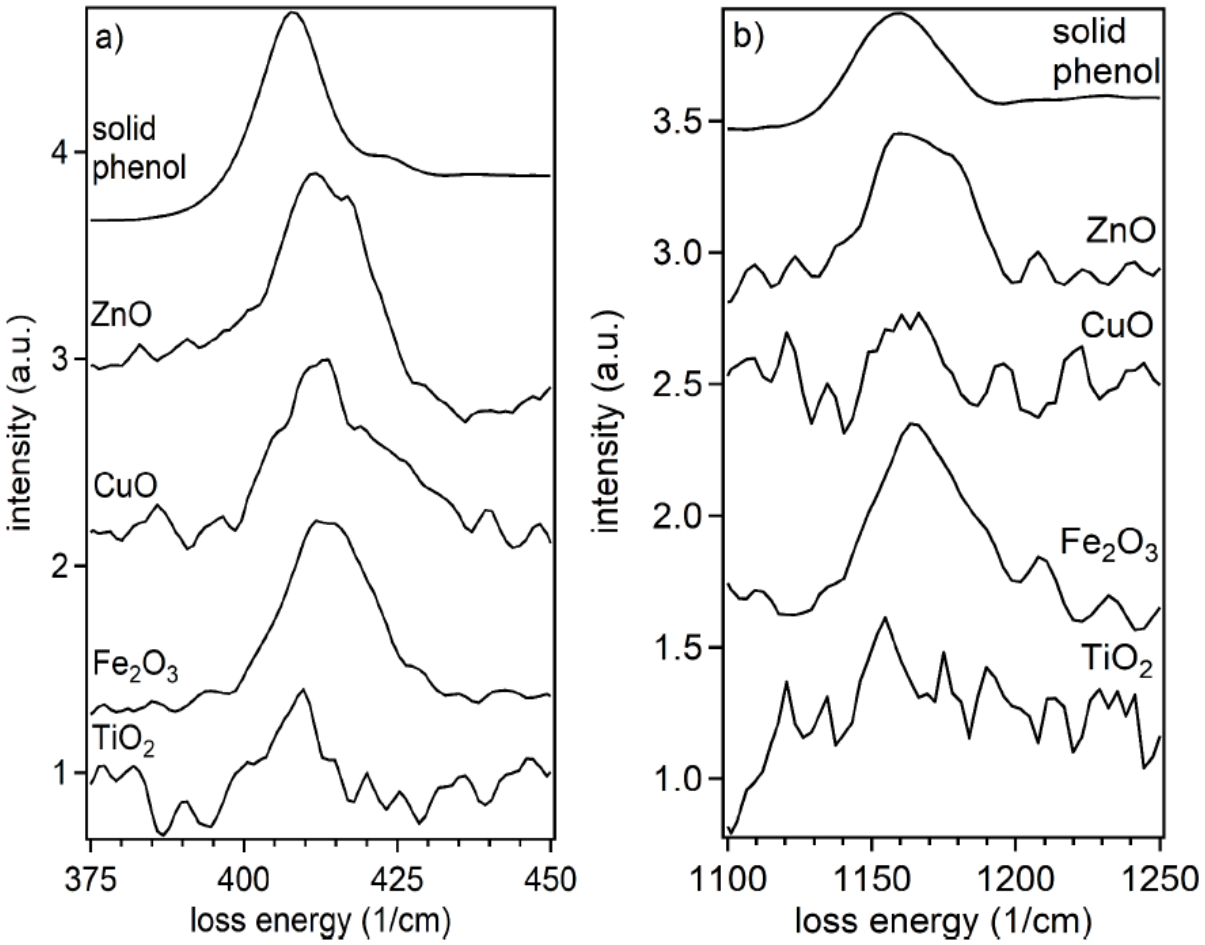

Figure 3.4. Inelastic neutron scattering spectra of oxide powders dosed with phenol at 250°C along with solid phenol reference spectrum (topmost trace). Blank (un-dosed) spectra of powders inside the appropriate sample containers have been subtracted from each of the spectra from the oxides. Figure (a) shows the region containing ring out-of-plane bending motion, (b) shows a C-H in-plane stretch.

3.3.3 Structural changes due to EPFRs formation

The conventional mechanism of EPFR formation proposes that the formation of each organic free radical is accompanied by the reduction of a surface metal cation. That is, one surface metal cation is involved per one phenol chemisorption process resulting in electron transfer to the metal cation that consequently lowers its oxidation state by 1. This aspect of EPFR formation is further investigated by using XPS which is employed to study the chemical states of the metal cations prior to and after dosing. Figure (3.5a) shows the Ti 2p region for the dosed and undosed

TiO_2 NPs pellet surface. The spectrum of the undosed pellet is characteristic of the Ti 2p region of TiO_2, in which the chemical state of titanium is Ti $^{4+}$ with the Ti $2p_{3/2}$ binding energy at 458.9 eV. The features observed at 472 eV and 477.6 eV are loss features due to inelastic scattering of the X-ray photoelectrons [134]. Upon dosing with phenol, a shoulder at 457.3 eV appears on the Ti $2p_{3/2}$ peak of the dosed spectrum along with a broadening of the Ti $2p_{1/2}$ peak. This observation indicates that Ti $^{4+}$ states are partially reduced to Ti $^{3+}$ due to phenol chemisorption.

This result indicates that phenol chemisorbs to the surface of TiO_2 by a single electron transfer from the organic molecule to the surface, causing the metal oxide surface to be partially reduced. This adsorption mechanism agrees well with the proposed EPFR formation mechanism.

A similar result has been observed for CuO. Figure (3.5b) shows the Cu 2p region for both dosed and undosed CuO NPs pellets. The shake-up satellite characteristic of Cu $^{2+}$ states is seen for both dosed and undosed surfaces. Upon phenol chemisorption at high temperature, a sharp peak at 932.6 eV is observed in the Cu $2p_{3/2}$ peak followed by a broadening of the Cu $2p_{1/2}$ peak of the dosed spectrum. Again, this result is characteristic of the partial reduction of Cu $^{2+}$ to Cu $^{1+}$ and the coexistence of both chemical states on the surface. This result is consistent with the Cu K-edge XANES spectroscopy of micron-sized CuO/silica dosed by three different organic precursors which has shown the reduction of CuO to a mixture of Cu $^{2+}$, Cu $^{1+}$ and Cu (0) due to high temperature dosing [115].

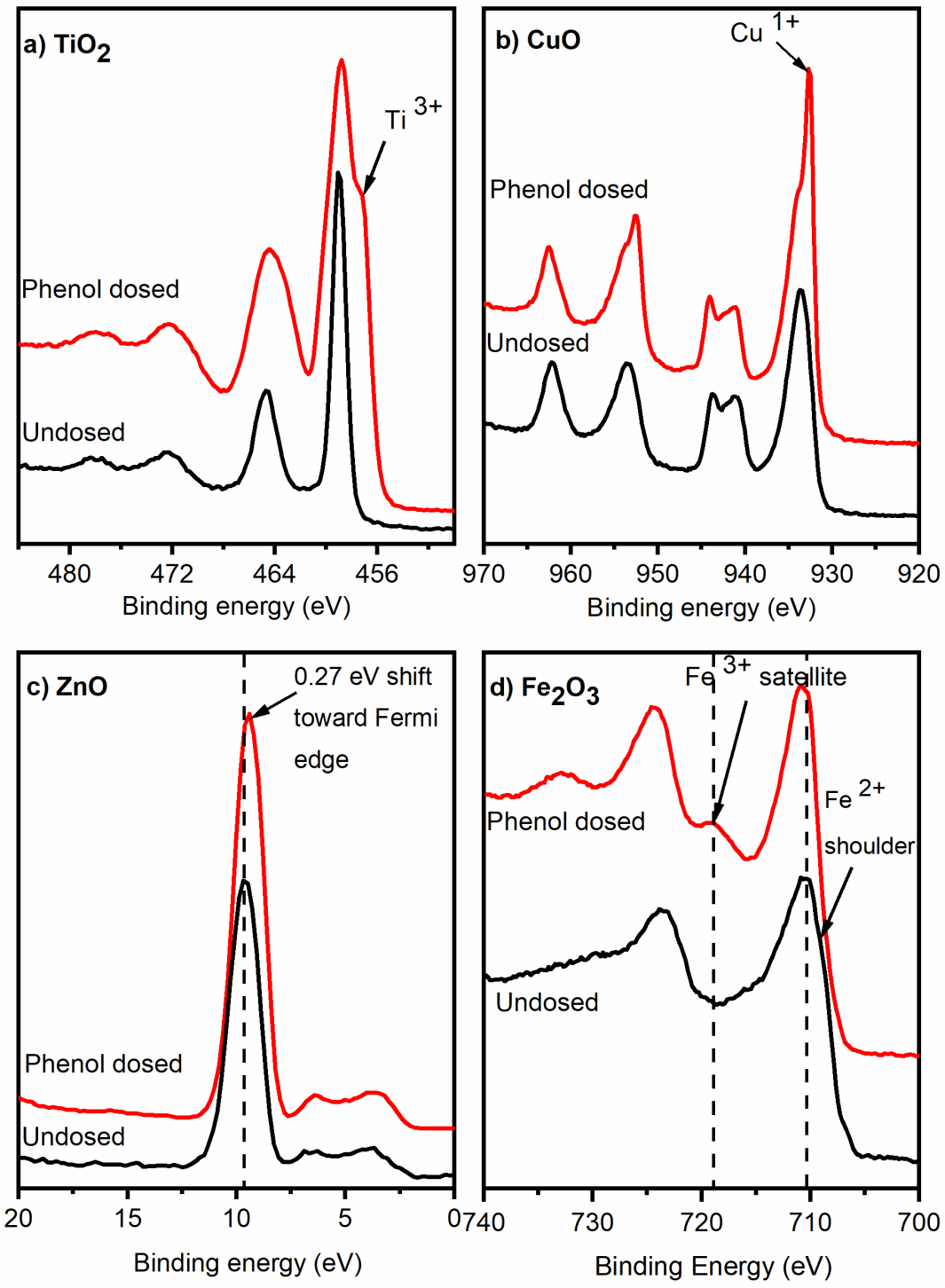

Figure 3.5. X-ray photoelectron spectra of metal oxide pellets dosed with phenol at 250°C (red) and undosed (black). Figure (a) shows Ti 2p region of TiO_2 pellet, (b) Cu 2p region of CuO pellet, (c) Zn 3d region of ZnO pellet, and (d) Fe 2p region of Fe_2O_3 pellet.

As a check for consistency, the chemical state of the phenol dosed CuO NPs can also be determined by calculating the modified Auger parameter (α), which is defined as:

$$\alpha = E_k(C_1C_2C_3) + E_B(C)$$

where $E_k(C_1C_2C_3)$ is the kinetic energy of the Auger transition $C_1C_2C_3$ and $E_B(C)$ is the binding energy of an electron from core level *C*. For CuO, the Auger transition Cu LMM at around 918 eV, see figure (3.6), and the Cu $2p_{3/2}$ core level peak are considered. The modified Auger parameters for both undosed and phenol dosed CuO were calculated and were found to be 1851.49 ± 0.017 eV and 1849.84 ± 0.012 eV, respectively. The value for the undosed CuO is consistent with the previously reported value for clean CuO, but the value for the dosed CuO lies between the reported values for CuO and Cu_2O [123]. This again implies that dosing with phenol causes the partial reduction of the CuO from almost entirely Cu^{2+} to a mixture of Cu oxidation states.

Table 3.2. Binding energy of 2p3/2 core-level of CuO and ZnO as well as kinetic energy of Cu LMM and Zn LMM.

	Cu $2p_{3/2}$ (eV)	**Cu LMM (eV)**	**Zn $2p_{3/2}$ (eV)**	**Zn LMM (eV)**
Undosed surface	933.77 ± 0.0046	917.72 ± 0.016	1021.01 ± 0.0007	989.04 ± 0.007
Dosed surface	932.35 ± 0.0017	917.49 ± 0.012	1020.4 ± 0.0009	988.9 ± 0.006

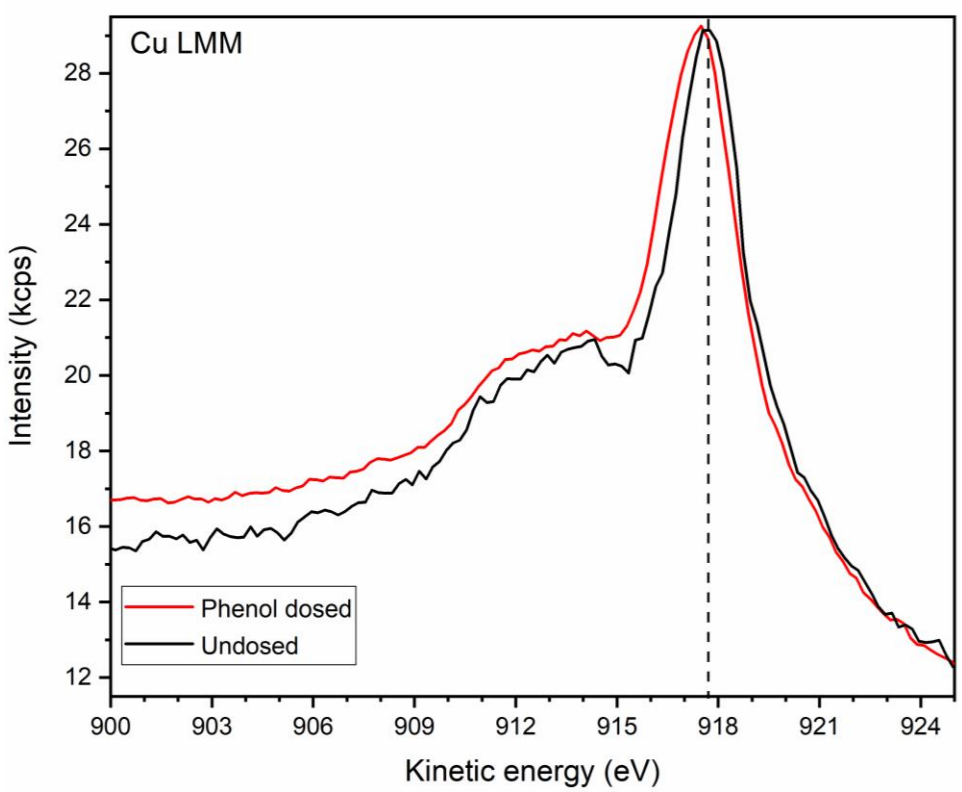

Figure 3.6. X-ray photoemission spectrum of Cu LMM transition of undosed (black) and phenol dosed at 250ºC (red) of CuO nanoparticle pellet

Figure (3.5c) shows the Zn 3d region of undosed and phenol dosed at 250 ºC ZnO NPs pressed to a pellet. The photoemission peak at 9.7 eV is attributed to Zn 3d. The remaining intensity between 3.6 and 6.8 eV is due to the O 2p and the Zn 4s electrons, respectively. Upon dosing ZnO NPs with phenol, the spectrum is found to shift by 0.27 eV toward the Fermi edge. This band bending is consistent with electron transfer from ZnO and has been previously reported for phenol dosed ZnO (1010) and ZnO (0001)-Zn single crystal surfaces [121]. Just as we have shown for the CuO, we can also infer chemical state information of the ZnO after dosing by calculating the modified Auger parameter. For ZnO, the Zn LMM Auger transition at around 988 eV and the Zn $2p_{3/2}$ peak are considered, see figure (3.7) and table (3.2). The modified Auger parameters for both undosed and phenol dosed ZnO were calculated and were found to be 2010.05 ± 0.007 eV and

2009.3 ± 0.006 eV, respectively. The value for the undosed ZnO is consistent with the previously reported value for clean ZnO [123]. The decrease in the modified Auger parameter due to dosing is consistent with the increase of the oxidation state of the Zn(II) cations [135], and that again confirms electron transfer from the ZnO as seen by the band bending in the Zn 3d dosed spectrum.

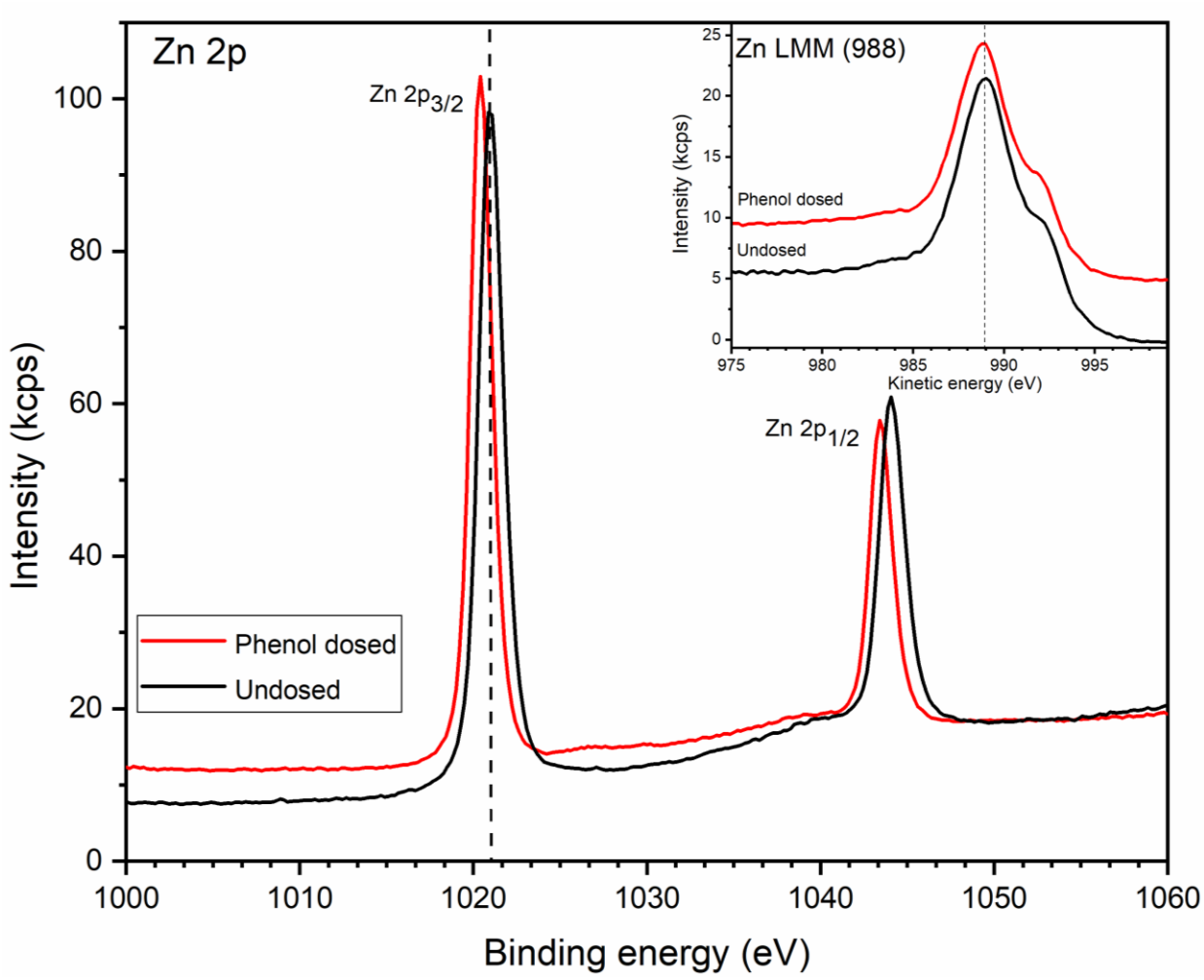

Figure 3.7. Zn 2p core level spectrum for undosed and phenol dosed ZnO. Figure inset shows the Zn LMM transition for dosed and undosed samples.

Figure (3.5d) shows Fe 2p core level spectra of phenol dosed and undosed Fe_2O_3 NPs. By looking at the undosed spectrum, the shake-up satellite at ~ 719.3 eV characteristic of Fe_2O_3 is absent. On the other hand, there is a satellite at 715.6 eV characteristic of Fe^{2+} along with a small shoulder ~706 eV. This suggests that the surface of the pellet prior to dosing is reduced to a mixture of Fe_2O_3 and Fe_3O_4. This reduction arises mainly from the mechanical pressure applied to the iron oxide powder to form a pellet. Upon dosing the reduced surface of Fe_2O_3 pellet with phenol at 250 ºC, the shake-up satellite characteristic of Fe_2O_3 is now observed associated with a shift toward higher binding energy. This result suggests that phenol is chemisorbed on the surface of the NP pellet through electron transfer from the iron oxide nanopowder, causing oxidation of the Fe cations as seen by XPS.

By looking at the overall picture given by XPS, we see that surface metal cations of TiO_2 and CuO are reduced due to phenol chemisorption indicating electron transfer from the organic molecule to the metal oxide surface, which is consistent with the typical EPFR formation mechanism. On the other hand, surface metal cations of ZnO and reduced-Fe_2O_3 surface are found to oxidize by phenol chemisorption, which contradicts this EPFR formation mechanism. However, EPR results show that in both cases EPFRs are formed. The direction of electron transfer proposed in the EPFRs formation mechanism is based on Lewis acid-base theory, in which metal cations are acids that accept electrons while the organic precursors are bases that donate electrons. However, adsorption behavior depends on surface properties. D'Arienzo et al. reported that the intrinsic defects in ZnO NPs can act as oxidative sites for the organic molecule and thus can promote the formation of EPFRs on the surface of the metal oxide NPs [136]. Therefore, we can infer that the defects which exist intrinsically in ZnO, and are induced in the reduced surface of Fe_2O_3 pellet, are the catalytically active sites for phenoxyl formation. Also, our group, based on synchrotron-

based photoemission and electron-energy-loss spectroscopy, has previously shown that the oxidation of ZnO to a higher oxidation state is precluded because Zn(III) does not exist in nature, that is oxidizing Zn(II) to Zn(III) is not observed [12]. Our DFT calculations, in this case, have shown that the higher oxidation state of Zn(II) is obtained by a partial electron transfer (-0.86*e*) to the organic molecule from three coordinated surface Zn atoms [12]. Furthermore, our photoemission results confirm the increase of the oxidation state of both ZnO NPs (partially) and reduced-Fe_2O_3 NPs (by one). Hence, we are certain that there is a partial/electron transfer to ZnO and reduced-Fe_2O_3 cations. However, the exact mechanism of phenol oxidation by chemisorption to surface defects is yet unclear and requires further investigations to be clearly understood.

3.4. Conclusion

We have studied the vibrational structure, the change in the chemical state, and the nature of the radical species formed on the surface of ZnO, CuO, Fe_2O_3, and TiO_2 nanoparticles due to phenol adsorption at high temperature. A number of key, fingerprint characteristics of EPFRs formed on TMOs due to phenol adsorption have emerged. EPR has shown a paramagnetic signal characteristic of phenoxyl radical whose yield is dependent on the type of metal oxide, as the spin density is highest in TiO_2 and lowest in Fe_2O_3. It has also shown that the broadness in the paramagnetic signal can be due to the superposition of oxygen- and carbon-centered phenoxyl radicals. FTIR has shown three main features that demonstrate the chemisorption of phenol on the surface of the different metal oxides due to phenol dosing. It has shown the absence of –OH contribution which implies the dissociated adsorption of phenol on the surface of metal oxides forming phenoxyl-metal surface species. FTIR spectra taken 18 days after dosing have shown different characteristics for the different metal oxides and indicate that the decay mechanism of the formed radical depends on the surface of the metal oxide and is not solely determined by

reactions with gas-phase molecules. INS spectra have further confirmed the chemisorption of phenoxyl-species by showing both ring out-of-plane bend motion and C-H in-plane bend motion. Finally, utilizing XPS has enabled us to study the change of the chemical state of the metal cations due to phenol chemisorption. The surface of TiO_2 and CuO pellets were found to be partially reduced, whereas Fe_2O_3 and ZnO pellets were observed to oxidize upon phenol chemisorption. These results have shown that the direction of the electron transfer in EPFR formation is strongly determined by the nature of the reacting metal oxide surface rather than Lewis acid-base theory. Future studies should account for the role of surface defects in the adsorption behavior of organic precursor on the surface of TMOs and consequently EPFRs formation.

Chapter 4. Photoemission Studies of Phenol Adsorption on α–Fe_2O_3 (0001)

4.1. Introduction

Environmentally persistent free radicals (EPFRs) are long-lived surface bound radicals that are formed by the chemisorption of aromatic hydrocarbons to the surface of transition metal oxides [14]. The lifetime of EPFRs can range from hours to days under ambient conditions [17, 18]. Their long lifetime has been attributed to their low reactivity with O_2, which makes EPFRs resistant to decomposition in the ambient environment [14, 137]. The basic formation mechanism of EPFRs involves initially the physisorption of an organic precursor to the surface of a transition metal oxide, followed by elimination of H_2O or HCl, depending on the type of the organic precursor, and finally chemisorption to the metal oxide surface [17]. During chemisorption, electron charge is transferred from the organic precursor to the metal oxide, thus reducing the metal cation and forming the EPFRs [17]. EPFRs pose adverse health impacts to humans [1, 3, 56, 74, 75, 112, 138, 139]. They are found to be associated with toxic airborne particulate matter (PM) which mostly result from combustion systems [14]. Upon inhalation, EPFRs produce reactive oxygen species (ROS), which causes oxidative stress that is responsible for respiratory and cardiovascular diseases [1, 14, 75]. Therefore, obtaining a fundamental understanding of the EPFRs formation mechanism is significantly important in understanding their environmental toxicity and in leading strategies for their prevention.

The formation of EPFRs from substituted benzene precursors on metal oxides supported on silica used as model fly ash have been extensively studied with electron paramagnetic resonance (EPR) [18, 19, 50, 140]. It has been reported that EPFRs are thermally activated, and either a phenoxyl-type or semiquinone-type radicals are formed [18]. Also, the correlation between transition metals

concentration in soil samples and EPFRs generation has been explored [125, 131, 141-143]. EPFRs have been found to form more readily on anthracene contaminated Fe(III)-montmorillonite [141].

Iron oxides are typically used as heterogeneous catalysts in many environmental and industrial processes [144]. It has been found that Fe (III) is the most abundant transition metal in airborne $PM_{2.5}$ since it comprises 10-70% of the bulk iron content in urban atmosphere[18]. Yang et al. have reported that Fe(III) in Fe_2O_3 exhibit a higher oxidation potential compared to ZnO, CuO, and NiO [118]. However, the high catalytic ability of Fe_2O_3 leads to lower yield of EPFRs [19]. This observation has been attributed to the partial decay of the generated EPFRs due to the high reactivity of Fe(III) [125].

Our group have utilized surface science techniques to elucidate the electronic and vibrational properties of the EPFRs formed on the TiO_2 (110), ZnO ($10\bar{1}0$) and ($000\bar{1}$) single crystal surfaces at room temperature as well as elevated temperature [120, 121]. Patterson et al. have shown a clear evidence of electron charge transfer from phenol HOMO to the unfilled states of TiO_2, this result is further confirmed by the downward band bending observed in the Ti 3p core level spectrum obtained for dosed TiO_2 at high temperature [120]. Band bending occurs due to the electric field induced by the electron charge transfer between the adsorbate and the surface, therefore, valence band shifts upward or downward depending on the direction of the electron charge transfer [145]. In contrast to Ti, Thibodaux et al. have shown an upward band bending in ZnO 3d states [121]. DFT calculations attributed this result to the chemisorption of the phenoxyl group through its oxygen atom, which coordinates to three Zn atoms on the surface [12]. Accordingly, partial electron transfers to Zn metal cations [121].

In this study, we perform ultraviolet photoelectron spectroscopy (UPS) and X-ray photoelectron spectroscopy (XPS) on phenol adsorbed at room temperature and at 250 °C on the

α–Fe_2O_3 (0001) single crystal surface to understand the electronic structure change and elucidate the electron transfer mechanism as a function of adsorption temperature. This surface science approach enables us to study the atomic-scale formation of EPFRs on α–Fe_2O_3 (0001) single-crystal surface, as well as to develop an atomic-scale understanding of the electronic structure of the composite organic/metal oxide system.

4.2. Experimental Methods

All photoemission experiments were performed in an ultra-high vacuum (UHV) system with base pressure below 2×10^{-10} Torr. The photoemission spectra were obtained at room temperature using an Omicron XM1000 monochromatic X-ray source (Al $K\alpha_I$) and SPECS microwave UV light source (utilizes He II line ~40.8 eV) in combination with a SPECS PHOIBOS 150 hemispherical analyzer. No charge neutralizer was applied and the sample was properly grounded. All XPS spectra were obtained at 25 eV pass energy, while UPS spectra were acquired at 10 eV pass energy. The Fermi edge is determined from a gold foil in electrical contact with the sample and all XPS spectra are referenced to Au $4f_{7/2}$ peak at 83.95 eV. XPS spectra were analyzed using CasaXPS. C 1s and O 1s peaks were fitted with a lineshape blend of Gaussian (Y%)-Lorentzian (X%) defined in CasaXPS as GL(X), peaks are fit better with GL(30) lineshape.

A single crystal sample of α–Fe_2O_3 was purchased from SurfaceNet GmbH (Germany). The sample was cut along the (0001) surface with (10 mm × 10 mm × 0.5 mm) dimensions, with one side polished. A stoichiometric (0001) surface was prepared in UHV chamber by cycles of 500 eV Ne ion bombardment at 5×10^{-5} Torr for 20 min followed by 30 min annealing at 700 °C in 1×10^{-6} Torr O_2, and subsequently cooled in O_2 atmosphere . The sample temperature was monitored by a type K thermocouple in contact with the plate beneath the sample. The surface cleanliness before dosing was checked by XPS and was found not to exhibit any C 1s peak on the

clean surface. Also, the binding energy of O 1s of the clean surface is consistent with the previously reported value. Dosing of phenol was accomplished by introducing phenol vapor into the UHV chamber using a standard leak valve. The phenol was purified by several freeze-pump-thaw cycles. For high temperature dosing, the sample was brought to 250 °C and dosed with phenol at 5×10^{-7} Torr.

4.3. Results and Discussion

Figure (4.1a) shows the UPS spectra of the α–Fe_2O_3 (0001) surface dosed with phenol at room temperature and 250 °C. A Tougaard background is subtracted from the spectrum of the clean surface, whereas a combination of Tougaard and Shirley backgrounds are subtracted from each spectrum of the surface dosed at different conditions. In the spectrum acquired from the clean α–Fe_2O_3 (0001) surface, the photoelectron emissions observed from 4 eV to 7 eV are mainly due to O 2p states hybridized with the Fe 3d states while the shoulder at 2.5 eV is due to Fe^{3+} states [146]. Upon exposure to 400 Langmuirs (L) at room temperature, structures with significant intensities appear in the region from 5.7 to 16 eV. The 400L high temperature dose show a clear feature at 0.85 eV, which seems to overlap with another feature at the 800 L dose. Similar to the room temperature dosed spectrum, phenolic features are observed in the region from 6 to 16 eV in the high temperature doses. The difference spectra in figure (4.1b) for the surface dosed at different conditions highlights the adsorbate feature relative to the clean surface. Thus, at 400L room temperature dose, the feature at 0.3 eV which is attributed to defective sites is diminished in the difference spectrum. For the dosed surface, it is well known that the intensity of the photoelectron emissions from the substrate is attenuated due to adsorbates on the surface. Therefore, the difference spectra were generated by scaling down the intensity of the clean spectrum by 0.65 before subtraction.

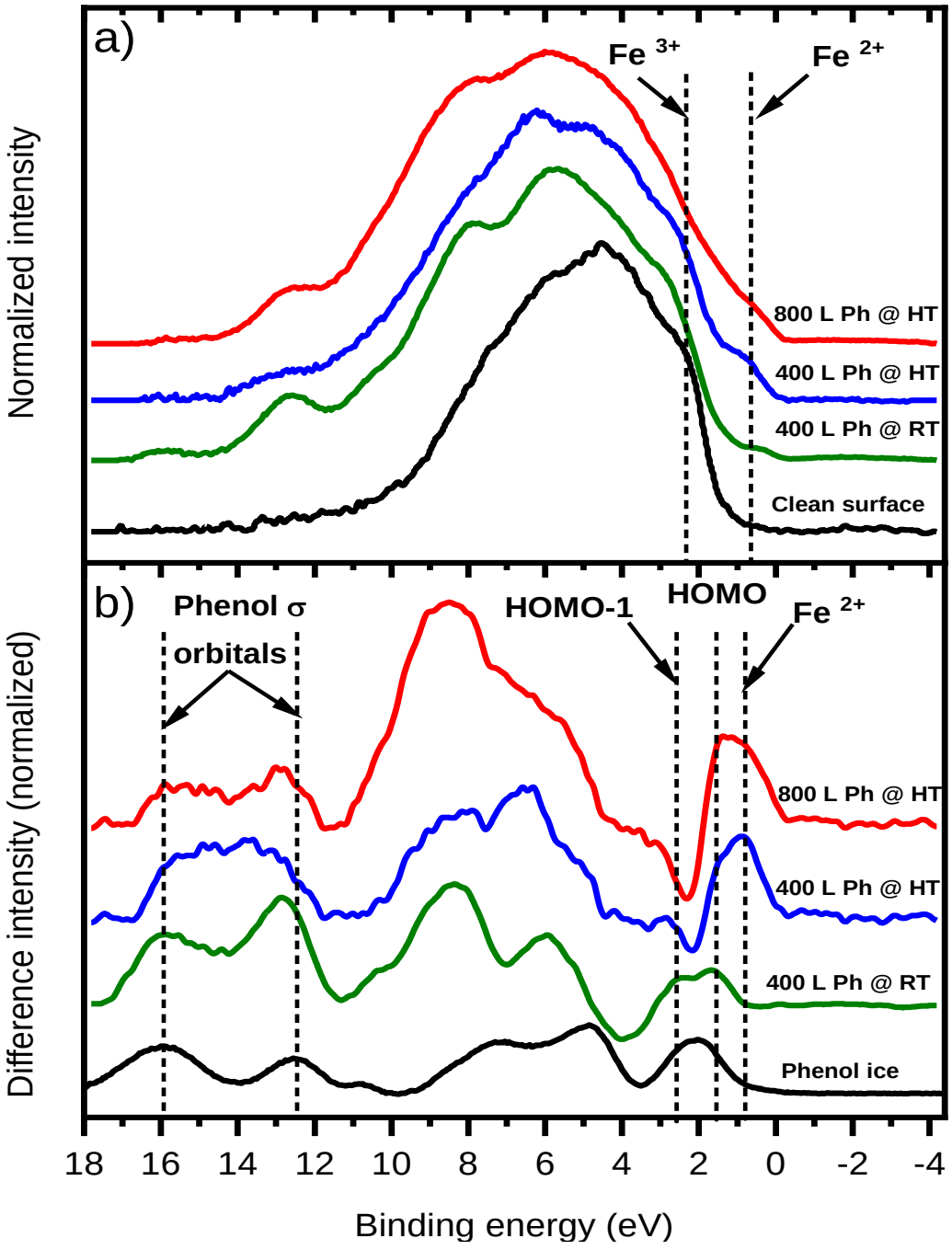

Figure 4.1 (a) UPS spectra of clean α–Fe_2O_3 (black), 400 L of phenol dosed at room temperature (green), 400 L of phenol dosed at 250 °C (blue), 800 L dosed at 250 °C (red). (b) Difference spectra obtained from data in (a), plotted with the spectrum of multilayer physisorbed phenol on the sample at -173 °C (black).

Figure (4.1b) shows the difference spectra of the dosed surfaces at different dosing conditions along with the "phenol ice" spectrum (thick condensed layer), which is obtained by cooling down the sample with liquid nitrogen to -173 °C and then dosing with phenol at this temperature until no Fe_2O_3 features are observed in the UPS spectrum. For the room temperature dose, the two peaks at 1.6 eV and 2.6 eV can be assigned to phenol HOMO and HOMO-1 bands, respectively. The 1 eV energy difference between the two phenolic bands is consistent with the results reported for phenol/ZnO ($10\bar{1}0$) (HOMO and HOMO-1 were observed at 2.5 eV and 3.5 eV, respectively) [121]. The emission at 5.9 eV and 8.3 eV are mainly due to the electronic levels of the oxygen in the phenyl ring while the feature at 10.3 eV can be attributed to $\sigma_{O\text{-}H}$ orbital [147]. The distinct intensities at 12.8 eV and 16 eV are similar to peaks observed for phenol/TiO_2 though 1 eV lower in binding energy. In comparison with the phenol ice spectrum, these two peaks can be assigned to the phenol σ–orbitals.

The high temperature doses show an intense peak at 0.9 eV that is neither observed for the room temperature dose nor in the phenol ice spectrum, this feature is clearly not phenolic. By referring to the UPS spectra obtained for the different iron oxides [146, 148], this feature can be assigned to Fe^{2+} states which are formed due to phenol dosing at high temperature. This peak is followed by a shoulder at 1.4 eV for the 400 L phenol, which becomes more distinct and intense at 800 L phenol. Again, this feature can be assigned to the phenol HOMO band, which seems to become more populated at 800 L phenol. On the other hand, the peak assigned to the phenol HOMO-1 band in the room temperature dose appears to be depopulated and shifted toward higher binding energy. Furthermore, the two features attributed to the electronic levels of the oxygen in the phenyl ring are modified in terms of position and intensity in the high temperature coverages. Also, the feature assigned to $\sigma_{O\text{-}H}$ orbital is clearly diminished in the 400 L dose at high

temperature. Yet, for the 800 L exposure, the intense emission at 8.3 eV makes it difficult to verify the existence of this feature. Finally, the phenol sigma orbitals are observed for the two high temperature doses. However, they appear to be broader and less intense (specially for 400 L phenol) with respect to the room temperature spectrum.

XPS is a very helpful surface-sensitive tool to study the elemental composition of the surface. Figure (4.2) shows the XPS spectra of the Fe 2p region of the clean and the phenol dosed surfaces at different conditions. The motivation here is to probe changes in the oxidation state of iron cations. For iron oxide, Fe^{3+} oxidation state is characterized by a satellite peak at 719.3 eV, which is clearly observed in the Fe 2p clean spectrum in Fig. 2, and the binding energy of Fe $2p_{3/2}$ is observed at 710.9 eV. Upon dosing at room temperature, there is almost no alteration in the satellite peak intensity, indicating that the surface mostly contains Fe^{3+} cations. However, at the elevated temperature doses, the intensity of the Fe^{3+} satellite is significantly reduced for the 400 L phenol dose, while it is diminished further for the 800 L phenol with a clear increase in the area ~715 eV which is the binding energy characteristic of Fe^{2+} satellite. For both high temperature doses, the FWHM of Fe $2p_{3/2}$ photoelectron peak become broader indicating the coexistence of both Fe^{2+} and Fe^{3+} oxidation states. This broadness is accompanied by a structure at 708.7 eV ascribed to Fe^{2+} states, observed in both of the high temperature doses which becomes more intense in 800 L phenol dose. Also, the binding energy separation between Fe $2p_{1/2}$ and Fe $2p_{3/2}$ is decreased.

It is anticipated that O 1s and C1s core level spectra will provide more insight information on the adsorbate structure. Figure (4.3) shows O 1s spectra of the clean as well as the dosed surfaces of α–Fe_2O_3 (0001). The main observation in this figure is the shift of O 1s toward higher

binding energies in the high temperature doses, with a maximum of 0.3 eV for the 800 L at 250 °C.

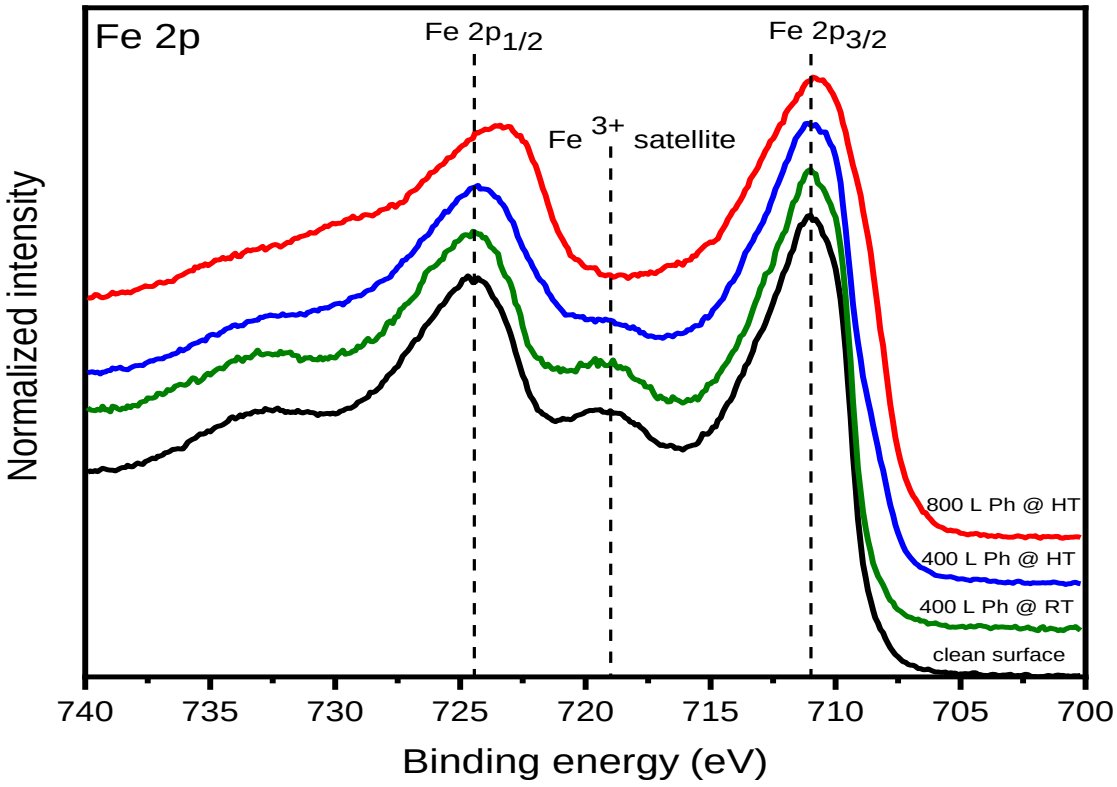

Figure 4.2. XPS spectra of Fe 2p core levels in clean surface of α–Fe_2O_3 (black), 400 L of phenol dosed at room temperature (green), 400 L of phenol dosed at 250 °C (blue), and 800 L of phenol dosed at 250 °C (red).

Also, the full width at half maximum (FWHM) increases at elevated temperature doses due to an emerging structure at the higher binding energy side of the O 1s peak. Therefore, we have quantitatively fit O 1s spectra of the 400 L at room temperature and 800 L at high temperature to identify the features evolving due to phenol adsorption at both temperatures. Figure (4.4) shows O 1s XPS spectra of the phenol dosed α–Fe_2O_3 (0001) surface at 400 L at room temperature (bottom panel), and 800 L at 250 °C (top panel). The O 1s region of the room temperature dose is deconvoluted into three components. The main component at 530 eV is due to lattice oxygen; the

second component at 531.12 eV is assigned to surface hydroxyl (OH) species. For the best fit results, a third component is added to the fitting at 532.25 eV and can be assigned to water or phenolic oxygen. All three components are constrained to have the same FWHM. Upon dosing 800 L phenol at 250 °C, we observe a broader O 1s peak. The envelope is again deconvoluted into three components. The lattice oxygen component is shifted 0.3 eV toward higher binding energy. A paramount increase in intensity is observed in the surface hydroxyl species component along with 0.32 eV shift toward higher binding energy. The third component is now observed at 533.11 eV and is broader and more intense. This component cannot be assigned to water, since the sample is here dosed at 250 °C. Therefore, it has to be due to phenolic oxygen.

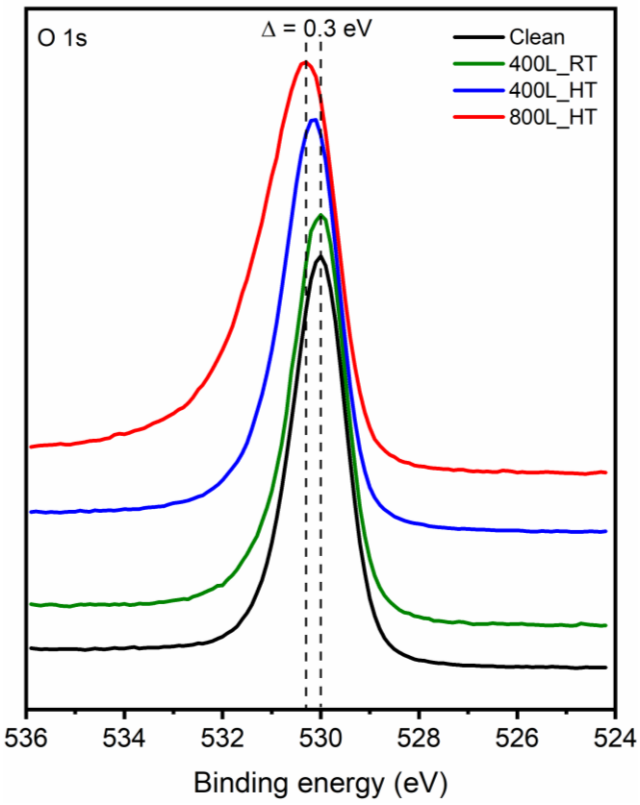

Figure 4.3. XPS spectra of O 1s core levels in clean surface of α–Fe_2O_3 (black), 400 L of phenol dosed at room temperature (green), 400 L of phenol dosed at 250 °C (blue), and 800 L of phenol dosed at 250 °C (red).

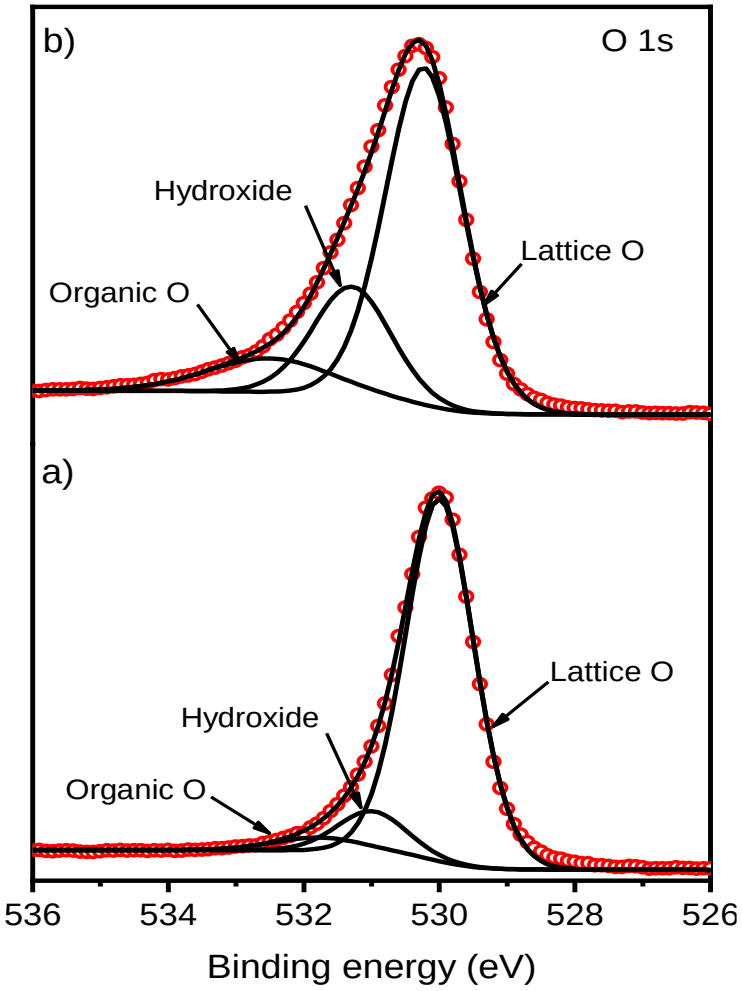

Figure 4.4. XPS spectra of O 1s core levels in (a) 400 L of phenol dosed at room temperature, (b) 800 L of phenol dosed at 250 °C.

Figure (4.5) shows C 1s XPS spectra of the phenol dosed α–Fe_2O_3 (0001) surface at 400 L at room temperature (bottom panel), and 800 L at 250 °C (top panel). For the room temperature dose, the main peak was fitted by one component at 284.0 eV which is ascribed to the unsubstituted carbons on the phenyl ring (C-C), and a shoulder at 285.4 eV ascribed to (C-OH) [123]. A broader peak is also observed at 290.9 eV and is attributed to the $\pi - \pi^*$ shakeup satellite, which is characteristic of an aromatic ring on the surface [149]. For the high temperature dose, the two components of the main photoelectron peak are shifted 0.4 eV toward higher binding energy. Moreover, the (C-O) component is significantly increased in intensity and overlapped with the

main (C-C) component. On the other hand, the $\pi - \pi^*$ shakeup satellite is shifted 0.64 eV toward higher binding energy and the best fit result requires the fourth peak at 287.8 eV, which can tentatively be assigned to (C=O).

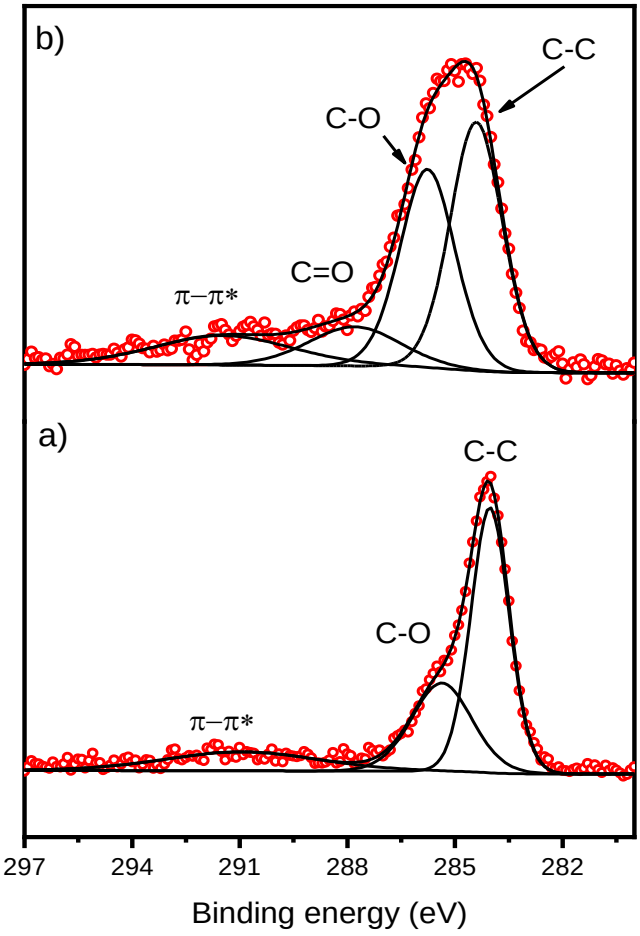

Figure 4.5. XPS spectra of C 1s core levels in (a) 400 L of phenol dosed at room temperature, (b) 800 L of phenol dosed at 250 °C.

The surface atomic structure of α–Fe_2O_3 (0001) surface is examined by LEED. This surface has been described as "the most challenging among the iron oxides" because cleaning cycles of sputtering and annealing produce reduced terminations [150-153]. "α–Fe_2O_3 crystallizes in the corundum structure with a hexagonal unit cell, in which O anions form a close packed hcp sublattice with ABAB stacking along [0001] direction. The Fe^{3+} cations are arranged in a honeycomb $\left(\sqrt{3} \times \sqrt{3}\right)R30°$ like layers", see figure (4.6b) [154]. Figure (4.6c) shows LEED pattern of α–Fe_2O_3 (0001) surface obtained after several cleaning cycles of sputtering and annealing subsequent to a several phenol doses at high and room temperatures. This pattern has been previously reported to correspond to Fe_3O_4 (111) surface with a (2×2) reconstruction [150, 152, 155]. In an attempt to restore the α–Fe_2O_3 (0001) surface, the surface was annealed at 700 °C in 1×10^{-6} Torr O_2 for prolonged time. This prolonged annealing has led to the LEED pattern exhibited in figure (4.5d). Genuzio et al. have observed a similar LEED pattern during their preparation of α–Fe_2O_3 (0001) thin film on Pt (111) substrate [154]. They have attributed their observation to the coexistence of Fe_3O_4 and α–Fe_2O_3 domains [154]. The only difference between their pattern and our pattern in figure (4.6d) is that their LEED hexagonal spots characteristic of α–Fe_2O_3 has the biphase structure of FeO (111) and α–Fe_2O_3 (0001) [156]. The stoichiometric surface of α–Fe_2O_3 (0001) could have been restored except that, unfortunately, sample position and condition at that time did not encourage any further annealing.

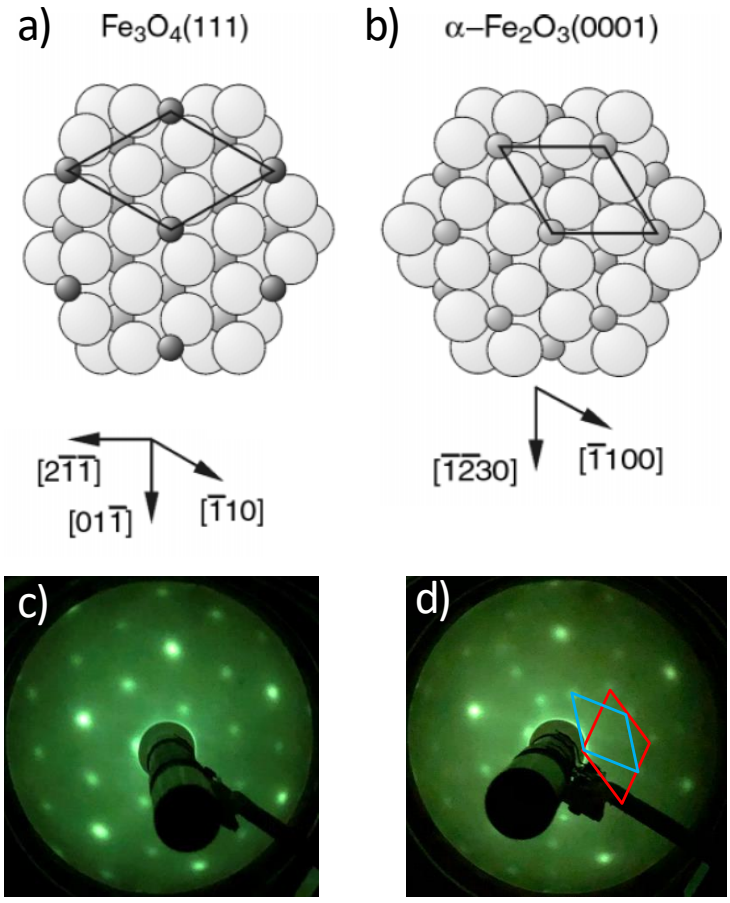

Figure 4.6. Crystal structures of a) Fe_3O_4 (111), and b) α–Fe_2O_3 (0001) surfaces (reproduced from reference [157] with permission from the PCCP Owner Societies). LEED patterns of α–Fe_2O_3 (0001) surfaces c) obtained after cycles of subsequent sputtering and annealing, d) after prolonged annealing at 700 °C in 1×10^{-6} Torr O_2, (E = 95 eV). This pattern shows coexisting domains of Fe_3O_4 (blue) and α–Fe_2O_3 (red).

Now looking at all the results obtained and starting by comparing the three difference spectra in figure (4.1b), one can see that both room temperature and high temperature difference doses share common features like phenol HOMO band as well as phenol-σ orbitals to some extent. This may lead one to suggest that the adsorption of phenol at elevated temperature did not degrade the phenyl ring into smaller hydrocarbon fragments. Another significant feature in figure (4.1b) is the clear observation of phenol HOMO and HOMO-1 bands at room temperature as well as at high temperature doses, and with $\Delta E = 1\ eV$. This finding is consistent with the DFT calculation of

electronic states of a single phenol molecule, except that the binding energies of both bands are lower than the predicted values [120, 121]. These two bands are found overlapped in the UPS spectrum of phenol ice; however, they clearly split in the room temperature spectrum with both bands having almost the same intensity. This might indicate that both bands are equally populated at room temperature adsorption. Notably, at the high temperature doses we observe an intense feature on the low binding energy side of the HOMO band, attributed to Fe^{2+}, presumably strongly hybridized with the HOMO band and resulting in the enhancement of its intensity. On the other hand, we see the HOMO-1 band shifts toward higher binding energy with its intensity almost diminishes at 800 L dose. The partial reduction of Fe^{3+} to Fe^{2+} can be considered as an evidence of electron charge transfer from the adsorbed phenol to the Fe^{3+} cations on the surface due to the chemisorption of the phenol molecule, which leads to the formation of EPFRs. This result agrees well with the proposed formation mechanism of EPFRs. Moreover, the dependence of adsorption behavior on temperature is manifested in $\sigma_{O\text{-}H}$ orbital which is observed in the room temperature spectrum indicating a molecular adsorption whereas the absence of this feature in the 400 L at high temperature implies that phenol chemisorbed dissociatively. The spectral changes seen in the emission from ~6 eV- 8.5 eV, which are attributed to electronic levels of the phenolic oxygen, might have to do with the nature of the bonding between the phenolic oxygen and the TMO surface and/or the orientation of the ring with respect to the surface.

The Fe 2p core level spectra confirm the results observed in UPS. The satellite at 719.3 eV characteristic of Fe^{3+} cations was not modified by the room temperature dose. However, at 400 L phenol at 250 °C, the intensity of the satellite was found to decrease along with broadness of the main photoelectron peak indicating partial reduction of the Fe^{3+} cations. On the other hand, the satellite is completely diminished and significant changes took place in the Fe 2p region for the

800 L phenol at 250 °C. Again, the reduction in Fe^{3+} cations is still partial though the density of Fe^{2+} states are higher in this coverage as indicated by the area at ~715 eV. That is, both oxidation states coexist together at elevated temperatures; however, 800L phenol dosing generates more Fe^{2+} states than 400 L phenol. Furthermore, the shift toward higher binding energy observed in O 1s core level spectra indicates a downward band bending in the higher temperature doses [145, 158].

Quantification of C 1s and O 1s core level spectra have provided a deeper insight into the formation of species on the surface due to phenol adsorption at different conditions. Observing both the hydroxyl group and the phenolic O in the O 1s room temperature spectrum may suggest that phenol ring has physisorbed on the dosed surface. However, C 1s spectrum of the same dose may support the same conclusion with the exception that the C-O:C-C ratio is higher than 1:5 which is the ratio indicative of phenol molecule. This can be explained by formation of a bonding between C in the ring with a nearby O in the lattice which may be allowed depending on the orientation of the physisorbed phenol molecule on the surface. On the other hand, the increase in the –OH, organic O, and π–π^* transition intensities associated with the appearance of C=O, and the further increase in the C-O:C-C ratio in the 800 L of phenol dosed at high temperature may indicate the chemisorption of phenol on iron cations and the formation of both carbon-centered and oxygen-centered phenoxyl-type radicals. It may also indicate the partial degradation of the formed phenoxyl radical to catechol. This might explain the changes observed in the electronic levels of phenolic oxygen in UPS spectra of elevated temperature doses.

4.4. Conclusion

This work has explored the formation mechanism of EPFRs by observing the adsorption of phenol on α–Fe_2O_3 (0001) surface as a function of dose and temperature to investigate the general assumption of EPFRs formation. Phenol was found to physisorb on the surface of α–Fe_2O_3

(0001) at room temperature dosing, as evident by observing $\sigma_{O\text{-}H}$ orbital in the respective UPS. Moreover, phenol HOMO and HOMO-1 bands, of room temperature dose, were not overlapped, unlike the case of the multilayers of physisorbed phenol at -173 °C. On the other hand, signs of phenol chemisorption on the surface of α–Fe_2O_3 (0001) were observed clearly at high temperature doses. Fe 2p core level spectra along with UPS spectra have clearly shown the partial reduction of of Fe^{3+} states to Fe^{2+} states. Also, O 1s peak were found to shift by 0.3 eV to higher binding energy, indicating a downward band bending. These two observations are evident of an electron transfer from the organic precursor to α–Fe_2O_3 (0001) surface. Also, all features related to phenol have been observed for both high temperature doses with different intensities implying that phenol has mainly chemisorbed with an intact phenyl ring. However, it is realized by quantifying and comparing O 1s and C 1s spectra that both carbon- and oxygen-centered phenoxyl radicals coexist on the surface and may be associated with catechol. This may imply that dosing iron oxide with phenol at high temperature may have activated certain surface sites which in turn have partially degraded the chemisorbed phenol.

Chapter 5. Effects of Simulated Solar Irradiation on EPFRs in Phenol/TiO_2 Nanoclusters

5.1. Introduction

EPFRs are pollutants that are found associated with airborne particulate matter (PM) generated in combustion systems [16]. Research has found that EPFRs are formed by the chemisorption of substituted aromatic (e.g. benzene) precursors on the surface of metal oxides. As stated in previous chapters, this chemisorption process involves an electron charge transfer between the organic precursor and the metal oxide surface, thus creating an oxygen- and/or carbon-centered free radical. EPFRs are long lived free radicals of which their half-lives can range from hours to days in ambient conditions and indefinitely in vacuum [17-19]. In this chapter, the effects of photodegradation is addressed. Again, it has been found that EPFRs-containing PM can cause serious health impacts to humans [1, 3, 56, 74, 75, 112, 138]. Upon their inhalation, they produce reactive oxygen species (ROS) which are known to cause oxidative stress and cell death in the living tissue [1, 72, 111, 138, 159], and hence it causes several cardiovascular and respiratory diseases [60, 61, 160].

Solar irradiation has been found to impact the generation and lifetime of EPFRs [142]. Jia et al. have reported that the 1/e lifetime of EPFRs detected on Fe(III)-montmorillonite containing polycyclic aromatic hydrocarbons (PAH) is significantly shortened due to solar irradiation [142]. They have also reported that solar irradiation promotes PAH transformation on the surface of clay minerals with much faster degradation rate [131, 132]. This result has been explained by the (solar) photo-induced production of ROS species which directly interact with EPFRs and lead it to degradation [142].

EPFRs produced by chemisorption of phenol on TiO_2 have been previously studied [16, 120]. It was found that phenoxyl radicals are the type of EPFRs formed with a high spin density and two decay behaviors with 1/e lifetimes of 4.3 and 57.4 days [16]. TiO_2 has also been employed as a

photocatalyst that facilitate the photodegradation of phenolic compounds in wastewater due to its high oxidation potential and band gap (~3 eV) which enable it to absorb the UV portion of the sunlight [161].

The mechanism of TiO_2 photocatalysis in water starts with absorption of UV light and consequent excitation of valence electrons resulting in creation of holes in the valence band (h_{vb}^{+}) and introduction of electrons in the conduction band (e_{cb}^{-}) of TiO_2 [161]. The ensuing holes can interact with the water adsorbed on TiO_2 and thus surface hydroxyl radicals ($HO^{\cdot}$) are produced, see equations (5.1) and (5.2). The photo-induced hydroxyl radical is a powerful oxidant that can totally decompose phenols to CO_2 and water if continuously produced [162]. However, photodegradation of the organic molecule is obstructed in the absence of molecular oxygen [163]. The role of adsorbed molecular oxygen is to scavenge the electrons produced in the conduction band, and therefore, it prevents the recombination of electrons and holes [162]. Consequently, the loss of photosensitivity of TiO_2 is inhibited by the presence of molecular oxygen. Also, the interaction between adsorbed molecular oxygen and conduction band electrons yields the formation of superoxide radical anions which in turn can further produce hydroxyl radicals, as seen by equations (5.3) to (5.6)

$$TiO_2 + h\nu \longrightarrow e_{cb}^{-} + h_{vb}^{+} \quad (5.1)$$

$$(H_2O)_{ads} + h_{vb}^{+} \longrightarrow HO_{ads}^{\cdot} + H^{+} \quad (5.2)$$

$$O_2 + e_{cb}^{-} \longrightarrow O_2^{\cdot -} \quad (5.3)$$

$$O_2^{\cdot -} + H^{+} \longrightarrow HO_2^{\cdot} \quad (5.4)$$

$$HO_2^{\cdot} + HO_2^{\cdot} \longrightarrow H_2O_2 + O_2 \quad (5.5)$$

$$H_2O_2 + e_{cb}^{-} \longrightarrow HO^{\cdot} + HO^{-} \quad (5.6)$$

The primary objective of this work is to study the effect of solar exposure in ambient atmosphere on the evolution and fate of EPFRs produced from phenols on nanoparticle size (18 nm) TiO_2 surface. We have initially produced EPFRs by chemisorbing phenol on TiO_2 surface at 250°C, our objective is achieved by probing the subsequent EPFR evolution upon sequentially increasing solar exposure time, using electron paramagnetic resonance (EPR) and Fourier transform Infrared spectroscopy (FTIR). This work is aimed at understanding the environmental behavior of the formed EPFRs which may contribute in developing future remediation strategies.

5.2. Experimental Methods

Experiments were performed on anatase TiO_2, CAS 13463-67-7, 289 m^2/g, 99.5% purity which were purchased from US Research Nanomaterials and used as-received. Phenol (CAS 108-95-2, ACS reagent grade, ≥ 99.0% pure) was purchased from Sigma-Aldrich and used without further purification.

Samples were prepared using the same dosing manifold described in previous work [12, 16]. In this work, TiO_2 nanoparticles powder samples were dosed by loading a small quantity (200-600 mg) of powder into a sample tube along with a small quantity (100-200 mg) of solid phenol. The filled tubed is then attached to the dosing system and heated for 1 hour to 250°C. The leak valve of the sample tube is then opened to the turbomolecular pump and pumped out to the turbo's base pressure (~10^{-4} mbar) while being heated for another 1 hour. After heating for a total time of two hours, the sample tube is left to cool down gradually to room temperature while being pumped continuously before removal from the dosing system for measurement. In this way, one can ensure that no excess solid phenol was present in the measured samples as evident by the lack of phenolic –OH mode in FTIR spectra (see section 5.3).

Dosed samples were placed in Suprasil EPR tubes and were irradiated by Wavelabs Sinus 70 solar simulator with spectral coverage from 365-1100 nm and AM1.5G spectral irradiance, see figure (5.1). The tubes were irradiated at different exposure times. EPR and FTIR measurements were taken immediately after solar exposure (first time exposure, 1^{st} exposure). Solar irradiated dosed samples were kept in their EPR tubes and were stored, in a dark environment and in a climate-controlled lab to avoid any possible photodegradation of EPFRs. Second time exposure (2^{nd} exposure) took place three days after the first time exposure, and again EPR was performed immediately after solar exposure.

Samples were analyzed under ambient conditions at room temperature using EPR spectroscopy and FTIR spectroscopy. EPR measurements were performed using Bruker EMXnano spectrometer with X-band, microwave power 100 mW, and microwave frequency of 9 GHz. The typical operating parameters were: microwave power of 0.3 mW, modulation amplitude 1 G, and time constant 40.96 ms. ATR-FTIR spectrograms were obtained using Bruker FTIR spectrometer. Each spectrum was obtained by averaging 64 scans recorded at 4 cm^{-1} resolution.

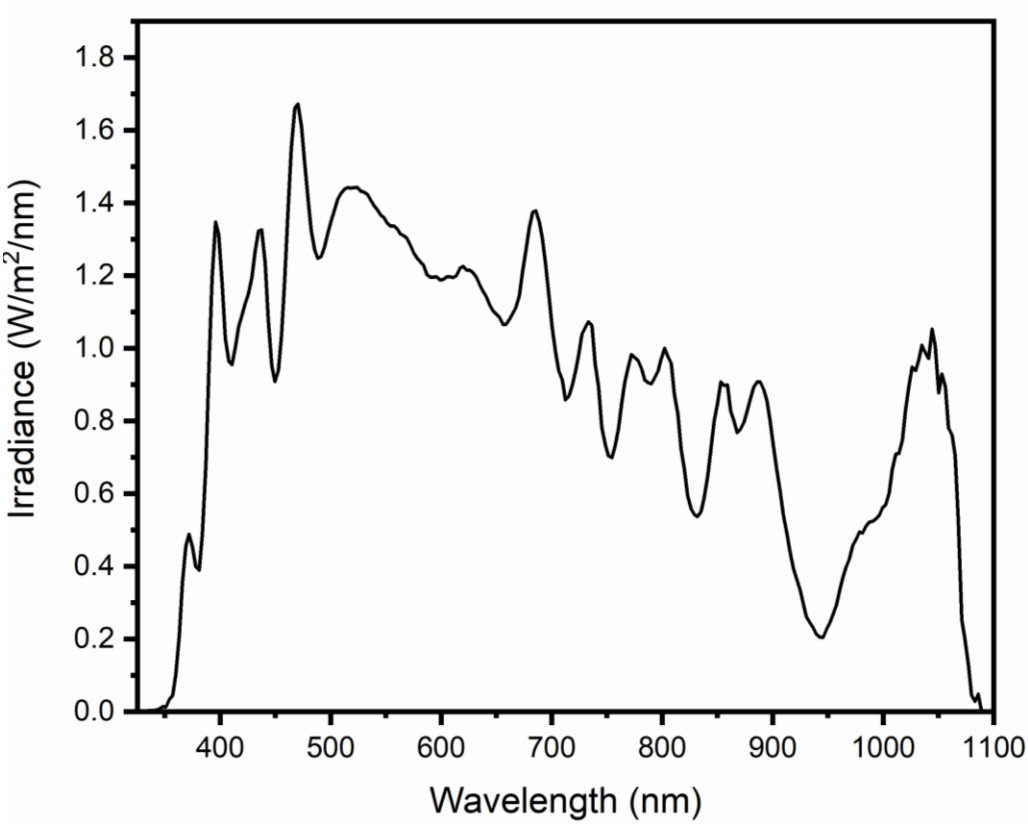

Figure 5.1. AM1.5G spectral irradiance curve measured at the sample position.

5.3. Results and Discussion

The evolution and changes of the chemisorbed EPFR on TiO_2 due to solar irradiation can be probed by comparing paramagnetic signal characteristics such as g-factor and spin density, as these parameters enable identification of the type and yield of the evolved EPFRs [142, 164]. EPFRs are initially generated by dosing anatase nanoparticles with phenol at 250°C. The dosed nano-powder is divided among five EPR tubes in which four of them were irradiated by solar simulated light at 20, 40, 60, and 90 minutes immediately after dosing (1st exposure). The irradiated dosed powder samples are irradiated once again three days after the first exposure (2nd exposure). EPR measurement performed on the non-irradiated dosed TiO_2 nanoparticles have shown a narrow paramagnetic signal characteristic of organic radical species. The g-factor of the paramagnetic signal obtained is 2.00332 which can be attributed to a phenoxyl-type radical that may have both

oxygen- and carbon-centered radicals (see figure (1.1)) [13]. Figure (5.2) shows the paramagnetic signals of phenol dosed TiO_2 irradiated with different exposure times (2^{nd} exposure data). It should be noted that undosed TiO_2 nanoparticles did not show any paramagnetic signal in this range of magnetic field. As seen from the figure, the relative intensity of the organic radical signal escalates as a function of exposure time accompanied with significant increase in ΔH_{p-p}. However, the trend exhibited by spin density with exposure time in 2^{nd} exposure is slightly different from that of 1^{st} exposure. Figure (5.3) shows the spin density as a function of exposure time for 1^{st} exposure and 2^{nd} exposure. In 1^{st} exposure, the radical yield at 20 minutes of exposure is 3 times higher than that of the non-irradiated sample. No significant increase in spin density beyond 20 minutes of solar exposure has been observed in the data obtained for 1^{st} exposure. However, in 2^{nd} exposure, the radical yield at 20 minutes of exposure is 10.3 times higher than that of the non-irradiated sample of 2^{nd} exposure. For greater exposure times, the spin density increases slightly. It should be noted that the overall spin density of 2^{nd} exposure is less than that of 1^{st} exposure and this is tentatively ascribed to the decay of EPFRs through the three days in dark storage.

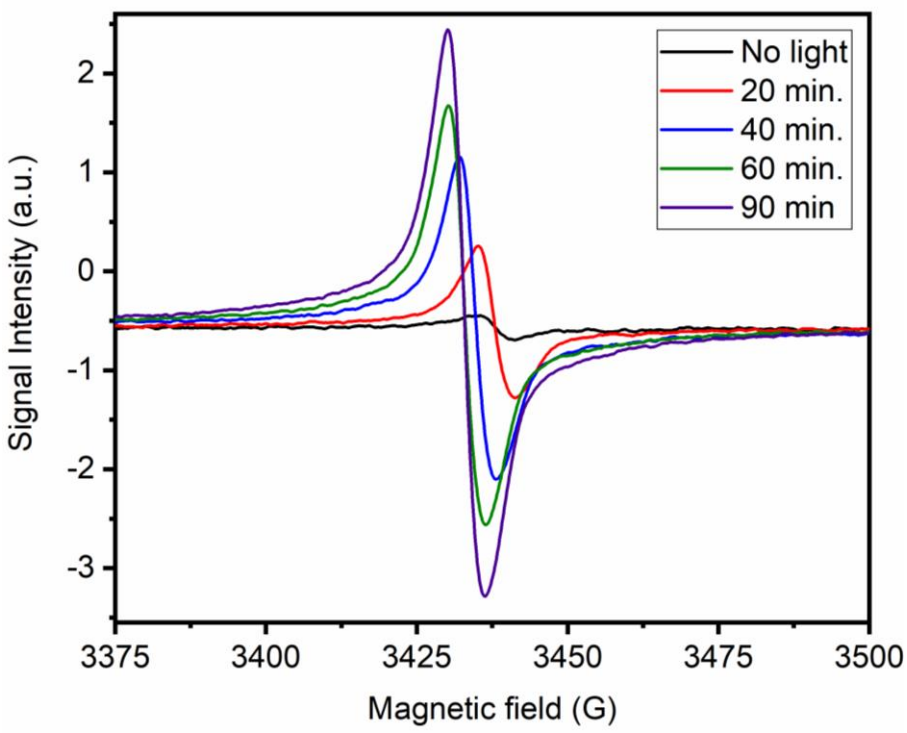

Figure 5.2. Electron paramagnetic resonance (EPR) spectra of solar irradiated phenol dosed TiO_2 at different exposure times and non-irradiated (black signal).

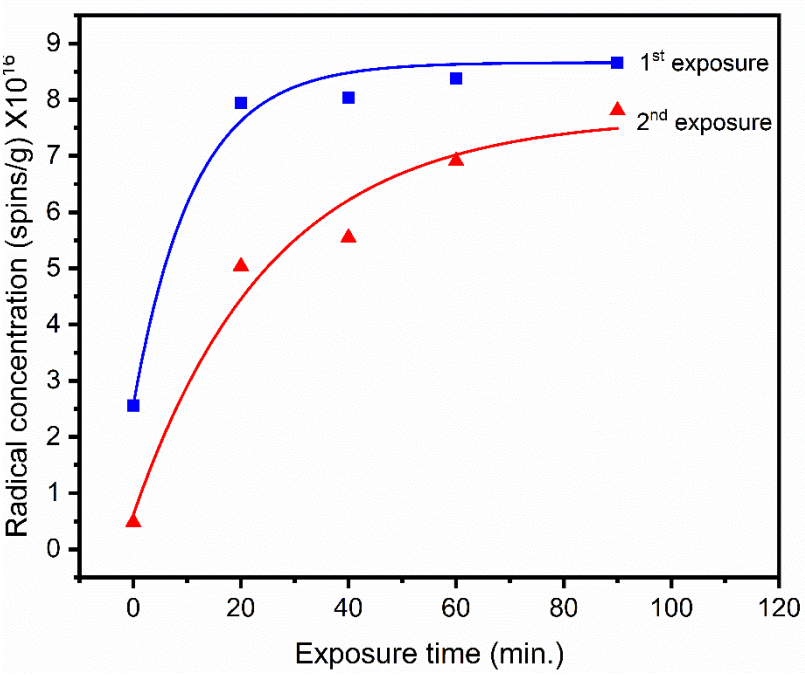

Figure 5.3. Relation between spin density and simulated solar irradiation at multiple exposure times for 1st and 2nd exposure times in which samples are irradiated immediately after dosing and 3 days later, respectively.

In order to examine the changes induced by solar irradiation on the type of EPFRs formed, the relation between g-factor and exposure time for 1st and 2nd exposure has been plotted in figure (5.4). In 1st exposure, the g-factor increases from 2.00332 to 2.00342 (at 90 min), whereas it increases from 2.00252 to 2.00259 (at 90 min) in 2nd exposure. The average increase in the g-factor can be attributed to the photo-oxidation of the existing EPFRs by solar irradiation in ambient air [165]. Similarly, the g-factor from 1st exposure drops significantly in 2nd exposure indicating the decay of oxygen-centered to carbon-centered radical species [17].

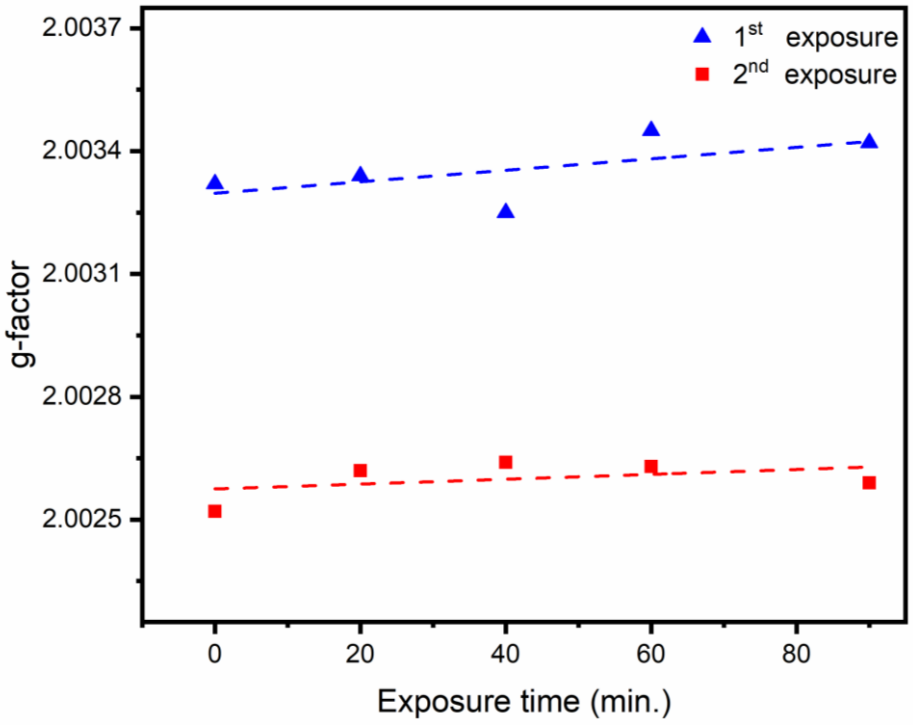

Figure 5.4. Relation between g-factor and simulated solar irradiation at multiple exposure times for day 1 and day 2 in which samples are irradiated immediately after dosing and 3 days later, respectively.

These results imply that, in 1st exposure, solar radiation has interacted with the freshly dosed TiO_2 yielding ~3 times more organic radicals species than the non-irradiated sample. These

induced organic radicals are more oxygen-centered indicating that phenoxyl is photo-oxidized by a hole hopping from the valence band of TiO_2 and/or by an interaction with a solar induced ROS. The degree to which phenoxyl is photodegraded and/or photo-induced depends on the amount of water and molecular oxygen adsorbed on the surface of TiO_2 nanoparticles during the photolysis [161]. This might explain the plateau observed in the spin density for exposure times greater than 20 minutes, particularly, in 1st exposure. We assume that the source of adsorbed water in this reaction comes from the humidity of the air trapped in the EPR tube, therefore, the reaction ceases when all water molecules trapped in the tube are consumed. In 2nd exposure, solar irradiation has induced radical species which are ~ 11 times higher in radical yield (at 20 min exposure) compared to the non-irradiated sample of 2nd exposure. This increase in photosensitivity can be attributed to the increase of humidity in the air trapped in the EPR tubes, as the samples were stored in ambient atmosphere for 3 days in darkness. The increase in water along with the exchanged oxygen have increased the photo-induced ROS which in turn generated more organic radicals. It seems that most of the water and air trapped in the EPR tube are consumed in the first 20 minutes of the reaction, therefore, radical yield does not increase significantly beyond 20 minutes of solar exposure.

FTIR spectroscopy is utilized to obtain more explicit picture of EPFRs' evolution due to solar irradiation. The purpose of performing FTIR is to potentially detect the signature of the photo-induced organic radicals. Figure (5.5) shows ATR-FTIR spectra of phenol dosed TiO_2 irradiated with solar light at different exposure times along with ATR-FTIR spectrum of solid phenol in the region between 1100-1700 cm^{-1}. Comparing the spectrum of solid phenol with phenol/TiO_2 spectra, we see the peak at 1593 cm^{-1} from solid phenol, which is attributed to pure C-C stretches in ring, is observed in all phenol/TiO_2 spectra at ~ 1593 cm^{-1}. Also, the two peaks at

1470 cm^{-1} and 1497 cm^{-1} collapse to a single peak at around 1489 cm^{-1}. The two peaks at 1470 cm^{-1} and 1497 cm^{-1} are attributed to a combination of ν(CC)+ν(CO) and δ(CH)+ν(CC) respectively in solid phenol. The broad band peaked at 1224 cm^{-1} in solid phenol which is a manifold of δ(OH) and ν(CO) modes is observed as a peak at ~1273 cm^{-1} with a shoulder at ~1218 cm^{-1}. The β(CH) in-plane bending modes are observed at 1164 cm^{-1} and 1151 cm^{-1}. Finally, absence of broad manifold of hydrogen-bonded OH bending modes centered at ~1368 cm^{-1}, which is observed in solid phenol is indicative of a dissociated adsorption mechanism to the surface of TiO_2 resulting in a chemisorbed phenoxyl-type surface species.

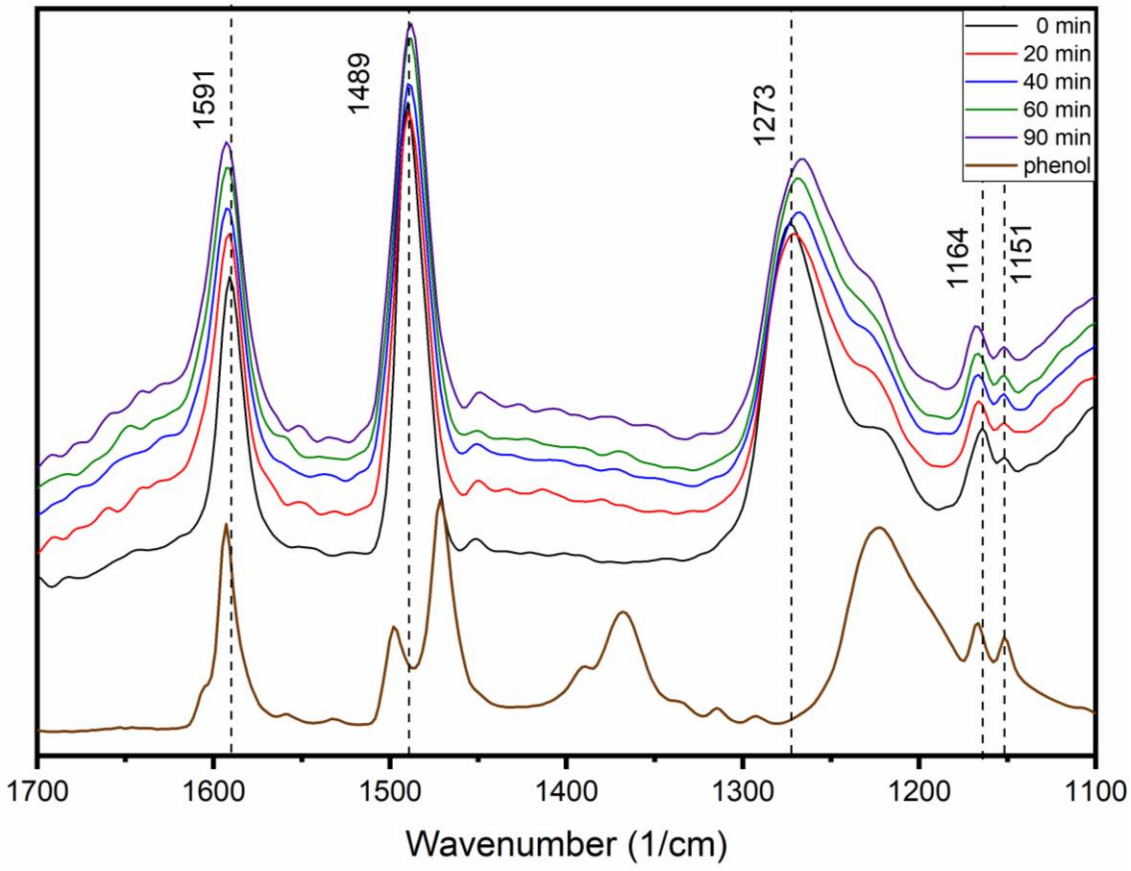

Figure 5.5. Comparison of ATR-FTIR spectrum of phenol (brown curve) and those of phenol adsorbed on anatase TiO_2 nanoparticles at 250°C and are irradiated with simulated solar light at different exposure times. Black curve is for non-irradiated phenol dosed TiO_2.

Comparing non-irradiated phenol/TiO_2 spectrum with solar irradiated phenol/TiO_2 spectra reveals an upward shift of the pure C-C stretches by ~ 3 cm^{-1} associated with increase in peak area on the left side of the peak. Also, the ring stretching mode at 1489 cm^{-1} shifts upward by ~ 1 cm^{-1} for 20- 60 min exposure whereas it shifts downward by ~ 1 cm^{-1} for the 90 min exposure. Furthermore, changes in the peak area on the left and right sides of the peak. The feature attributed to C-O stretch is significantly modified. The peak shifts downward by 2 cm^{-1} for 20 min exposure whereas it shifts downward by 6 cm^{-1} for 40-90 min exposures. Also, the shoulder at 1218 cm^{-1} shifts upward by ~ 8 cm^{-1} and the intensity ratio between the peak and shoulder decreases by half for all exposure times. Finally, the peak at 1164 shifts upward by 2 cm^{-1} for 20-60 min exposure and by 6 cm^{-1} for 90 min exposure.

Figure (5.6) shows the FTIR difference spectra which are generated by normalizing all phenol/TiO_2 spectra and taking the difference from the non-irradiated dosed spectrum. Four main features are observed at 1600 cm^{-1}, 1500 cm^{-1}, 1483 cm^{-1}, and 1234 cm^{-1} and are found to increase with exposure time. The peak at 1234 cm^{-1} represents a modification in the C-O bond whereas the peaks at 1500 $cm^{-1}$and 1483 cm^{-1} can be attributed to changes in the ring structure as compared to phenoxyl radical. The peak at 1600 cm^{-1} may be attributed to ν(C=O) which is characteristic of a quinone product, except that it is downshifted by 40 cm^{-1}. This peak can also be attributed to ν(CC)+ν(CO) stretching vibration of catechol. However, the FTIR spectrum of catechol/TiO_2 shows that ν(CC)+ν(CO) feature is a very weak and broad band compared to other features observed in the spectrum [166]. There is also a mild feature evolving with exposure time at ~1368.2 cm^{-1} which is characteristic of δ(OH) vibration mode of perhaps catechol and/or hydroquinone radical.

FTIR results indicate that phenol has initially degraded to phenoxyl radical upon its chemisorption on the surface of TiO_2 nanoparticle as evident by the absence of δ(OH) vibration mode. When the dosed samples become exposed to simulated solar radiation, the features observed implied further oxidation of the adsorbed phenoxyl radical. The extent of the photo-oxidation of phenoxyl radical is determined by the concentration of the photo-induced ROS. FTIR difference spectra suggests that the adsorbed phenoxyl radical has partially transformed to a mixture of catechol and some quinone product. These results are consistent with the mechanisms proposed for the degradation of phenol by hydroxyl radical [167, 168].

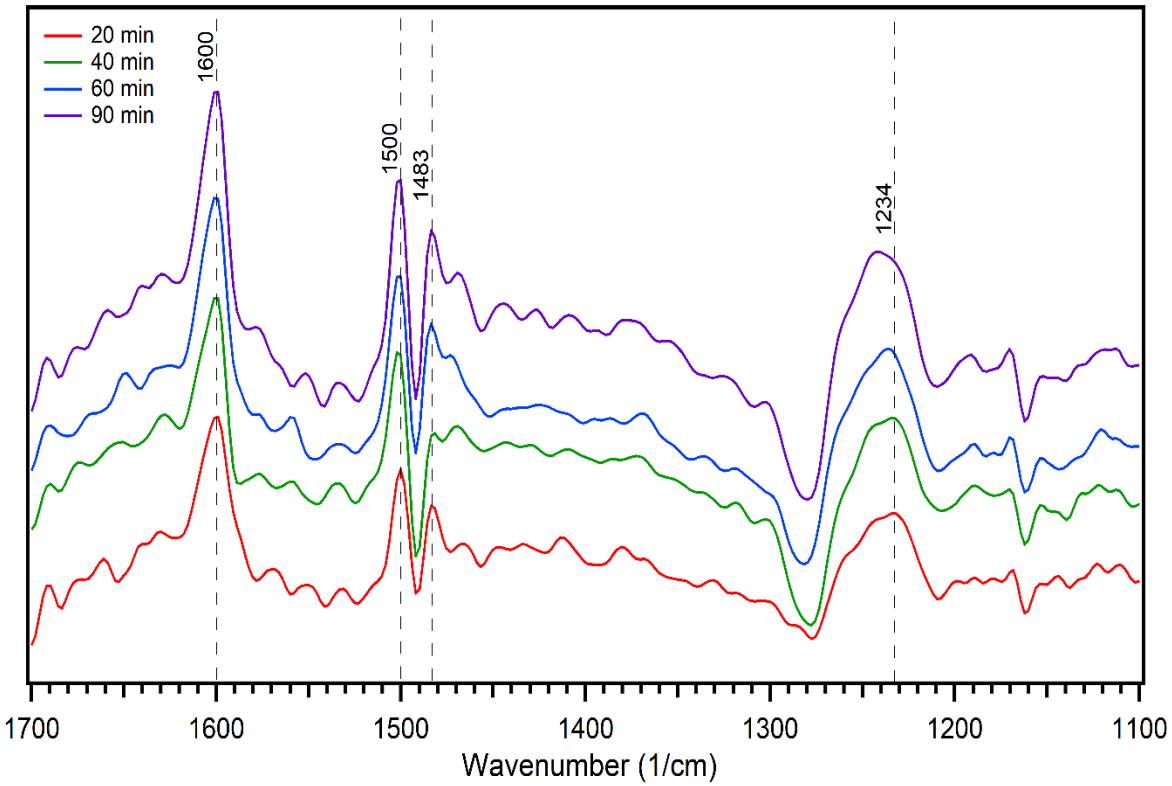

Figure 5.6. Comparison of ATR-FTIR difference spectra obtained from data in figure (5.5). The difference is generated by normalizing all spectra and subtracting the solar irradiated spectrum from the non-irradiated one.

5.4. Conclusion

In this work, we have studied the generation and evolution of EPFRs formed on the surface of TiO_2 nanoparticles by simulated solar irradiation at different exposure times. EPR has shown a significant increase in the radical spin density associated with an increase in g-factor for solar irradiated samples in day 1 and day 2 indicating the generation of organic radical species by photo-oxidation of the existing EPFRs as well as the physisorbed phenol molecules. Moreover, FTIR has revealed the initial formation of EPFRs through dissociative adsorption of phenol as seen by the absence of δ(OH) vibration mode. Effects of solar radiation at different exposure times have manifested as intensity changes and shifts in the main vibrational features of phenoxyl. FTIR difference spectra have shown features that can be attributed to the photo-induced EPFRs. The frequencies of the observed features suggest that the transformed EPFRs can be a mixture of catechol and some quinone product. The results of this work lead us to conclude that humid environments aid in the photodegradation of EPFRs associated PM and consequently to their faster decay.

Chapter 6. Summary

The studies presented in this dissertation have primarily focused at identifying the characteristics of EPFRs' formation and their catalyzed photodegradation on transition metal oxide systems. These studies have mainly investigated the vibrational features, the change in the chemical states, and the change in the electronic structure taking place at different metal oxide surfaces, and are induced by phenoxyl-type radical which is a type of EPFRs produced by the chemisorption of phenol on transition metal oxide surface. The purpose of the studies conducted is to gain an indepth understanding of EPFRs formation mechanism and their environmental induced transformation.

We have initially formed EPFRs by dosing, at high temperature, four different types of transition metal oxides nanoparticles which are abundant in EPFRs generated in combustion systems. The purpose of using nanoparticle size TMO was to mimic the EPFRs-associated $PM_{2.5}$ which are known to cause adverse health implications. FTIR and INS have enabled us to identify features characteristic of phenol chemisorption on metal oxide surface. Furthermore, FITR data taken after 18 days have shown the partial transformation of the phenolic features to other quinone products. Thus, we were able to verify, in part, one pathway of phenoxyl-radical decomposition. It is true that FTIR does not show strong features that can help distinguish between molecular and radical species. However, EPR results obtained from previous research aimed at studying the decay behavior of EPFRs, showed paramagnetic signal characteristic of organic radical still present in stored samples. On the other hand, our EPR results have helped us gain more insight into the role of metal oxide redox potential and its influence on its catalytic ability of producing EPFRs. The correlation between redox potential and radical yield allowed one to think that metal oxides which possess higher oxidation should generate high concentration of EPFRs. However, Fe_2O_3 NP, which

has highest oxidation potential compared to other metal oxides studied in this work, produced the least spin density. We inferred that the high reactivity of Fe_2O_3 may have consumed most of the EPFRs produced. Moreover, the highest radical yield in our study was observed in TiO_2 and it was attributed to the presence of superoxide species which are reported to be contained with metal oxide NP. Therefore, particle size impacts the reactivity of metal oxides not only because it offers larger surface area for organic precursors to adsorb, but also due to reactive species that enhances its catalytic ability. Finally, XPS enabled us to study the change in the chemical state of the studied metal oxides due to phenol adsorption. Metal cations of TiO_2 and CuO NPs were found to become partially reduced by phenol adsorption at high temperature, whereas ZnO and reduced-Fe_2O_3 NPs were partially oxidized. This result required us to reconsider the direction of electron transfer suggested by the proposed mechanism of EPFRs formation. Since ZnO has intrinsic defects and the reduced surface of Fe_2O_3 has likely induced defects, and defects are reported to act as active sites for adsorption, we attributed this results to the presence of defects. However, the direction of electron transfer is unclear. XPS ascertain the partial oxidation of the metal cations of ZnO and Fe_2O_3, but no information can be obtained about where this charge comes from using the techniques utilized in our study. Therefore, more comprehensive research should be conducted to study the mechanism of the chemisorption of organic precursors on defective sites existing on the surface of metal oxides.

Given the results of our first study, we were interested in investigating the adsorption behavior of phenol on the surface of α-Fe_2O_3 (0001) surface at both elevated and room temperature. The advantage of using single crystal compared to NP pellet lies in obtaining a single stoichiometric surface prior to dosing as confirmed by both photoemission techniques as well as LEED. Comparing UPS results of both room temperate and high temperature dosing, we found

that phenol has chemisorbed in both cases, except that the phenolic states are strongly perturbed at high temperature dosing associated with remarkable reduction of Fe^{3+} to Fe^{2+} states at high phenol coverage. Same results have been confirmed by XPS which have also shown an increase in the –OH as well as the appearance of C=O with increasing coverage of phenol at high temperature. This interesting result could indicate the formation of carbon-centered phenoxyl radicals or that high temperature has induced some defective sites that might have oxidized the adsorbed phenoxyl to other quinone products.

Finally, the environmental behavior of phenoxyl-type radical formed on the surface of anatase TiO_2 NPs has been investigated. We have found a significant increase in the EPFRs radical yield after 20 minutes of solar irradiation associated with increase in the g-factor. EPR results have been attributed to the photo-oxidation of the adsorbed phenolate species along with the existing phenoxyl radical. Moreover, FTIR difference spectra have given us more insight into the type of radicals and/or molecular species formed due to phenolate/phenoxyl photo-transformation. The observed features can be assigned to a mixture of catechol and a quinone product. It should be noted that the increase in radical yield of second day exposure was found more significant than first day exposure, and it was ascribed to the presence of more water molecules due to humidity in the air. Thus, it would be interesting to study EPFRs yield in humid versus dry environments.

Based on the work presented, it is essential to probe the influence of the type and density of defects in forming and transforming EPFRs. More interestingly to predict the mechanism by which organic precursors adsorb on defective sites as well as the pathway of electron transfer to metal cations in this case. Moreover, EPFRs yield dependence on transition metal oxide NPs size should be investigated and compared to obtain better understanding of the correlation between NPs size and the catalytic ability of the metal oxides involved. Finally, more research should be

focused on the environmental behavior of EPFRs. That is, the influence of molecular oxygen, water, and sunlight on the generation and fate of EPFRs existing in ambient environments.

Appendix A. Statements of Permission

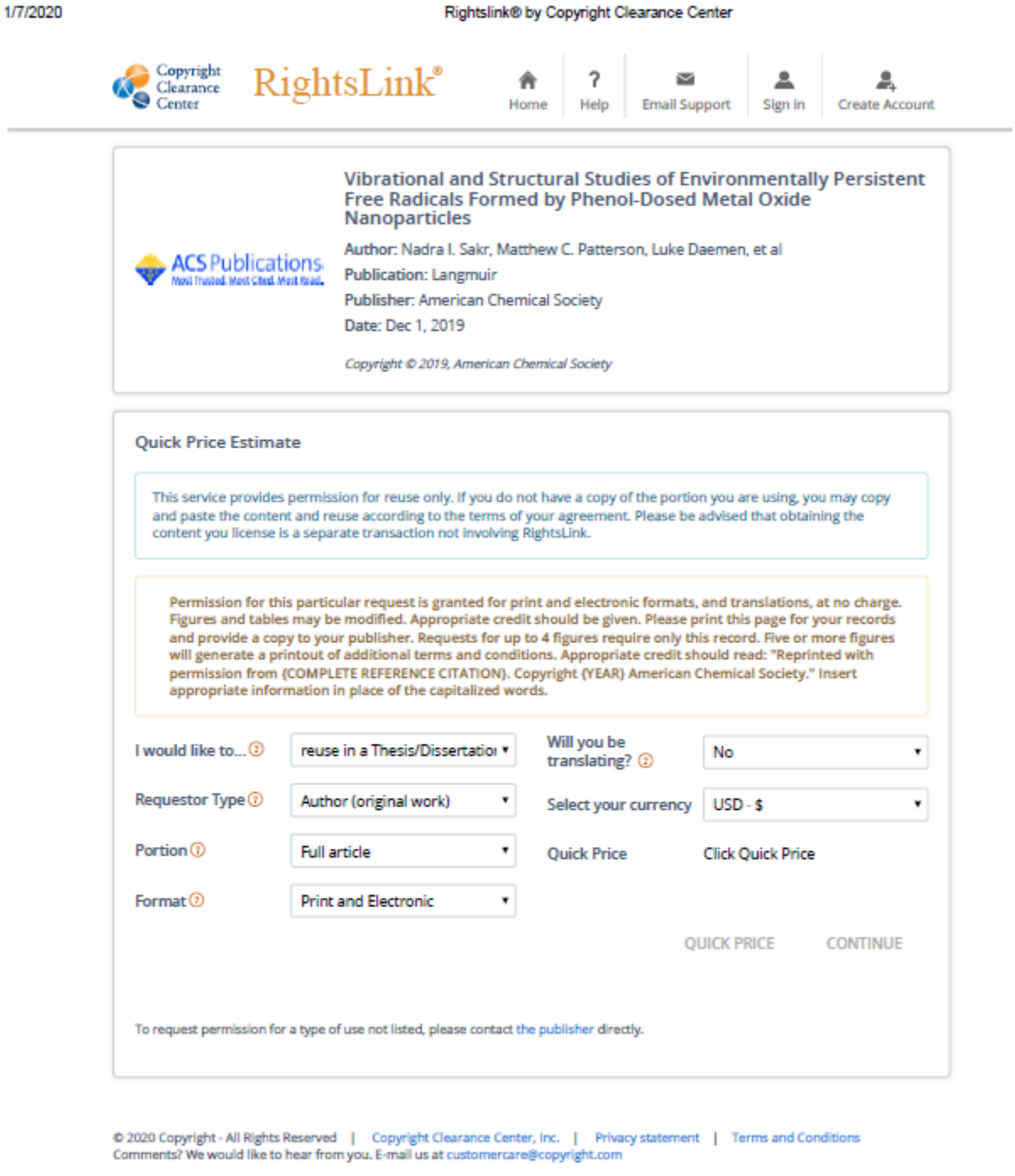

1/7/2020 Rightslink® by Copyright Clearance Center

Copyright Clearance Center RightsLink®

Home | Help | Email Support | Sign in | Create Account

ACS Publications

Vibrational and Structural Studies of Environmentally Persistent Free Radicals Formed by Phenol-Dosed Metal Oxide Nanoparticles

Author: Nadra I. Sakr, Matthew C. Patterson, Luke Daemen, et al

Publication: Langmuir

Publisher: American Chemical Society

Date: Dec 1, 2019

Copyright © 2019, American Chemical Society

Quick Price Estimate

This service provides permission for reuse only. If you do not have a copy of the portion you are using, you may copy and paste the content and reuse according to the terms of your agreement. Please be advised that obtaining the content you license is a separate transaction not involving RightsLink.

Permission for this particular request is granted for print and electronic formats, and translations, at no charge. Figures and tables may be modified. Appropriate credit should be given. Please print this page for your records and provide a copy to your publisher. Requests for up to 4 figures require only this record. Five or more figures will generate a printout of additional terms and conditions. Appropriate credit should read: "Reprinted with permission from {COMPLETE REFERENCE CITATION). Copyright {YEAR) American Chemical Society." Insert appropriate information in place of the capitalized words.

I would like to... reuse in a Thesis/Dissertatio

Will you be translating? No

Requestor Type Author (original work)

Select your currency USD - $

Portion Full article

Quick Price Click Quick Price

Format Print and Electronic

QUICK PRICE CONTINUE

To request permission for a type of use not listed, please contact the publisher directly.

© 2020 Copyright - All Rights Reserved | Copyright Clearance Center, Inc. | Privacy statement | Terms and Conditions

Comments? We would like to hear from you. E-mail us at customercare@copyright.com

Copyright Clearance Center

Note: Copyright.com supplies permissions but not the copyrighted content itself.

1 PAYMENT 2 REVIEW 3 CONFIRMATION

Step 3: Order Confirmation

Thank you for your order! A confirmation for your order will be sent to your account email address. If you have questions about your order, you can call us 24 hrs/day, M-F at +1.855.239.3415 Toll Free, or write to us at info@copyright.com. This is not an invoice.

Confirmation Number: 11847090
Order Date: 08/31/2019

If you paid by credit card, your order will be finalized and your card will be charged within 24 hours. If you choose to be invoiced, you can change or cancel your order until the invoice is generated.

Payment Information

Nadra Sakr
Louisiana State University
nsakr1@lsu.edu
Payment Method: n/a

Order Details

Journal of environmental monitoring

Order detail ID: 71998508
Order License Id: 4659480511624
ISSN: 1464-0333
Publication Type: e-Journal
Volume:
Issue:
Start page:
Publisher: ROYAL SOC OF CHEMISTRY
Author/Editor: Royal Society of Chemistry (Great Britain)

Permission Status: Granted
Permission type: Republish or display content
Type of use: Thesis/Dissertation
View details

Note: This item will be invoiced or charged separately through CCC's **RightsLink** service. More info **$ 0.00**

Total order items: 1

This is not an invoice.

Order Total: 0.00 USD

Environ Health Perspect. 2006 Jun; 114(6): 810–817. PMCID: PMC1480527
Published online 2006 Jan 26. doi: 10.1289/ehp.8629
Commentaries & Reviews

Origin and Health Impacts of Emissions of Toxic By-Products and Fine Particles from Combustion and Thermal Treatment of Hazardous Wastes and Materials

Stephania A. Cormier,[1] Slawo Lomnicki,[2] Wayne Backes,[3] and Barry Dellinger[2]

[1] Department of Biological Science and
[2] Department of Chemistry, Louisiana State University, Baton Rouge, Louisiana, USA
[3] Department of Pharmacology, Louisiana State University Health Sciences Center, Baton Rouge, Louisiana, USA
Address correspondence to S.A. Cormier, Louisiana State University, Department of Biological Sciences, 202 Life Sciences Building, Baton Rouge, LA 70803 USA. Telephone: (225) 578-0960. Fax: (225) 578-2597. E-mail: scormier@lsu.edu
The authors declare they have no competing financial interests.

Received 2005 Sep 4; Accepted 2006 Jan 26.

RightsLink®

Home | Account Info | Help | LIVE CHAT

WILEY

Book: Surface Analysis – The Principal Techniques
Publisher: John Wiley and Sons
Date: Dec 31, 1969

Logged in as:
Nadra Sakr
Louisiana State University
Account #:
3001044112
LOGOUT

Order Completed

Thank you for your order.

This Agreement between Louisiana State University -- Nadra Sakr ("You") and John Wiley and Sons ("John Wiley and Sons") consists of your license details and the terms and conditions provided by John Wiley and Sons and Copyright Clearance Center.

Your confirmation email will contain your order number for future reference.

printable details

License Number	4661850954121
License date	Sep 04, 2019
Licensed Content Publisher	John Wiley and Sons
Licensed Content Publication	Wiley Books
Licensed Content Date	Dec 31, 1969
Licensed Content Pages	10
Type of use	Dissertation/Thesis
Requestor type	University/Academic
Format	Electronic
Portion	Figure/table
Number of figures/tables	2
Original Wiley figure/table number(s)	Figure A1.2 Figure A1.5
Will you be translating?	No
Title of your thesis / dissertation	VIBRATIONAL AND ELECTRONIC STRUCTURE OF ENVIRONMETALLY PERSISTANT FREE RADICALS FORMED ON METAL OXIDE NANOCLUSTERS AND SINGLE-CRYSTAL SURFACES
Expected completion date	May 2020
Expected size (number of pages)	1
Requestor Location	Louisiana State University OCLC Headquarters, 6565 Kilgour Place Dublin, OH 43017 United States Attn: Louisiana State University
Publisher Tax ID	EU826007151
Total	0.00 USD

ORDER MORE CLOSE WINDOW

RightsLink®

Home | Account Info | Help

Title:	Basics of Continuous Wave EPR
Author:	Gareth R. Eaton, Sandra S. Eaton, David P. Barr et al
Publication:	Springer eBook
Publisher:	Springer Nature
Date:	Jan 1, 2010

Logged in as:
Nadra Sakr
Louisiana State University
LOGOUT

Order Completed

Thank you for your order.

This Agreement between Louisiana State University -- Nadra Sakr ("You") and Springer Nature ("Springer Nature") consists of your license details and the terms and conditions provided by Springer Nature and Copyright Clearance Center.

Your confirmation email will contain your order number for future reference.

printable details

License Number	4657720000112
License date	Aug 28, 2019
Licensed Content Publisher	Springer Nature
Licensed Content Publication	Springer eBook
Licensed Content Title	Basics of Continuous Wave EPR
Licensed Content Author	Gareth R. Eaton, Sandra S. Eaton, David P. Barr et al
Licensed Content Date	Jan 1, 2010
Type of Use	Thesis/Dissertation
Requestor type	academic/university or research institute
Format	electronic
Portion	figures/tables/illustrations
Number of figures/tables/illustrations	1
Will you be translating?	no
Circulation/distribution	<501
Author of this Springer Nature content	no
Title	VIBRATIONAL AND ELECTRONIC STRUCTURE OF ENVIRONMETALLY PERSISTANT FREE RADICALS FORMED ON METAL OXIDE NANOCLUSTERS AND SINGLE-CRYSTAL SURFACES
Institution name	Louisiana State University
Expected presentation date	May 2020
Order reference number	25
Portions	Figure 1.1
Requestor Location	Louisiana State University OCLC Headquarters, 6565 Kilgour Place Dublin, OH 43017 United States Attn: Louisiana State University
Total	0.00 USD

RightsLink®

Home | Account Info | Help

SPRINGER NATURE

Title:	Surface Analysis II. Electron Spectroscopy Methods
Author:	K. Oura, M. Katayama, A. V. Zotov et al
Publication:	Springer eBook
Publisher:	Springer Nature
Date:	Jan 1, 2003

Logged in as:
Nadra Sakr
Louisiana State University
Account #:
3001044112

LOGOUT

Order Completed

Thank you for your order.

This Agreement between Louisiana State University -- Nadra Sakr ("You") and Springer Nature ("Springer Nature") consists of your license details and the terms and conditions provided by Springer Nature and Copyright Clearance Center.

Your confirmation email will contain your order number for future reference.

printable details

License Number	4680941386407
License date	Oct 02, 2019
Licensed Content Publisher	Springer Nature
Licensed Content Publication	Springer eBook
Licensed Content Title	Surface Analysis II. Electron Spectroscopy Methods
Licensed Content Author	K. Oura, M. Katayama, A. V. Zotov et al
Licensed Content Date	Jan 1, 2003
Type of Use	Thesis/Dissertation
Requestor type	academic/university or research institute
Format	print and electronic
Portion	figures/tables/illustrations
Number of figures/tables/illustrations	1
Will you be translating?	no
Circulation/distribution	30 - 99
Author of this Springer Nature content	no
Title	VIBRATIONAL AND ELECTRONIC STRUCTURE OF ENVIRONMETALLY PERSISTANT FREE RADICALS FORMED ON METAL OXIDE NANOCLUSTERS AND SINGLE-CRYSTAL SURFACES
Institution name	Louisiana State University
Expected presentation date	May 2020
Portions	Figure 5.5
Requestor Location	Louisiana State University OCLC Headquarters, 6565 Kilgour Place Dublin, OH 43017 United States Attn: Louisiana State University
Total	0.00 USD

Order Completed

Thank you for your order.

This Agreement between Louisiana State University -- Nadra Sakr ("You") and Springer Nature ("Springer Nature") consists of your license details and the terms and conditions provided by Springer Nature and Copyright Clearance Center.

Your confirmation email will contain your order number for future reference.

printable details

License Number	4680260869057
License date	Oct 01, 2019
Licensed Content Publisher	Springer Nature
Licensed Content Publication	Springer eBook
Licensed Content Title	FOURIER TRANSFORM INFRARED SPECTROSCOPY
Licensed Content Author	Neena Jaggi, D.R. Vij
Licensed Content Date	Jan 1, 2006
Type of Use	Thesis/Dissertation
Requestor type	academic/university or research institute
Format	print and electronic
Portion	figures/tables/illustrations
Number of figures/tables/illustrations	1
Will you be translating?	no
Circulation/distribution	1 - 29
Author of this Springer Nature content	no
Title	VIBRATIONAL AND ELECTRONIC STRUCTURE OF ENVIRONMETALLY PERSISTANT FREE RADICALS FORMED ON METAL OXIDE NANOCLUSTERS AND SINGLE-CRYSTAL SURFACES
Institution name	Louisiana State University
Expected presentation date	May 2020
Order reference number	112
Portions	Figure 9.1
Requestor Location	Louisiana State University OCLC Headquarters, 6565 Kilgour Place Dublin, OH 43017 United States Attn: Louisiana State University
Total	0.00 USD

Copyright Clearance Center

Note: Copyright.com supplies permissions but not the copyrighted content itself.

1 PAYMENT 2 REVIEW **3 CONFIRMATION**

Step 3: Order Confirmation

Thank you for your order! A confirmation for your order will be sent to your account email address. If you have questions about your order, you can call us 24 hrs/day, M-F at +1.855.239.3415 Toll Free, or write to us at info@copyright.com. This is not an invoice.

Confirmation Number: 11847972
Order Date: 09/04/2019

If you paid by credit card, your order will be finalized and your card will be charged within 24 hours. If you choose to be invoiced, you can change or cancel your order until the invoice is generated.

Payment Information

Nadra Sakr
Louisiana State University
nsakr1@lsu.edu
Payment Method: n/a

Order Details

Physics of surfaces and interfaces

Order detail ID:	72000692
Order License Id:	4661860528543
ISBN:	9783540347095
Publication Type:	Book
Publisher:	SPRINGER
Author/Editor:	IBACH, H.

Permission Status: Granted
Permission type: Republish or display content
Type of use: Thesis/Dissertation

Requestor type	Not-for-profit entity
Format	Electronic
Portion	chart/graph/table/figure
Number of charts/graphs/tables/figures	3
The requesting person/organization	Louisiana State University
Title or numeric reference of the portion(s)	Figure 2.7, Figure 2.10, Figure 2.21
Title of the article or chapter the portion is from	Basic techniques
Editor of portion(s)	N/A

Author of portion(s)	Ibach, H
Volume of serial or monograph	N/A
Page range of portion	72-90
Publication date of portion	2006
Rights for	Main product
Duration of use	Life of current edition
Creation of copies for the disabled	no
With minor editing privileges	no
For distribution to	United States and Canada
In the following language(s)	Original language of publication
With incidental promotional use	no
Lifetime unit quantity of new product	Up to 499
Title	VIBRATIONAL AND ELECTRONIC STRUCTURE OF ENVIRONMETALLY PERSISTANT FREE RADICALS FORMED ON METAL OXIDE NANOCLUSTERS AND SINGLE-CRYSTAL SURFACES
Institution name	Louisiana State University
Expected presentation date	May 2020

Note: This item will be invoiced or charged separately through CCC's **RightsLink** service. More info **$ 0.00**

This is not an invoice.

Total order items: 1 **Order Total: 0.00 USD**

Confirmation Number: 11847972

Special Rightsholder Terms & Conditions

The following terms & conditions apply to the specific publication under which they are listed

Physics of surfaces and interfaces
Permission type: Republish or display content
Type of use: Thesis/Dissertation

TERMS AND CONDITIONS

The following terms are individual to this publisher:

A maximum of 10% of the content may be licensed for republication.

The user is responsible for identifying and seeking separate licenses for any third party materials that are identified anywhere in the work. Without a separate license, such third party materials may not be reused.

Other Terms and Conditions:

STANDARD TERMS AND CONDITIONS

1. Description of Service; Defined Terms. This Republication License enables the User to obtain licenses for republication of one or more copyrighted works as described in detail on the relevant Order Confirmation (the "Work(s)"). Copyright Clearance Center, Inc. ("CCC") grants licenses through the Service on behalf of the rightsholder identified on the Order Confirmation (the "Rightsholder"). "Republication", as used herein, generally means the inclusion of a Work, in whole or in part, in a new work or works, also as described on the Order Confirmation. "User", as used herein, means the person or entity making such republication.

2. The terms set forth in the relevant Order Confirmation, and any terms set by the Rightsholder with respect to a particular Work, govern the terms of use of Works in connection with the Service. By using the Service, the person transacting for a republication license on behalf of the User represents and warrants that he/she/it (a) has been duly authorized by the User to accept, and hereby does accept, all such terms and conditions on behalf of User, and (b) shall inform User of all such terms and conditions. In the event such person is a "freelancer" or other third party independent of User and CCC, such party shall be deemed jointly a "User" for purposes of these terms and conditions. In any event, User shall be deemed to have accepted and agreed to all such terms and conditions if User republishes the Work in any fashion.

3. Scope of License; Limitations and Obligations.

3.1 All Works and all rights therein, including copyright rights, remain the sole and exclusive property of the Rightsholder. The license created by the exchange of an Order Confirmation (and/or any invoice) and payment by User of the full amount set forth on that document includes only those rights expressly set forth in the Order Confirmation and in these terms and conditions, and conveys no other rights in the Work(s) to User. All rights not expressly granted are hereby reserved.

3.2 General Payment Terms: You may pay by credit card or through an account with us payable at the end of the month. If you and we agree that you may establish a standing account with CCC, then the following terms apply: Remit Payment to: Copyright Clearance Center, 29118 Network Place, Chicago, IL 60673-1291. Payments Due: Invoices are payable upon their delivery to you (or upon our notice to you that they are available to you for downloading). After 30 days, outstanding amounts will be subject to a service charge of 1-1/2% per month or, if less, the maximum rate allowed by applicable law. Unless otherwise specifically set forth in the Order Confirmation or in a separate written agreement signed by CCC, invoices are due and payable on "net 30" terms. While User may exercise the rights licensed immediately upon issuance of the Order Confirmation, the license is automatically revoked and is null and void, as if it had never been issued, if complete payment for the license is not received on a timely basis either from User directly or through a payment agent, such as a credit card company.

3.3 Unless otherwise provided in the Order Confirmation, any grant of rights to User (i) is "one-time" (including the editions and product family specified in the license), (ii) is non-exclusive and non-transferable and (iii) is subject to any and all limitations and restrictions (such as, but not limited to, limitations on duration of use or circulation) included in the Order Confirmation or invoice and/or in these terms and conditions. Upon completion of the licensed use, User shall either secure a new permission for further use of the Work(s) or immediately cease any new use of the Work(s) and shall render inaccessible (such as by deleting or by removing or severing links or other locators) any further copies of the Work (except for copies printed on paper in accordance with this license and still in User's stock at the end of such period).

3.4 In the event that the material for which a republication license is sought includes third party materials (such as photographs, illustrations, graphs, inserts and similar materials) which are identified in such material as having been used by permission, User is responsible for identifying, and seeking separate licenses (under this Service or otherwise) for, any of such third party materials; without a separate license, such third party materials may not be used.

3.5 Use of proper copyright notice for a Work is required as a condition of any license granted under the Service. Unless otherwise provided in the Order Confirmation, a proper copyright notice will read substantially as follows: "Republished with permission of [Rightsholder's name], from [Work's title, author, volume, edition number and year of copyright];

permission conveyed through Copyright Clearance Center, Inc. " Such notice must be provided in a reasonably legible font size and must be placed either immediately adjacent to the Work as used (for example, as part of a by-line or footnote but not as a separate electronic link) or in the place where substantially all other credits or notices for the new work containing the republished Work are located. Failure to include the required notice results in loss to the Rightsholder and CCC, and the User shall be liable to pay liquidated damages for each such failure equal to twice the use fee specified in the Order Confirmation, in addition to the use fee itself and any other fees and charges specified.

3.6 User may only make alterations to the Work if and as expressly set forth in the Order Confirmation. No Work may be used in any way that is defamatory, violates the rights of third parties (including such third parties' rights of copyright, privacy, publicity, or other tangible or intangible property), or is otherwise illegal, sexually explicit or obscene. In addition, User may not conjoin a Work with any other material that may result in damage to the reputation of the Rightsholder. User agrees to inform CCC if it becomes aware of any infringement of any rights in a Work and to cooperate with any reasonable request of CCC or the Rightsholder in connection therewith.

4. Indemnity. User hereby indemnifies and agrees to defend the Rightsholder and CCC, and their respective employees and directors, against all claims, liability, damages, costs and expenses, including legal fees and expenses, arising out of any use of a Work beyond the scope of the rights granted herein, or any use of a Work which has been altered in any unauthorized way by User, including claims of defamation or infringement of rights of copyright, publicity, privacy or other tangible or intangible property.

5. Limitation of Liability. UNDER NO CIRCUMSTANCES WILL CCC OR THE RIGHTSHOLDER BE LIABLE FOR ANY DIRECT, INDIRECT, CONSEQUENTIAL OR INCIDENTAL DAMAGES (INCLUDING WITHOUT LIMITATION DAMAGES FOR LOSS OF BUSINESS PROFITS OR INFORMATION, OR FOR BUSINESS INTERRUPTION) ARISING OUT OF THE USE OR INABILITY TO USE A WORK, EVEN IF ONE OF THEM HAS BEEN ADVISED OF THE POSSIBILITY OF SUCH DAMAGES. In any event, the total liability of the Rightsholder and CCC (including their respective employees and directors) shall not exceed the total amount actually paid by User for this license. User assumes full liability for the actions and omissions of its principals, employees, agents, affiliates, successors and assigns.

6. Limited Warranties. THE WORK(S) AND RIGHT(S) ARE PROVIDED "AS IS". CCC HAS THE RIGHT TO GRANT TO USER THE RIGHTS GRANTED IN THE ORDER CONFIRMATION DOCUMENT. CCC AND THE RIGHTSHOLDER DISCLAIM ALL OTHER WARRANTIES RELATING TO THE WORK(S) AND RIGHT(S), EITHER EXPRESS OR IMPLIED, INCLUDING WITHOUT LIMITATION IMPLIED WARRANTIES OF MERCHANTABILITY OR FITNESS FOR A PARTICULAR PURPOSE. ADDITIONAL RIGHTS MAY BE REQUIRED TO USE ILLUSTRATIONS, GRAPHS, PHOTOGRAPHS, ABSTRACTS, INSERTS OR OTHER PORTIONS OF THE WORK (AS OPPOSED TO THE ENTIRE WORK) IN A MANNER CONTEMPLATED BY USER; USER UNDERSTANDS AND AGREES THAT NEITHER CCC NOR THE RIGHTSHOLDER MAY HAVE SUCH ADDITIONAL RIGHTS TO GRANT.

7. Effect of Breach. Any failure by User to pay any amount when due, or any use by User of a Work beyond the scope of the license set forth in the Order Confirmation and/or these terms and conditions, shall be a material breach of the license created by the Order Confirmation and these terms and conditions. Any breach not cured within 30 days of written notice thereof shall result in immediate termination of such license without further notice. Any unauthorized (but licensable) use of a Work that is terminated immediately upon notice thereof may be liquidated by payment of the Rightsholder's ordinary license price therefor; any unauthorized (and unlicensable) use that is not terminated immediately for any reason (including, for example, because materials containing the Work cannot reasonably be recalled) will be subject to all remedies available at law or in equity, but in no event to a payment of less than three times the Rightsholder's ordinary license price for the most closely analogous licensable use plus Rightsholder's and/or CCC's costs and expenses incurred in collecting such payment.

8. **Miscellaneous.**

8.1 User acknowledges that CCC may, from time to time, make changes or additions to the Service or to these terms and conditions, and CCC reserves the right to send notice to the User by electronic mail or otherwise for the purposes of notifying User of such changes or additions; provided that any such changes or additions shall not apply to permissions already secured and paid for.

8.2 Use of User-related information collected through the Service is governed by CCC's privacy policy, available online here: http://www.copyright.com/content/cc3/en/tools/footer/privacypolicy.html.

8.3 The licensing transaction described in the Order Confirmation is personal to User. Therefore, User may not assign or transfer to any other person (whether a natural person or an organization of any kind) the license created by the Order Confirmation and these terms and conditions or any rights granted hereunder; provided, however, that User may assign such license in its entirety on written notice to CCC in the event of a transfer of all or substantially all of User's rights in the new material which includes the Work(s) licensed under this Service.

8.4 No amendment or waiver of any terms is binding unless set forth in writing and signed by the parties. The Rightsholder and CCC hereby object to any terms contained in any writing prepared by the User or its principals, employees, agents or affiliates and purporting to govern or otherwise relate to the licensing transaction described in the Order Confirmation, which terms are in any way inconsistent with any terms set forth in the Order Confirmation and/or in these terms and conditions or CCC's standard operating procedures, whether such writing is prepared prior to, simultaneously with or subsequent to the Order Confirmation, and whether such writing appears on a copy of the Order Confirmation or in a separate instrument.

8.5 The licensing transaction described in the Order Confirmation document shall be governed by and construed under the law of the State of New York, USA, without regard to the principles thereof of conflicts of law. Any case, controversy, suit, action, or proceeding arising out of, in connection with, or related to such licensing transaction shall be brought, at CCC's sole discretion, in any federal or state court located in the County of New York, State of New York, USA, or in any federal or state court whose geographical jurisdiction covers the location of the Rightsholder set forth in the Order Confirmation. The parties expressly submit to the personal jurisdiction and venue of each such federal or state court.If

you have any comments or questions about the Service or Copyright Clearance Center, please contact us at 978-750-8400 or send an e-mail to info@copyright.com.

v 1.1

Close

Order Completed

Thank you for your order.

This Agreement between Louisiana State University -- Nadra Sakr ("You") and Springer Nature ("Springer Nature") consists of your license details and the terms and conditions provided by Springer Nature and Copyright Clearance Center.

Your confirmation email will contain your order number for future reference.

printable details

License Number	4680890847366
License date	Oct 02, 2019
Licensed Content Publisher	Springer Nature
Licensed Content Publication	Springer eBook
Licensed Content Title	Structure of Surfaces
Licensed Content Date	Jan 1, 2006
Type of Use	Thesis/Dissertation
Requestor type	academic/university or research institute
Format	print and electronic
Portion	figures/tables/illustrations
Number of figures/tables/illustrations	1
Will you be translating?	no
Circulation/distribution	1 - 29
Author of this Springer Nature content	no
Title	VIBRATIONAL AND ELECTRONIC STRUCTURE OF ENVIRONMETALLY PERSISTANT FREE RADICALS FORMED ON METAL OXIDE NANOCLUSTERS AND SINGLE-CRYSTAL SURFACES
Institution name	Louisiana State University
Expected presentation date	May 2020
Portions	Figure 1.2
Requestor Location	Louisiana State University OCLC Headquarters, 6565 Kilgour Place Dublin, OH 43017 United States Attn: Louisiana State University
Total	0.00 USD

ORDER MORE CLOSE WINDOW

Title:	Iron oxide surfaces
Author:	Gareth S. Parkinson
Publication:	Surface Science Reports
Publisher:	Elsevier
Date:	March 2016

Order Completed

Thank you for your order.

This Agreement between Louisiana State University -- Nadra Sakr ("You") and Elsevier ("Elsevier") consists of your license details and the terms and conditions provided by Elsevier and Copyright Clearance Center.

Your confirmation email will contain your order number for future reference.

printable details

License Number	4680900398610
License date	Oct 02, 2019
Licensed Content Publisher	Elsevier
Licensed Content Publication	Surface Science Reports
Licensed Content Title	Iron oxide surfaces
Licensed Content Author	Gareth S. Parkinson
Licensed Content Date	Mar 1, 2016
Licensed Content Volume	71
Licensed Content Issue	1
Licensed Content Pages	94
Type of Use	reuse in a thesis/dissertation
Portion	figures/tables/illustrations
Number of figures/tables/illustrations	1
Format	both print and electronic
Are you the author of this Elsevier article?	No
Will you be translating?	No
Original figure numbers	figure 41
Title of your thesis/dissertation	VIBRATIONAL AND ELECTRONIC STRUCTURE OF ENVIRONMETALLY PERSISTANT FREE RADICALS FORMED ON METAL OXIDE NANOCLUSTERS AND SINGLE-CRYSTAL SURFACES
Publisher of new work	Louisiana State University
Expected completion date	May 2020
Estimated size (number of pages)	1
Requestor Location	Louisiana State University OCLC Headquarters, 6565 Kilgour Place Dublin, OH 43017 United States Attn: Louisiana State University

RightsLink®

Home | Account Info | Help | LIVE CHAT

WILEY

Book: Surface Analysis – The Principal Techniques
Publisher: John Wiley and Sons
Date: Dec 31, 1969

Logged in as:
Nadra Sakr
Louisiana State University
Account #:
3001044112
LOGOUT

Order Completed

Thank you for your order.

This Agreement between Louisiana State University -- Nadra Sakr ("You") and John Wiley and Sons ("John Wiley and Sons") consists of your license details and the terms and conditions provided by John Wiley and Sons and Copyright Clearance Center.

Your confirmation email will contain your order number for future reference.

printable details

License Number	4680891366758
License date	Oct 02, 2019
Licensed Content Publisher	John Wiley and Sons
Licensed Content Publication	Wiley Books
Licensed Content Date	Dec 31, 1969
Licensed Content Pages	10
Type of use	Dissertation/Thesis
Requestor type	University/Academic
Format	Print and electronic
Portion	Figure/table
Number of figures/tables	1
Original Wiley figure/table number(s)	figure 7.7
Will you be translating?	No
Title of your thesis / dissertation	VIBRATIONAL AND ELECTRONIC STRUCTURE OF ENVIRONMETALLY PERSISTANT FREE RADICALS FORMED ON METAL OXIDE NANOCLUSTERS AND SINGLE-CRYSTAL SURFACES
Expected completion date	May 2020
Expected size (number of pages)	1
Requestor Location	Louisiana State University OCLC Headquarters, 6565 Kilgour Place Dublin, OH 43017 United States Attn: Louisiana State University
Publisher Tax ID	EU826007151
Total	0.00 USD

ORDER MORE CLOSE WINDOW

Permission Request Submitted

Your request is now under review.
You will be notified of the decision via email.
Please print this request for your records.

printable details

Order Number	501518068
Order Date	Oct 02, 2019
Licensed Content Publisher	John Wiley and Sons
Licensed Content Publication	Wiley Books
Licensed Content Title	X-ray Photoelectron Spectroscopy: An introduction to Principles and Practices
Licensed Content Author	Paul van der Heide
Licensed Content Date	Dec 1, 2011
Licensed Content Pages	1
Type of use	Dissertation/Thesis
Requestor type	University/Academic
Format	Print and electronic
Portion	Figure/table
Number of figures/tables	4
Original Wiley figure/table number(s)	figure 4.6, figure 5.1, figure 5.13, figure 5.18
Will you be translating?	No
Title of your thesis / dissertation	VIBRATIONAL AND ELECTRONIC STRUCTURE OF ENVIRONMETALLY PERSISTANT FREE RADICALS FORMED ON METAL OXIDE NANOCLUSTERS AND SINGLE-CRYSTAL SURFACES
Expected completion date	May 2020
Expected size (number of pages)	1
Requestor Location	Louisiana State University OCLC Headquarters, 6565 Kilgour Place Dublin, OH 43017 United States Attn: Louisiana State University
Publisher Tax ID	EU826007151
Total	Not Available

ORDER MORE CLOSE WINDOW

SPRINGER NATURE LICENSE TERMS AND CONDITIONS

Aug 28, 2019

This Agreement between Louisiana State University -- Nadra Sakr ("You") and Springer Nature ("Springer Nature") consists of your license details and the terms and conditions provided by Springer Nature and Copyright Clearance Center.

License Number	4657720000112
License date	Aug 28, 2019
Licensed Content Publisher	Springer Nature
Licensed Content Publication	Springer eBook
Licensed Content Title	Basics of Continuous Wave EPR
Licensed Content Author	Gareth R. Eaton, Sandra S. Eaton, David P. Barr et al
Licensed Content Date	Jan 1, 2010
Type of Use	Thesis/Dissertation
Requestor type	academic/university or research institute
Format	electronic
Portion	figures/tables/illustrations
Number of figures/tables/illustrations	1
Will you be translating?	no
Circulation/distribution	<501
Author of this Springer Nature content	no
Title	VIBRATIONAL AND ELECTRONIC STRUCTURE OF ENVIRONMETALLY PERSISTANT FREE RADICALS FORMED ON METAL OXIDE NANOCLUSTERS AND SINGLE-CRYSTAL SURFACES
Institution name	Louisiana State University
Expected presentation date	May 2020
Order reference number	25
Portions	Figure 1.1
Requestor Location	Louisiana State University OCLC Headquarters, 6565 Kilgour Place Dublin, OH 43017 United States Attn: Louisiana State University
Total	0.00 USD
Terms and Conditions	

Springer Nature Customer Service Centre GmbH Terms and Conditions

This agreement sets out the terms and conditions of the licence (the **Licence**) between you and **Springer Nature Customer Service Centre GmbH** (the **Licensor**). By clicking

Copyright Clearance Center Marketplace™

Order Confirmation

This is not an invoice. Please go to manage account to access your order history and invoices.

CUSTOMER INFORMATION

Billing Address

Jackie Fahmy
Louisiana State University
OCLC Headquarters, 6565 Kilgour Place
Dublin, OH 43017
United States

fahmyj@oclc.org

Customer Location

Jackie Fahmy
Louisiana State University
OCLC Headquarters, 6565 Kilgour Place
Dublin, OH 43017
United States

PO Number (optional)

N/A

Payment options

Invoice

PENDING ORDER CONFIRMATION

Total Due: 0.00 USD

Confirmation Number: Pending

Order Date: 15-Nov-2019

1. Physical chemistry chemical physics

0.00 USD

Order license ID	Pending
ISSN	1463-9084
Type of Use	Republish in a thesis/dissertation
Publisher	ROYAL SOCIETY OF CHEMISTRY
Portion	Image/photo/illustration

LICENSED CONTENT

Publication Title	Physical chemistry chemical physics	**Country**	United Kingdom of Great Britain and Northern Ireland
Author/Editor	Royal Society of Chemistry (Great Britain)	**Rightsholder**	Royal Society of Chemistry
Date	12/31/1998	**Publication Type**	e-Journal
Language	English		

Appendix B. XPS Peak Fitting

XPS technique is based on the photoelectric effect, in which a photon of energy ($h\nu$) ejects a core electron with a binding energy B.E., the kinetic energy of the ejected photoelectron is given by

$$K.E. = h\nu - B.E. - \phi_s \quad (1)$$

where ϕ_s is the analyzer's work function. Part of the photoelectrons move through the solid to the surface and experience inelastic scattering resulting in the background observed in XPS spectrum. The background in this work is described mainly by:

(i) Shirely background:

This model assumes an S-shaped background per peak, where the background at the higher binding energy side of the photoelectron peak is higher than that at the lower binding energy side. Also, the form of Shirely background depends on the number of electrons (intensity) at a given binding energy.

(ii) Tougaard background:

This model takes into account the initial energy distribution function and inelastic electron scattering over a limited energy range. Because of its complexity, a universal loss function has been derived that enables fitting backgrounds of relatively narrow energy range. CasaXPS offers a list of different universal cross sections where the loss function has different forms. For instance, the loss function form of "E Tougaard" background is Gaussian.

Ideally, one would expect to observe the photoelectron peak to be sharp lines, however, the peaks observed are broad. The broadness observed in the photoelectron peaks can be described as a convolution of a Gaussian and Lorentzian function, and is due to a combination

of factors such as: (1) the lifetime of the core hole created as the photoelectron is ejected, which is assumed to be Lorentzian in nature. According to the uncertainty principle, the photoelectron peak width is inversely proportional to the core hole lifetime; (2) the energy resolution of the analyzer (which is controlled by the pass energy as well as entrance/exist slit), and the full width at half maximum (FWHM) of the source, are usually taken to be Gaussian in nature.

Beside the broadness, asymmetric peaks are observed for metal samples. This asymmetry is ascribed to the interaction between the electrons in the conduction band with the core hole, as a consequence low energy electron-hole pairs are excited resulting in a high B.E. tail on the metallic photoelectron peaks.

In the work presented, all nonmetallic elements have been fit using approximations to a Voigt lineshape, which is a convolution of Gaussian and Lorentzian function. The Gaussian/Lorentzian product form used in this work is

$$GL(x,m,E,F) = \frac{\exp[-4\ln 2\,(1-m)\frac{(x-E)^2}{F^2}]}{1+4m\frac{(x-E)^2}{F^2}} \quad (2)$$

where the Gaussian function is

$$G(x,E,F) = \exp[-4\ln\frac{(x-E)^2}{F^2}] \quad (3)$$

and the Lorentzian function is

$$L(x,E,F) = \frac{1}{1+\frac{(X-E)^2}{F^2}} \quad (4)$$

here E is the energy of the center of the peak (in kinetic energy), F is the full width at half maximum (FWHM), and m is a parameter that controls mixing. That is, m=0 corresponds to a pure Gaussian, while m=1 the product form corresponds to a pure Lorentzian. On the other

hand, the asymmetry in metallic peaks in this work are fit with Lorentzian Asymmetric lineshape $LA(\alpha, \beta, m)$ where

$$LA\ (\alpha, \beta) = \begin{cases} [L(x, E, F)]^{\alpha} & x \leq E \\ [L(x, E, F)]^{\beta} & x > E \end{cases} \quad (5)$$

the parameters α and β controls the spread of the Lorentzian tail on the left and right side of the peak maximum, respectively. CasaXPS includes the parameter m in the asymmetric Lorentzian lineshape to specify the width of Gaussian used to convolute the Lorentzian curve.

References

1. Balakrishna, S.; Lomnicki, S.; McAvey, K. M.; Cole, R. B.; Dellinger, B.; Cormier, S. A. Environmentally persistent free radicals amplify ultrafine particle mediated cellular oxidative stress and cytotoxicity. *Part. Fibre Toxicol.* **2009,** *6*.

2. dela Cruz, A. L.; Cook, R. L.; Dellinger, B.; Lomnicki, S. M.; Donnelly, K. C.; Kelley, M. A.; Cosgriff, D. Assessment of environmentally persistent free radicals in soils and sediments from three Superfund sites. *Environ Sci Process Impacts* **2014,** *16* (1), 44-52.

3. dela Cruz, A. L. N.; Gehling, W.; Lomnicki, S.; Cook, R.; Dellinger, B. Detection of Environmentally Persistent Free Radicals at a Superfund Wood Treating Site. *Environ. Sci. Technol.* **2011,** *45* (15), 6356-6365.

4. Ingram, D. J. E.; Tapley, J. G.; Jackson, R.; Bond, R. L.; Murnaghan, A. R. Paramagnetic Resonance in Carbonaceous Solids. *Nature* **1954,** *174* (4434), 797-798.

5. Valavanidis, A.; Iopoulos, N.; Gotsis, G.; Fiotakis, K. Persistent free radicals, heavy metals and PAHs generated in particulate soot emissions and residue ash from controlled combustion of common types of plastic. *J Hazard Mater* **2008,** *156* (1-3), 277-284.

6. Tian, L. W.; Koshland, C. P.; Yano, J. K.; Yachandra, V. K.; Yu, I. T. S.; Lee, S. C.; Lucas, D. Carbon-Centered Free Radicals in Particulate Matter Emissions from Wood and Coal Combustion. *Energ Fuel* **2009,** *23* (5-6), 2523-2526.

7. Jankovic, J.; Jones, W.; Castranova, V.; Dalal, N. Measurement of Short-Lived Reactive Species and Long-Lived Free Radicals in Air Samples from Structural Fires. *Applied Occupational and Environmental Hygiene* **1993,** *8* (7), 650-654.

8. Nwosu, U. G.; Khachatryan, L.; Youm, S. G.; Roy, A.; dela Cruz, A. L. N.; Nesterov, E. E.; Dellinger, B.; Cook, R. L. Model system study of environmentally persistent free radicals formation in a semiconducting polymer modified copper clay system at ambient temperature. *RSC Advances* **2016,** *6* (49), 43453-43462.

9. Dellinger, B.; Khachatryan, L.; Masko, S.; Lomnicki, S. Free Radicals in Tobacco Smoke. *Mini-Reviews in Organic Chemistry* **2011,** *8* (4), 427-433.

10. Maskos, Z.; Dellinger, B. Formation of the Secondary Radicals from the Aging of Tobacco Smoke. *Energ Fuel* **2008,** *22* (1), 382-388.

11. Maskos, Z.; Khachatryan, L.; Dellinger, B. Precursors of Radicals in Tobacco Smoke and the Role of Particulate Matter in Forming and Stabilizing Radicals. *Energ Fuel* **2005,** *19* (6), 2466-2473.

12. Patterson, M. C.; DiTusa, M. F.; McFerrin, C. A.; Kurtz, R. L.; Hall, R. W.; Poliakoff, E. D.; Sprunger, P. T. Formation of environmentally persistent free radicals (EPFRs) on ZnO at room temperature: Implications for the fundamental model of EPFR generation. *Chem Phys Lett* **2017,** *670*, 5-10.

13. Dellinger, B.; Lomnicki, S.; Khachatryan, L.; Maskos, Z.; Hall, R. W.; Adounkpe, J.; McFerrin, C.; Truong, H. Formation and Stabilization of Persistent Free Radicals. *Symp. (Int.) Combust., [Proc.]* **2007,** *31* (1), 521-528.

14. Saravia, J.; Lee, G. I.; Lomnicki, S.; Dellinger, B.; Cormier, S. A. Particulate matter containing environmentally persistent free radicals and adverse infant respiratory health effects: a review. *J Biochem Mol Toxicol* **2013,** *27* (1), 56-68.

15. Vejerano, E.; Lomnicki, S.; Dellinger, B. Lifetime of combustion-generated environmentally persistent free radicals on Zn(II)O and other transition metal oxides. *J Environ Monit* **2012,** *14* (10), 2803-6.

16. Patterson, M. C.; Keilbart, N. D.; Kiruri, L. W.; Thibodeaux, C. A.; Lomnicki, S.; Kurtz, R. L.; Poliakoff, E. D.; Dellinger, B.; Sprunger, P. T. EPFR formation from phenol adsorption on Al2O3 and TiO2: EPR and EELS studies. *Chem Phys* **2013,** *422*, 277-282.

17. Lomnicki, S.; Truong, H.; Vejerano, E.; Dellinger, B. Copper Oxide-Based Model of Persistent Free Radical Formation on Combustion-Derived Particulate Matter. *Environ. Sci. Technol.* **2008,** *42* (13), 4982-4988.

18. Vejerano, E.; Lomnicki, S.; Dellinger, B. Formation and Stabilization of Combustion-Generated Environmentally Persistent Free Radicals on an Fe(III)(2)O-3/Silica Surface. *Environ. Sci. Technol.* **2011,** *45* (2), 589-594.

19. Vejerano, E.; Lomnicki, S. M.; Dellinger, B. Formation and stabilization of combustion-generated, environmentally persistent radicals on Ni(II)O supported on a silica surface. *Environ. Sci. Technol.* **2012,** *46* (17), 9406-11.

20. Olie, K.; Vermeulen, P. L.; Hutzinger, O. Chlorodibenzo-p-dioxins and chlorodibenzofurans are trace components of fly ash and flue gas of some municipal incinerators in The Netherlands. *Chemosphere* **1977,** *6* (8), 455-459.

21. Fine, P. M.; Cass, G. R.; Simoneit, B. R. T. Chemical Characterization of Fine Particle Emissions from the Wood Stove Combustion of Prevalent United States Tree Species. *Environmental Engineering Science* **2004,** *21* (6), 705-721.

22. Hays, M. D.; Fine, P. M.; Geron, C. D.; Kleeman, M. J.; Gullett, B. K. Open burning of agricultural biomass: Physical and chemical properties of particle-phase emissions. *Atmospheric Environment* **2005,** *39* (36), 6747-6764.

23. Schweigert, N.; Acero, J. L.; von Gunten, U.; Canonica, S.; Zehnder, A. J. B.; Eggen, R. I. L. DNA degradation by the mixture of copper and catechol is caused by DNA-copper-hydroperoxo complexes, probably DNA-Cu(I)OOH. *Environmental and Molecular Mutagenesis* **2000,** *36* (1), 5-12.

24. Daisey, J. M.; Mahanama, K. R.; Hodgson, A. T. Toxic volatile organic compounds in simulated environmental tobacco smoke: emission factors for exposure assessment. *J Expo Anal Environ Epidemiol* **1998,** *8* (3), 313-334.

25. Riveles, K.; Roza, R.; Talbot, P. Phenols, Quinolines, Indoles, Benzene, and 2-Cyclopenten-1-ones are Oviductal Toxicants in Cigarette Smoke. *Toxicol Sci* **2005,** *86* (1), 141-151.

26. Schlotzhauer, W. S.; Walters, D. B.; Snook, M. E.; Higman, H. C. Characterization of catechols, resorcinols, and hydroquinones in an acidic fraction of cigarette smoke condensate. *Journal of Agricultural and Food Chemistry* **1978,** *26* (6), 1277-1281.

27. Ballschmiter, K.; Braunmiller, I.; Niemczyk, R.; Swerev, M. Reaction pathways for the formation of polychloro-dibenzodioxins (PCDD) and—dibenzofurans (PCDF) in combustion processes: II. Chlorobenzenes and chlorophenols as precursors in the formation of polychloro-dibenzodioxins and—dibenzofurans in flame chemistry. *Chemosphere* **1988,** *17* (5), 995-1005.

28. Okeson, C. D.; Riley, M. R.; Fernandez, A.; Wendt, J. O. L. Impact of the composition of combustion generated fine particles on epithelial cell toxicity: influences of metals on metabolism. *Chemosphere* **2003,** *51* (10), 1121-1128.

29. Allouis, C.; Beretta, F.; D'Alessio, A. Structure of inorganic and carbonaceous particles emitted from heavy oil combustion. *Chemosphere* **2003,** *51* (10), 1091-1096.

30. Nielsen, M. T.; Livbjerg, H.; Fogh, C. L.; Jensen, J. N.; Simonsen, P.; Lund, C.; Poulsen, K.; Sander, B. Formation and emission of fine particles from two coal-fired power plants. *Combustion Science and Technology* **2002,** *174* (2), 79-113.

31. Wasson, S. J.; Linak, W. P.; Gullett, B. K.; King, C. J.; Touati, A.; Huggins, F. E.; Chen, Y.; Shah, N.; Huffman, G. P. Emissions of Chromium, Copper, Arsenic, and PCDDs/Fs from Open Burning of CCA-Treated Wood. *Environ. Sci. Technol.* **2005,** *39* (22), 8865-8876.

32. Olie, K.; Addink, R.; Schoonenboom, M. Metals as Catalysts during the Formation and Decomposition of Chlorinated Dioxins and Furans in Incineration Processes. *Journal of the Air & Waste Management Association* **1998,** *48* (2), 101-105.

33. Stieglitz, L.; Zwick, G.; Beck, J.; Roth, W.; Vogg, H. On the de-novo synthesis of PCDD/PCDF on fly ash of municipal waste incinerators. *Chemosphere* **1989,** *18* (1), 1219-1226.

34. Tuppurainen, K. A.; Ruokojärvi, P. H.; Asikainen, A. H.; Aatamila, M.; Ruuskanen, J. Chlorophenols as Precursors of PCDD/Fs in Incineration Processes: Correlations, PLS Modeling, and Reaction Mechanisms. *Environ. Sci. Technol.* **2000,** *34* (23), 4958-4962.

35. Gullett, B. K.; Bruce, K. R.; Beach, L. O. The effect of metal catalysts on the formation of polychlorinated dibenzo-p-dioxin and polychlorinated dibenzofuran precursors. *Chemosphere* **1990,** *20* (10), 1945-1952.

36. Addink, R.; Altwicker, E. R. Formation of polychlorinated dibenzo-p-dioxins and dibenzofurans on secondary combustor/boiler ash from a rotary kiln burning hazardous waste. *J Hazard Mater* **2004,** *114* (1), 53-57.

37. Nganai, S.; Lomnicki, S.; Dellinger, B. Ferric Oxide Mediated Formation of PCDD/Fs from 2-Monochlorophenol. *Environ. Sci. Technol.* **2009,** *43* (2), 368-373.

38. Brown, L. M.; Collings, N.; Harrison, R. M.; Maynard, A. D.; Maynard, R. L.; Cass Glen, R.; Hughes Lara, A.; Bhave, P.; Kleeman Michael, J.; Allen Jonathan, O.; Salmon Lynn, G. The chemical composition of atmospheric ultrafine particles. *Philosophical Transactions of the Royal Society of London. Series A: Mathematical, Physical and Engineering Sciences* **2000,** *358* (1775), 2581-2592.

39. McFerrin, C. A.; Hall, R. W.; Dellinger, B. Ab initio study of the formation and degradation reactions of semiquinone and phenoxyl radicals. *J Mol Struc-Theochem* **2008,** *848* (1-3), 16-23.

40. Chen, Y.; Shah, N.; Huggins, F. E.; Huffman, G. P.; Dozier, A. Characterization of ultrafine coal fly ash particles by energy-filtered TEM. *Journal of Microscopy* **2005,** *217* (3), 225-234.

41. Huffman, G. P.; Huggins, F. E.; Shah, N.; Huggins, R.; Linak, W. P.; Miller, C. A.; Pugmire, R. J.; Meuzelaar, H. L. C.; Seehra, M. S.; Manivannan, A. Characterization of Fine Particulate Matter Produced by Combustion of Residual Fuel Oil. *Journal of the Air & Waste Management Association* **2000,** *50* (7), 1106-1114.

42. Chen, Y.; Shah, N.; Huggins, F. E.; Huffman, G. P. Investigation of the Microcharacteristics of PM2.5 in Residual Oil Fly Ash by Analytical Transmission Electron Microscopy. *Environ. Sci. Technol.* **2004,** *38* (24), 6553-6560.

43. Kleeman, M. J.; Schauer, J. J.; Cass, G. R. Size and Composition Distribution of Fine Particulate Matter Emitted from Motor Vehicles. *Environ. Sci. Technol.* **2000,** *34* (7), 1132-1142.

44. Linak, W. P.; Miller, C. A.; Wendt, J. O. L. Comparison of Particle Size Distributions and Elemental Partitioning from the Combustion of Pulverized Coal and Residual Fuel Oil. *Journal of the Air & Waste Management Association* **2000,** *50* (8), 1532-1544.

45. Kleeman, M. J.; Schauer, J. J.; Cass, G. R. Size and Composition Distribution of Fine Particulate Matter Emitted from Wood Burning, Meat Charbroiling, and Cigarettes. *Environ. Sci. Technol.* **1999,** *33* (20), 3516-3523.

46. Altwicker, E. R.; Konduri, R. K.; Lin, C.; Milligan, M. S. Rapid formation of polychlorinated dioxins/furans in the post combustion region during heterogeneous combustion. *Chemosphere* **1992,** *25* (12), 1935-1944.

47. Addink, R.; Bakker, W. C. M.; Olie, K. Influence of HCl and Cl_2 on the Formation of Polychlorinated Dibenzo-p-dioxins/Dibenzofurans in a Carbon/Fly Ash Mixture. *Environ. Sci. Technol.* **1995,** *29* (8), 2055-2058.

48. Cormier, S. A.; Lomnicki, S.; Fau - Backes, W.; Dellinger, B. Origin and health impacts of emissions of toxic by-products and fine particles from combustion and thermal treatment of hazardous wastes and materials. (0091-6765 (Print)).

49. Dellinger, B.; Pryor, W. A.; Cueto, B.; Squadrito, G. L.; Deutsch, W. A. The role of combustion-generated radicals in the toxicity of PM2.5. *P Combust Inst* **2000,** *28* (2), 2675-2681.

50. Lomnicki, S.; Dellinger, B. A detailed mechanism of the surface-mediated formation of PCDD/F from the oxidation of 2-chlorophenol on a CuO/silica surface. *J Phys Chem A* **2003,** *107* (22), 4387-4395.

51. Evans, J. S.; Tosteson, T.; Kinney, P. L. Cross-sectional mortality studies and air pollution risk assessment. *Environment International* **1984,** *10* (1), 55-83.

52. Lipfert, F. W. Air pollution and mortality: Specification searches using SMSA-based data. *Journal of Environmental Economics and Management* **1984,** *11* (3), 208-243.

53. Bobak, M.; Leon, D. A. Air pollution and infant mortality in the Czech Republic, 1986-88. *The Lancet* **1992,** *340* (8826), 1010-1014.

54. Özkaynak, H.; Thurston, G. D. Associations Between 1980 U.S. Mortality Rates and Alternative Measures of Airborne Particle Concentration. *Risk Analysis* **1987,** *7* (4), 449-461.

55. Mendelsohn, R.; Orcutt, G. An empirical analysis of air pollution dose-response curves. *Journal of Environmental Economics and Management* **1979,** *6* (2), 85-106.

56. Dellinger, B.; Pryor, W. A.; Cueto, R.; Squadrito, G. L.; Hegde, V.; Deutsch, W. A. Role of free radicals in the toxicity of airborne fine particulate matter. *Chemical research in toxicology* **2001,** *14* (10), 1371-7.

57. Balakrishna, S.; Lomnicki, S.; McAvey, K. M.; Cole, R. B.; Dellinger, B.; Cormier, S. A. Environmentally persistent free radicals amplify ultrafine particle mediated cellular oxidative stress and cytotoxicity. *Part Fibre Toxicol* **2009,** *6*, 11.

58. Vejerano, E. P.; Rao, G.; Khachatryan, L.; Cormier, S. A.; Lomnicki, S. Environmentally Persistent Free Radicals: Insights on a New Class of Pollutants. *Environ. Sci. Technol.* **2018,** *52* (5), 2468-2481.

59. Oberdörster, G. Pulmonary effects of inhaled ultrafine particles. *International Archives of Occupational and Environmental Health* **2000,** *74* (1), 1-8.

60. Calderón-Garcidueñas, L.; Mora-Tiscareño, A.; Fordham, L. A.; Chung, C. J.; García, R.; Osnaya, N.; Hernández, J.; Acuña, H.; Gambling, T. M.; Villarreal-Calderón, A.; Carson, J.; Koren, H. S.; Devlin, R. B. Canines as Sentinel Species for Assessing Chronic Exposures to Air Pollutants: Part 1. Respiratory Pathology. *Toxicol Sci* **2001,** *61* (2), 342-355.

61. Nemmar, A.; Hoet, P. H. M.; Vanquickenborne, B.; Dinsdale, D.; Thomeer, M.; Hoylaerts, M. F.; Vanbilloen, H.; Mortelmans, L.; Nemery, B. Passage of Inhaled Particles Into the Blood Circulation in Humans. *Circulation* **2002,** *105* (4), 411-414.

62. Li, N.; Sioutas, C.; Cho, A.; Schmitz, D.; Misra, C.; Sempf, J.; Wang, M.; Oberley, T.; Froines, J.; Nel, A. Ultrafine particulate pollutants induce oxidative stress and mitochondrial damage. *Environmental Health Perspectives* **2003,** *111* (4), 455-460.

63. Han, J.; Takeshita, K.; Utsumi, H. Noninvasive detection of hydroxyl radical generation in lung by diesel exhaust particles. *Free Radical Biology and Medicine* **2001,** *30* (5), 516-525.

64. Knaapen, A. M.; Shi, T.; Borm, P. J.; Schins, R. P. Soluble metals as well as the insoluble particle fraction are involved in cellular DNA damage induced by particulate matter. In *Oxygen/Nitrogen Radicals: Cell Injury and Disease*, Vallyathan, V.; Shi, X.; Castranova, V., Eds. Springer US: Boston, MA, 2002; pp 317-326.

65. Prahalad, A. K.; Soukup, J. M.; Inmon, J.; Willis, R.; Ghio, A. J.; Becker, S.; Gallagher, J. E. Ambient Air Particles: Effects on Cellular Oxidant Radical Generation in Relation to Particulate Elemental Chemistry. *Toxicology and Applied Pharmacology* **1999,** *158* (2), 81-91.

66. Prahalad, A. K.; Inmon, J.; Dailey, L. A.; Madden, M. C.; Ghio, A. J.; Gallagher, J. E. Air Pollution Particles Mediated Oxidative DNA Base Damage in a Cell Free System and in Human Airway Epithelial Cells in Relation to Particulate Metal Content and Bioreactivity. *Chemical research in toxicology* **2001,** *14* (7), 879-887.

67. Breen, A. P.; Murphy, J. A. Reactions of oxyl radicals with DNA. *Free Radical Biology and Medicine* **1995,** *18* (6), 1033-1077.

68. Cohen, G.; Yakushin, S.; Dembiec-Cohen, D. Proteinl-Dopa as an Index of Hydroxyl Radical Attack on Protein Tyrosine. *Analytical Biochemistry* **1998,** *263* (2), 232-239.

69. Gardner, H. Oxygen radical chemistry of polyunsaturated fatty acids. *Free Radical Biology and Medicine* **1989,** *7* (1), 65-86.

70. Girotti, A. Mechanisms of lipid peroxidation. *Journal of Free Radicals in Biology & Medicine* **1985,** *1* (2), 87-95.

71. Wang, P.; Thevenot, P.; Saravia, J.; Ahlert, T.; Cormier, S. A. Radical-Containing Particles Activate Dendritic Cells and Enhance Th17 Inflammation in a Mouse Model of Asthma. *American Journal of Respiratory Cell and Molecular Biology* **2011,** *45* (5), 977-983.

72. Lee, G. I.; Saravia, J.; You, D.; Shrestha, B.; Jaligama, S.; Hebert, V. Y.; Dugas, T. R.; Cormier, S. A. Exposure to combustion generated environmentally persistent free radicals enhances severity of influenza virus infection. *Part. Fibre Toxicol.* **2014,** *11* (1), 57.

73. Chuang, G. C.; Xia, H.; Mahne, S. E.; Varner, K. J. Environmentally Persistent Free Radicals Cause Apoptosis in HL-1 Cardiomyocytes. *Cardiovascular Toxicology* **2017,** *17* (2), 140-149.

74. Lord, K.; Moll, D.; Lindsey, J. K.; Mahne, S.; Raman, G.; Dugas, T.; Cormier, S.; Troxlair, D.; Lomnicki, S.; Dellinger, B.; Varner, K. Environmentally persistent free radicals decrease cardiac function before and after ischemia/reperfusion injury in vivo. *J Recept Signal Transduct Res* **2011,** *31* (2), 157-67.

75. Balakrishna, S.; Saravia, J.; Thevenot, P.; Ahlert, T.; Lominiki, S.; Dellinger, B.; Cormier, S. A. Environmentally persistent free radicals induce airway hyperresponsiveness in neonatal rat lungs. *Part Fibre Toxicol* **2011,** *8*, 11.

76. Karamanov, A.; Pelino, M.; Salvo, M.; Metekovits, I. Sintered glass-ceramics from incinerator fly ashes. Part II. The influence of the particle size and heat-treatment on the properties. *Journal of the European Ceramic Society* **2003,** *23* (10), 1609-1615.

77. Dellinger, B.; Pryor, W. A.; Cueto, R.; Squadrito, G.; Deutsch, W. A. The role of combustion-generated radicals in the toxicity of PM2.5. *P Combust Inst* **2000,** *28*, 2675-2681.

78. Oettinger, R.; Drumm, K.; Knorst, M.; Krinyak, P.; Smolarski, R.; Kienast, K. Production of Reactive Oxygen Intermediates by Human Macrophages Exposed to Soot Particles and Asbestos Fibers and Increase in NF-kappa B p50/p105 mRNA. *Lung* **1999,** *177* (6), 343-354.

79. Sagai, M.; Lim, H.; Ichinose, T. Lung Carcinogenesis by Diesel Exhaust Particles and the Carcinogenic Mechanism Via Active Oxygens. *Inhal Toxicol* **2000,** *12* (sup3), 215-223.

80. Samet, J. M.; Dominici, F.; Curriero, F. C.; Coursac, I.; Zeger, S. L. Fine Particulate Air Pollution and Mortality in 20 U.S. Cities, 1987–1994. *New England Journal of Medicine* **2000,** *343* (24), 1742-1749.

81. Stone, K.; Bermudez, E.; Zang, L. Y.; Carter, K. M.; Queenan, K. E.; Pryor, W. A. The ESR Properties, DNA Nicking, and DNA Association of Aged Solutions of Catechol Versus Aqueous Extracts of Tar from Cigarette Smoke. *Archives of Biochemistry and Biophysics* **1995,** *319* (1), 196-203.

82. Valavanidis, A.; Salika, A.; Theodoropoulou, A. Generation of hydroxyl radicals by urban suspended particulate air matter. The role of iron ions. *Atmospheric Environment* **2000,** *34* (15), 2379-2386.

83. Tokiwa, H.; Sera, N.; Nakanishi, Y.; Sagai, M. 8-Hydroxyguanosine formed in human lung tissues and the association with diesel exhaust particles. *Free Radical Biology and Medicine* **1999,** *27* (11), 1251-1258.

84. Tsurudome, Y.; Hirano, T.; Yamato, H.; Tanaka, I.; Sagai, M.; Hirano, H.; Nagata, N.; Itoh, H.; Kasai, H. Changes in levels of 8-hydroxyguanine in DNA, its repair and OGG1 mRNA in rat lungs after intratracheal administration of diesel exhaust particles. *Carcinogenesis* **1999,** *20* (8), 1573-1576.

85. Pryor, W. A.; Hales, B. J.; Premovic, P. I.; Church, D. F. The radicals in cigarette tar: their nature and suggested physiological implications. *Science* **1983,** *220* (4595), 425.

86. Hirakawa, K.; Oikawa, S.; Hiraku, Y.; Hirosawa, I.; Kawanishi, S. Catechol and Hydroquinone Have Different Redox Properties Responsible for Their Differential DNA-damaging Ability. *Chemical research in toxicology* **2002,** *15* (1), 76-82.

87. Pryor, W. A.; Stone, K.; Zang, L.; Bermúdez, E. Fractionation of Aqueous Cigarette Tar Extracts: Fractions That Contain the Tar Radical Cause DNA Damage. *Chemical research in toxicology* **1998,** *11* (5), 441-448.

88. Squadrito, G. L.; Cueto, R.; Dellinger, B.; Pryor, W. A. Quinoid redox cycling as a mechanism for sustained free radical generation by inhaled airborne particulate matter. *Free Radical Biology and Medicine* **2001,** *31* (9), 1132-1138.

89. Pryor, W. A. Oxy-Radicals and Related Species: Their Formation, Lifetimes, and Reactions. *Annual Review of Physiology* **1986,** *48* (1), 657-667.

90. Li, Y.; Trush, M. A. Reactive Oxygen-dependent DNA Damage Resulting from the Oxidation of Phenolic Compounds by a Copper-Redox Cycle Mechanism. *Cancer Research* **1994,** *54* (7 Supplement), 1895s.

91. Toledano, D. S.; Henrich, V. E. Kinetics of SO2 Adsorption on Photoexcited α-Fe2O3. *The Journal of Physical Chemistry B* **2001,** *105* (18), 3872-3877.

92. Parkinson, G. S. Iron oxide surfaces. *Surface Science Reports* **2016,** *71* (1), 272-365.

93. Kukier, U.; Ishak, C. F.; Sumner, M. E.; Miller, W. P. Composition and element solubility of magnetic and non-magnetic fly ash fractions. *Environmental Pollution* **2003,** *123* (2), 255-266.

94. Wilson, R. Appendix 1: Vacuum Technology for Applied Surface Science. *Surface Analysis – The Principal Techniques* **2009**, 613-647.

95. Ibach, H. *Physics of surfaces and interfaces*. Springer: 2006; Vol. 12.

96. Murphy, D. M. EPR (Electron Paramagnetic Resonance) Spectroscopy of Polycrystalline Oxide Systems. *Metal Oxide Catalysis* **2008**, 1-50.

97. Eaton, G. R.; Eaton, S. S.; Barr, D. P.; Weber, R. T. Basics of Continuous Wave EPR. In *Quantitative EPR: A Practitioners Guide*, Eaton, G. R.; Eaton, S. S.; Barr, D. P.; Weber, R. T., Eds. Springer Vienna: Vienna, 2010; pp 1-14.

98. Lucas, C. A. Surface Structure Determination by Interference Techniques. *Surface Analysis – The Principal Techniques* **2009**, 391-478.

99. Oura, K.; Lifshits, V.; Saranin, A.; Zotov, A.; Katayama, M. *Surface science: an introduction*. Springer Science & Business Media: 2013.

100. Ratner, B. D.; Castner, D. G. Electron Spectroscopy for Chemical Analysis. *Surface Analysis – The Principal Techniques* **2009**, 47-112.

101. Heide, P. Data Collection and Quantification. In *X-Ray Photoelectron Spectroscopy*, 2011; pp 61-99.

102. Heide, P. Spectral Interpretation. *X-Ray Photoelectron Spectroscopy* **2011**, 101-140.

103. DAR 400 & XM 1000: Sources for X-Ray Photoelectron Spectroscopy. GmbH, O. N., Ed. 2011.

104. Larkin, P. Chapter 2 - Basic Principles. In *Infrared and Raman Spectroscopy*, Larkin, P., Ed. Elsevier: Oxford, 2011; pp 7-25.

105. Jaggi, N.; Vij, D. R. FOURIER TRANSFORM INFRARED SPECTROSCOPY. In *Handbook of Applied Solid State Spectroscopy*, Vij, D. R., Ed. Springer US: Boston, MA, 2006; pp 411-450.

106. Lucas, C. A. Surface Structure Determination by Interference Techniques. In *Surface Analysis – The Principal Techniques*, 2009; pp 391-478.

107. Solar simulation technology: A guide to solar simulation and solar simulators. https://g2voptics.com/solar-simulation/ (accessed 09/28/2019).

108. Reference Solar Spectral Irradiance: Air Mass 1.5. https://rredc.nrel.gov/solar//spectra/am1.5/ (accessed 09/28/2019).

109. The global standard spectrum (AM1.5g). https://www2.pvlighthouse.com.au/resources/courses/altermatt/The%20Solar%20Spectrum/The%20global%20standard%20spectrum%20(AM1-5g).aspx (accessed 09/28/2019).

110. Standard solar spectra. https://www.pveducation.org/pvcdrom/appendices/standard-solar-spectra (accessed 09/28/2019).

111. Khachatryan, L.; Vejerano, E.; Lomnicki, S.; Dellinger, B. Environmentally Persistent Free Radicals (EPFRs). 1. Generation of Reactive Oxygen Species in Aqueous Solutions. *Environ. Sci. Technol.* **2011,** *45* (19), 8559-8566.

112. Mahne, S.; Chuang, G. C.; Pankey, E.; Kiruri, L.; Kadowitz, P. J.; Dellinger, B.; Varner, K. J. Environmentally persistent free radicals decrease cardiac function and increase pulmonary artery pressure. *Am. J. Physiol.: Heart Circ. Physiol.* **2012,** *303* (9), H1135-42.

113. Pan, B.; Li, H.; Lang, D.; Xing, B. Environmentally persistent free radicals: Occurrence, formation mechanisms and implications. *Environmental Pollution* **2019,** *248*, 320-331.

114. Lomnicki, S.; Truong, H.; Dellinger, B. Mechanisms of product formation from the pyrolytic thermal degradation of catechol. *Chemosphere* **2008,** *73* (4), 629-633.

115. Alderman, S. L.; Farquar, G. R.; Poliakoff, E. D.; Dellinger, B. An Infrared and X-ray Spectroscopic Study of the Reactions of 2-Chlorophenol, 1,2-Dichlorobenzene, and Chlorobenzene with Model CuO/Silica Fly Ash Surfaces. *Environ. Sci. Technol.* **2005,** *39* (19), 7396-7401.

116. Vejerano, E.; Rao, G.; Khachatryan, L.; Cormier, S. A.; Lomnicki, S. Environmentally Persistent Free Radicals: Insights on a New Class of Pollutants. **2018,** (1520-5851 (Electronic)).

117. Kiruri, L. W.; Khachatryan, L.; Dellinger, B.; Lomnicki, S. Effect of copper oxide concentration on the formation and persistency of environmentally persistent free radicals (EPFRs) in particulates. **2014,** (1520-5851 (Electronic)).

118. Yang, L.; Liu, G.; Zheng, M.; Jin, R.; Zhao, Y.; Wu, X.; Xu, Y. Pivotal Roles of Metal Oxides in the Formation of Environmentally Persistent Free Radicals. **2017,** (1520-5851 (Electronic)).

119. Ruan, X.; Sun, Y.; Du, W.; Tang, Y.; Liu, Q.; Zhang, Z.; Doherty, W.; Frost, R. L.; Qian, G.; Tsang, D. Formation, characteristics, and applications of environmentally persistent free radicals in biochars: A review. *Bioresource Technology* **2019,** *281*, 457-468.

120. Patterson, M. C.; Thibodeaux, C. A.; Kizilkaya, O.; Kurtz, R. L.; Poliakoff, E. D.; Sprunger, P. T. Electronic Signatures of a Model Pollutant-Particle System: Chemisorbed Phenol on TiO2(110). *Langmuir* **2015,** *31* (13), 3869-3875.

121. Thibodeaux, C. A.; Poliakoff, E. D.; Kizilkaya, O.; Patterson, M. C.; DiTusa, M. F.; Kurtz, R. L.; Sprunger, P. T. Probing environmentally significant surface radicals: Crystallographic and temperature dependent adsorption of phenol on ZnO. *Chem Phys Lett* **2015,** *638*, 56-60.

122. Seeger, P. A.; Daemen, L. L.; Larese, J. Z. Resolution of VISION, a Crystal-Analyzer Spectrometer. *Nucl. Instrum. Methods Phys. Res., Sect. A* **2009,** *604* (3), 719-728.

123. Biesinger, M. C.; Lau, L. W. M.; Gerson, A. R.; Smart, R. C. Resolving surface chemical states in XPS analysis of first row transition metals, oxides and hydroxides: Sc, Ti, V, Cu and Zn. *Appl. Surf. Sci.* **2010,** *257* (3), 887-898.

124. Biesinger, M. C.; Payne, B. P.; Grosvenor, A. P.; Lau, L. W. M.; Gerson, A. R.; Smart, R. S. C. Resolving surface chemical states in XPS analysis of first row transition metals, oxides and hydroxides: Cr, Mn, Fe, Co and Ni. *Appl. Surf. Sci.* **2011,** *257* (7), 2717-2730.

125. Jia, H.; Zhao, S.; Shi, Y.; Zhu, L.; Wang, C.; Sharma, V. K. Transformation of Polycyclic Aromatic Hydrocarbons and Formation of Environmentally Persistent Free Radicals on Modified Montmorillonite: The Role of Surface Metal Ions and Polycyclic Aromatic Hydrocarbon Molecular Properties. *Environ. Sci. Technol.* **2018,** *52* (10), 5725-5733.

126. Zhao, S.; Gao, P.; Miao, D.; Wu, L.; Qian, Y.; Chen, S.; Sharma, V. K.; Jia, H. Formation and Evolution of Solvent-Extracted and Nonextractable Environmentally Persistent Free Radicals in Fly Ash of Municipal Solid Waste Incinerators. *Environ. Sci. Technol.* **2019,** *53* (17), 10120-10130.

127. Zhao, S.; Miao, D.; Zhu, K.; Tao, K.; Wang, C.; Sharma, V. K.; Jia, H. Interaction of benzo[a]pyrene with Cu(II)-montmorillonite: Generation and toxicity of environmentally persistent free radicals and reactive oxygen species. **2019,** (1873-6750 (Electronic)).

128. Ding, X.; Wu, X.; Zhao, Y.; He, S. C–H Bond Activation by Oxygen-Centered Radicals over Atomic Clusters. *Accounts of Chemical Research* **2012,** *45* (3), 382-390.

129. Zhang, M.; Zhao, Y.; Liu, Q.; Li, X.; He, S. Does Each Atom Count in the Reactivity of Vanadia Nanoclusters? *Journal of the American Chemical Society* **2017,** *139* (1), 342-347.

130. Yang, L.; Liu, G.; Zheng, M.; Zhao, Y.; Jin, R.; Wu, X.; Xu, Y. Molecular Mechanism of Dioxin Formation from Chlorophenol based on Electron Paramagnetic Resonance Spectroscopy. **2017,** (1520-5851 (Electronic)).

131. Jia, H.; Zhao, J.; Li, L.; Li, X.; Wang, C. Transformation of polycyclic aromatic hydrocarbons (PAHs) on Fe(III)-modified clay minerals: Role of molecular chemistry and clay surface properties. *Applied Catalysis B: Environmental* **2014,** *154-155*, 238-245.

132. Jia, H.; Zhao, J.; Fan, X.; Dilimulati, K.; Wang, C. Photodegradation of phenanthrene on cation-modified clays under visible light. *Applied Catalysis B: Environmental* **2012,** *123-124*, 43-51.

133. Keresztury, G.; Billes, F.; Kubinyi, M.; Sundius, T. A Density Functional, Infrared Linear Dichroism, and Normal Coordinate Study of Phenol and its Deuterated Derivatives: Revised Interpretation of the Vibrational Spectra. *The Journal of Physical Chemistry A* **1998,** *102* (8), 1371-1380.

134. Oku, M.; Matsuta, H.; Wagatsuma, K.; Waseda, Y.; Kohiki, S. Removal of inelastic scattering part from Ti2p XPS spectrum of TiO2 by deconvolution method using O1s as response function. *J. Electron Spectrosc. Relat. Phenom.* **1999,** *105* (2), 211-218.

135. Krzywiecki, M.; Grządziel, L.; Sarfraz, A.; Iqbal, D.; Szwajca, A.; Erbe, A. Zinc oxide as a defect-dominated material in thin films for photovoltaic applications – experimental determination of defect levels, quantification of composition, and construction of band diagram. *Phys. Chem. Chem. Phys.* **2015,** *17* (15), 10004-10013.

136. D'Arienzo, M.; Mostoni, S.; Crapanzano, R.; Cepek, C.; Di Credico, B.; Fasoli, M.; Polizzi, S.; Vedda, A.; Villa, I.; Scotti, R. Insight into the Influence of ZnO Defectivity on the Catalytic Generation of Environmentally Persistent Free Radicals in ZnO/SiO2 Systems. *The Journal of Physical Chemistry C* **2019,** *123* (35), 21651-21661.

137. Feld-Cook, E. E.; Bovenkamp-Langlois, L.; Lomnicki, S. M. Effect of Particulate Matter Mineral Composition on Environmentally Persistent Free Radical (EPFR) Formation. *Environ. Sci. Technol.* **2017,** *51* (18), 10396-10402.

138. Fahmy, B., Ding, L., You, D., Lomnicki, S., Dellinger, B., & Cormier, S. A. In vitro and in vivo assessment of pulmonary risk associated with exposure to combustion generated fine particles. *Environmental Toxicology and Pharmacology* **2010,** *29* (2), 173-182.

139. Laden, F., Neas, L. M., Dockery, D. W., Schwartz, J. Association of fine particulate matter from different sources with daily mortality in six U.S. cities. **2000,** *108* (10), 941-947.

140. Guan, X.; Ghimire, A.; Potter, P. M.; Lomnicki, S. Role of Fe2O3 in fly ash surrogate on PCDD/Fs formation from 2-monochlorophenol. *Chemosphere* **2019,** *226*, 809-816.

141. Jia, H.; Nulaji, G.; Gao, H.; Wang, F.; Zhu, Y.; Wang, C. Formation and Stabilization of Environmentally Persistent Free Radicals Induced by the Interaction of Anthracene with Fe(III)-Modified Clays. *Environ. Sci. Technol.* **2016,** *50* (12), 6310-9.

142. Jia, H.; Zhao, S.; Shi, Y.; Zhu, K.; Gao, P.; Zhu, L. Mechanisms for light-driven evolution of environmentally persistent free radicals and photolytic degradation of PAHs on Fe(III)-montmorillonite surface. **2019,** (1873-3336 (Electronic)).

143. Nwosu, U. G.; Roy, A.; dela Cruz, A. L.; Dellinger, B.; Cook, R. Formation of environmentally persistent free radical (EPFR) in iron(III) cation-exchanged smectite clay. *Environ Sci-Proc Imp* **2016,** *18* (1), 42-50.

144. Yamamoto, S.; Kendelewicz, T.; Newberg, J. T.; Ketteler, G.; Starr, D. E.; Mysak, E. R.; Andersson, K. J.; Ogasawara, H.; Bluhm, H.; Salmeron, M.; Brown, G. E.; Nilsson, A. Water Adsorption on α-Fe2O3(0001) at near Ambient Conditions. *The Journal of Physical Chemistry C* **2010,** *114* (5), 2256-2266.

145. Zhang, Z.; Yates, J. T. Band Bending in Semiconductors: Chemical and Physical Consequences at Surfaces and Interfaces. *Chemical Reviews* **2012,** *112* (10), 5520-5551.

146. Xue, M.; Guo, Q. Study on growth mechanisms and electronic structures of polar NiO(111) ultrathin films using iron oxide buffer layers. *Journal of Alloys and Compounds* **2014,** *598*, 224-229.

147. Carbone, M.; Piancastelli, M. N.; Casaletto, M. P.; Zanoni, R.; Besnard-Ramage, M. J.; Comtet, G.; Dujardin, G.; Hellner, L. Phenol adsorption on Si(111)7×7 studied by synchrotron radiation photoemission and photodesorption. *Surface Science* **1999,** *419* (2), 114-119.

148. Toledano, D. S.; Dufresne, E. R.; Henrich, V. E. Photoexcited Fe_2O_3 surfaces: Properties and chemisorption. *Journal of Vacuum Science & Technology A* **1998,** *16* (3), 1050-1054.

149. Solomon, J. L.; Madix, R. J.; Stöhr, J. Orientation and absolute coverage of benzene, aniline, and phenol on Ag(110) determined by NEXAFS and XPS. *Surface Science* **1991,** *255* (1), 12-30.

150. Lad, R. J.; Henrich, V. E. Structure of α-Fe_2O_3 single crystal surfaces following Ar+ ion bombardment and annealing in O2. *Surface Science* **1988,** *193* (1), 81-93.

151. Kurtz, R. L.; Henrich, V. E. Geometric structure of the α-Fe_2O_3(001) surface: A LEED and XPS study. *Surface Science* **1983,** *129* (2), 345-354.

152. Condon, N. G.; Murray, P. W.; Leibsle, F. M.; Thornton, G.; Lennie, A. R.; Vaughan, D. J. Fe_3O_4(111) termination of α-Fe_2O_3(0001). *Surface Science* **1994,** *310* (1), L609-L613.

153. Condon, N. G.; Leibsle, F. M.; Lennie, A. R.; Murray, P. W.; Parker, T. M.; Vaughan, D. J.; Thornton, G. Scanning tunnelling microscopy studies of α-Fe2O3(0001). *Surface Science* **1998,** *397* (1), 278-287.

154. Genuzio, F.; Sala, A.; Schmidt, T.; Menzel, D.; Freund, H. Interconversion of α-Fe2O3 and Fe3O4 Thin Films: Mechanisms, Morphology, and Evidence for Unexpected Substrate Participation. *The Journal of Physical Chemistry C* **2014,** *118* (50), 29068-29076.

155. Tang, Y.; Qin, H.; Wu, K.; Guo, Q.; Guo, J. The reduction and oxidation of Fe2O3(0001) surface investigated by scanning tunneling microscopy. *Surface Science* **2013,** *609*, 67-72.

156. Condon, N. G.; Leibsle, F. M.; Lennie, A. R.; Murray, P. W.; Vaughan, D. J.; Thornton, G. Biphase Ordering of Iron Oxide Surfaces. *Physical Review Letters* **1995,** *75* (10), 1961-1964.

157. Joseph, Y.; Wühn, M.; Niklewski, A.; Ranke, W.; Weiss, W.; Wöll, C.; Schlögl, R. Interaction of ethylbenzene and styrene with iron oxide model catalyst films at low coverages: A NEXAFS study. *Phys. Chem. Chem. Phys.* **2000,** *2* (22), 5314-5319.

158. Kraushofer, F.; Jakub, Z.; Bichler, M.; Hulva, J.; Drmota, P.; Weinold, M.; Schmid, M.; Setvin, M.; Diebold, U.; Blaha, P.; Parkinson, G. S. Atomic-Scale Structure of the Hematite α-Fe2O3(1$\bar{1}$02) "R-Cut" Surface. *The Journal of Physical Chemistry C* **2018,** *122* (3), 1657-1669.

159. Khachatryan, L.; Dellinger, B, Environmentally Persistent Free Radicals (EPFRs)-2. Are Free Hydroxyl Radicals Generated in Aqueous Solutions? *Environ. Sci. Technol.* **2011,** *45* (21), 9232-9239.

160. Calderón-Garcidueñas, L.; Gambling, T. M.; Acuña, H.; García, R.; Osnaya, N.; Monroy, S.; Villarreal-Calderón, A.; Carson, J.; Koren, H. S.; Devlin, R. B. Canines as Sentinel Species for Assessing Chronic Exposures to Air Pollutants: Part 2. Cardiac Pathology. *Toxicol Sci* **2001,** *61* (2), 356-367.

161. Linsebigler, A. L.; Lu, G.; Yates, J. T. Photocatalysis on TiO2 Surfaces: Principles, Mechanisms, and Selected Results. *Chemical Reviews* **1995,** *95* (3), 735-758.

162. Laoufi, N. A.; Tassalit, D.; Bentahar, F.; Génie, F. D. In The degradation of phenol in water solution by TiO_2 photocatalysis in a helical reactor., 2008.

163. Mino, L.; Zecchina, A.; Martra, G.; Rossi, A. M.; Spoto, G. A surface science approach to TiO2 P25 photocatalysis: An in situ FTIR study of phenol photodegradation at controlled water coverages from sub-monolayer to multilayer. *Applied Catalysis B: Environmental* **2016,** *196*, 135-141.

164. Di Valentin, C.; Neyman Km Fau - Risse, T.; Risse T Fau - Sterrer, M.; Sterrer M Fau - Fischbach, E.; Fischbach E Fau - Freund, H.-J.; Freund Hj Fau - Nasluzov, V. A.; Nasluzov Va Fau - Pacchioni, G.; Pacchioni G Fau - Rosch, N.; Rosch, N. Density-functional model cluster studies of EPR g tensors of Fs+ centers on the surface of MgO. (0021-9606 (Print)).

165. Gehling, W.; Dellinger, B. Environmentally Persistent Free Radicals and Their Lifetimes in PM2.5. *Environ. Sci. Technol.* **2013,** *47* (15), 8172-8178.

166. Gulley-Stahl, H.; Hogan, P. A.; Schmidt, W. L.; Wall, S. J.; Buhrlage, A.; Bullen, H. A. Surface Complexation of Catechol to Metal Oxides: An ATR-FTIR, Adsorption, and Dissolution Study. *Environ. Sci. Technol.* **2010,** *44* (11), 4116-4121.

167. Bremner, D. H.; Burgess, A. E.; Houllemare, D.; Namkung, K. Phenol degradation using hydroxyl radicals generated from zero-valent iron and hydrogen peroxide. *Applied Catalysis B: Environmental* **2006,** *63* (1), 15-19.

168. Sobczyński, A.; Duczmal, Ł.; Zmudziński, W. Phenol destruction by photocatalysis on TiO2: an attempt to solve the reaction mechanism. *Journal of Molecular Catalysis A: Chemical* **2004,** *213* (2), 225-230.

Vita

Nadra Sakr was born in Egypt. She received her Bachelor of Science degree in Physics from Ain Shams University. She entered Louisiana State University in 2012 to pursue her PhD in Physics.